Classical vibrational modes in phononic lattices: theory and experiment

Mihail Sigalas[I], Manvir S. Kushwaha[II], Eleftherios N. Economou[III], Maria Kafesaki[III], Ioannis E. Psarobas*,[IV] and Walter Steurer[V]

[I] Communication and Optics Lab, Agilent Labs, Agilent Technologies, 3500 Deer Creek Road, MS26M9, Palo Alto, California 94304, USA
[II] Institute of Physics, University of Puebla, P.O. Box J-45, Puebla 72570, Mexico
[III] FORTH, Institute of Electronic Structure and Laser, P.O. Box 1527, 71110 Heraklion, Crete, Greece
[IV] Section of Solid State Physics, The University of Athens, Panepistimioupolis, 15784 Athens, Greece
[V] Laboratory of Crystallography, Department of Materials, ETH Zurich and MNF, University of Zurich, 8093 Zurich, Switzerland

Received May 31, 2005; accepted June 9, 2005

Phononic crystal / Sonic bandgap materials / Classical spectral gap materials / Vibrations-lattice dynamics / Elastic waves

Abstract. We present a review, through selected illustrative examples, of the physics of classical vibrational modes in phononic lattices, which elaborates on the theory, the formalism, the methods, and mainly on the numerical and experimental results related to phononic crystals. Most of the topics addressed here, are written in a self-consistent way and they can be read as independent individual parts.

Part I: Theory-formalism

1. Introduction

In recent years, propagation of classical waves [electromagnetic (EM) or elastic waves] in composite materials with dielectric or, respectively, elastic properties which are periodic functions of the position, with a period comparable to the wavelength of the corresponding field, has been the object of considerable attention [1]–[4]. These materials, photonic and phononic crystals, respectively, whether they exist naturally or are artificially fabricated, exhibit a rich variety of physical properties of interest to fundamental and applied research. There are striking analogies between the propagation of electrons in ordinary crystals and EM/elastic waves in photonic/phononic crystals (see Table 1), so that a great variety of multiple-scattering (MS) methods as well as other traditional methods originally developed for electronic-structure calculations have been transferred to the field of photonic and phononic crystals. The reader may consult the work of Modinos *et al.* [5], where a theory of electron, EM, and elastic wave propagation in systems consisting of nonoverlapping scatterers in a host medium is presented. The theory provides a framework for a unified description of wave propagation in three-dimensional periodic structures, finite slabs of layered structures, and systems with impurities: isolated impurities, impurity aggregates, or randomly distributed impurities.

Phononic crystals, like photonic crystals, attracted a lot of interest among researchers mainly because of the possibility of frequency regions, known as absolute phononic gaps, over which there can be no propagation of elastic waves in the crystal, whatever the direction of propagation. At the beginning of this review we shall describe briefly the methods presently available for the calculation of the frequency band-structure of phononic crystals. The plane-wave method (PW) [6, 7] seems the most forward and, in conjuction with a supercell approach, can also treat defects [8] and finite slabs [9]. However, it has convergence problems, especially in the case of fluid-solid composites [12]. A MS method emanating from the traditional Korringa-Kohn-Rostoker (KKR) method [10, 11] developed for the calculation of the electronic structure of solids appears to be numerically more efficient [12–14]. The above methods apply to infinite phononic crystals made of non-dispersive lossless materials. In reality, however, one usually measures the transmittance or reflectance of finite slabs, which may be dispersive or dissipative. The well-known finite-difference-time domain (FDTD) method [15–17] gives the transmission, reflection, and absorption coefficients of elastic waves incident on a finite slab of a phononic crystal, but it gets computationally cumbersome for 3D systems [18]. Psarobas *et al.* [19] proposed an on-shell layer-MS method for the calculation of the complex band structure of 3D phononic crystals and of the transmittance/reflectance of slabs of the same. The method is similar to the layer-KKR (LKKR) method of low-energy electron diffraction (LEED) [20] and electron emission [21]. Liu *et al.* [13] proposed independently a method along the same lines for the transmittance/reflectance of a slab. Also a variational method was developed by Sánchez-Dehesa *et al.* [22–24]. Finally, over the years, certain combinations of the above methods appeared (see

* Correspondence author (e-mail: ipsarob@cc.uoa.gr)

Table 1. Band-structure-related properties of three periodic systems. (After Kushwaha *et al.* [1]).

Property	"**Electronic**" crystal	"**Photonic**" crystal	"**Phononic**" crystal
Materials	Crystalline solid (natural or grown)	Constructed of at least 2 dielectric materials	Constructed of at least 2 elastic materials
Parameters	Atomic numbers	$\varepsilon(\mathbf{r})$, $\mu(\mathbf{r})$ (E/M permitivities & permeabilities)	$\varrho(\mathbf{r})$, $c_l(\mathbf{r}), c_t(\mathbf{r})$ (Mass densities, sound speeds)
Lattice constant	1–5 Å (microscopic)	0.1 μm–1 cm (macroscopic)	$\gtrsim$1 μm (macroscopic)
Waves	De Broglie (electrons) ψ	EM (photons) (**E**, **H**)	Vibrational or sound (phonons) **u**
Polarization	Spin $\uparrow, \downarrow$	Transverse $\nabla \cdot \mathbf{D} = 0 (\nabla \cdot \mathbf{E} \neq 0)$	Coupled shear-compressional $(\nabla \cdot \mathbf{u} \neq 0, \nabla \times \mathbf{u} \neq \mathbf{0})$
Diff. equation	$\left[-(\hbar^2/2m)\,\nabla^2 + V(\mathbf{r})\right]\psi = i\hbar\,\partial_t\psi$	$\nabla \times \varepsilon\nabla \times \mathbf{E} = (\varepsilon/c^2)\,\partial_t^2\mathbf{E}$	see Table footnote[a]
Free particle limit	$W = \hbar^2k^2/2m$ (parabolic)	$\omega = ck/\sqrt{\varepsilon}$ (linear)	$\omega = c_{l,t}\,k$ (linear)
Spectral region	Radio waves, microwaves, optical, x-rays	Microwaves, optical	$\omega \lesssim 1$ GHz

a: $-\varrho c_t^2\nabla \times \nabla \times \mathbf{u} + \nabla\left[\nabla \cdot (\varrho c_l^2\mathbf{u})\right] - (2\nabla \cdot \mathbf{u} + \mathbf{u} \cdot \nabla)\,\nabla(\varrho c_t^2) + \left[\nabla(\varrho c_t^2) \cdot \nabla\right]\mathbf{u} = \varrho\,\partial_t^2\mathbf{u}$.

e.g. Ref. [25]), and well established numerical methods, such as the finite element method and the transfer matrix method have been used to address specific problems (e.g., a more complex geometry).

In this review, we present briefly the principles of the MS and the FDTD methods. The rest of the main methods appear in Part II through certain illustrative examples. More detailed presentations can be found in other contributions to this special issue. In addition, Part II also includes an extended collection of numerical results on phononic crystals, where the underlying physics is discussed. Finally, Part III is solely devoted to various experimental observations and results on the field.

2. Multiple scattering method

2.1 Introduction

Although the PW method is a very powerful tool for the calculation of the dispersion relations of acoustic and elastic waves, it fails in some important cases: It can not calculate accurately the dispersion relation of mixed (fluid/solid) composites, it also fails in cases where the contrast in the material parameters between scatterers and host is very high (due to the fact that very large-step functions need an extremely large number of Fourier components in order to be reproduced accurately).

These difficulties are overcome within the MS method, an approach based on the well-known in the electronic band-structure community Korringa-Kohn-Rostoker (KKR) theory [10, 11, 26–28]. The success of this theory in both electronic and electromagnetic [29–31] band-structure calculations was a strong motivation for its application in the acoustic/elastic problem as well. Moreover, in addition to its capability to calculate dispersion for mixed composites [12] and for high contrast composites [32], the MS method is capable to calculate *transmission* through finite slabs of those composites, *both periodic and random*; thus it is a valuable tool in the acoustic/elastic problem.

In what follows we will describe in detail the method and its application to both band structure and transmission calculations, restricting ourselves to three-dimensional periodic or random systems consisting of solid or fluid scatterers in a *fluid host*, i.e. to the scalar version of the method. For the full vector version (including all possible combinations of hosts and scatterers, bulk and layer-KKR) see Refs. [19, 33] and [13, 34] as well.

2.2 Description of the method

2.2.1 Main equations

One begins with the observation that in a system of many scatterers, either periodic or random, the incident wave at each scatterer is the sum of the scattered waves by all the other scatterers (plus the external field, if present). This idea is used for the determination of the total field and, through it, for the calculation of either the transmission coefficient or the dispersion relation.

The application of the method starts by writing the total pressure field $p(\mathbf{r})$ in the fluid host of the system as [12]

$$p(\mathbf{r}) = p^0(\mathbf{r}) + \sum_n p_n^{sc}(\mathbf{r})\,, \tag{1}$$

where $p^0(\mathbf{r})$ is the external field and $p_n^{sc}(\mathbf{r})$ the scattered field by the scatterer at the position $\mathbf{R}_n$. This scattered field, $p_n^{sc}(\mathbf{r})$, can be written as a sum of elementary spherical waves,

$$\begin{aligned} p_n^{sc}(\mathbf{r}) &= p^{sc}(\mathbf{r} - \mathbf{R}_n) \\ &= \sum_{lm} b_{lm}^n h_l(k_o|\mathbf{r} - \mathbf{R}_n|)\,Y_{lm}(\mathbf{r} - \mathbf{R}_n)\,. \end{aligned} \tag{2}$$

($h_l = j_l + in_l$ is the spherical Hankel function of the first kind and order l [35], and $k_o = \omega/c_o$, with c_o the wave velocity in the host material; Y_{lm} are the spherical harmonics [36, 37]). Thus, the determination of the total field of Eq. (1) is reduced to the calculation of the coefficients b_{lm}^n. The determination of b_{lm}^n is done by writing the incident field at the scatterer at the position $\mathbf{R}_n$ as

$$p_n^{\mathrm{inc}}(\mathbf{r}) = p^0(\mathbf{r}) + \sum_{p \neq n} p_p^{sc}(\mathbf{r})\,. \tag{3}$$

Writing $p_n^{inc}(\mathbf{r})$ as a sum of elementary spherical waves,

$$\begin{aligned} p_n^{\mathrm{inc}}(\mathbf{r}) &= p^{\mathrm{inc}}(\mathbf{r} - \mathbf{R}_n) \\ &= \sum_{lm} a_{lm}^n j_l(k_o|\mathbf{r} - \mathbf{R}_n|)\,Y_{lm}(\mathbf{r} - \mathbf{R}_n)\,, \end{aligned} \tag{4}$$

and substituting this expression and Eq. (2) in Eq. (3), one obtains

$$\sum_{lm} a^n_{lm} j_l(k_o|\mathbf{r}-\mathbf{R}_n|)\, Y_{lm}(\mathbf{r}-\mathbf{R}_n) = p^0(\mathbf{r}) + \sum_{p\neq n}\sum_{lm} b^p_{lm} h_l(k_o|\mathbf{r}-\mathbf{R}_p|)\, Y_{lm}(\mathbf{r}-\mathbf{R}_p)\,. \quad (5)$$

The coefficients b^n_{lm} are proportional to a^n_{lm},

$$b^n_{lm} = t^n_l a^n_{lm} \Rightarrow a^n_{lm} = [t^n_l]^{-1} b^n_{lm}\,, \quad (6)$$

where the proportionality coefficients t^n_l $(= 1/(-1+iw^n_l)$ with $w^n_l = \mathrm{Im}\,[(t^n_l)]^{-1} = \text{real})$ can be found by solving a single scattering problem [12, 38, 39]. Moreover, the spherical functions of (5) centered at $\mathbf{R}_p$ can be transformed to functions centered at $\mathbf{R}_n$,

$$h_l(k_o|\mathbf{r}-\mathbf{R}_p|)Y_{lm}(\mathbf{r}-\mathbf{R}_p) = \sum_{l'm'} j_{l'}(k_o|\mathbf{r}-\mathbf{R}_n|)\, Y_{l'm'}(\mathbf{r}-\mathbf{R}_n)\, g^{(h)}_{l'm'lm}(\mathbf{R}_p-\mathbf{R}_n) \quad \text{for} \quad |\mathbf{r}-\mathbf{R}_n| < |\mathbf{R}_p-\mathbf{R}_n|\,, \quad (7)$$

where

$$g^{(R)}_{l'm'lm}(\mathbf{D}) = \sum_{\lambda} [(-1)^{(l'-l-\lambda)/2}\, 4\pi C_{l'm';\,lm;\,\lambda m-m'} R_\lambda(kD) \times Y_{\lambda m-m'}(\mathbf{D})]\,, \quad R = j \text{ or } h \quad (8)$$

and $C_{l'm';\,lm;\,\lambda\mu}$ are the Gaunt numbers [12, 36]. Substituting (6) and (7) in (5), interchanging the (l', m') with the (l, m) in the r.h.s and writing the external field, p^0, also as a sum of spherical waves with center at $\mathbf{R}_n$,

$$p^0(\mathbf{r}) = \sum_{lm} a^{0n}_{lm} j_l(k_o|\mathbf{r}-\mathbf{R}_n|)\, Y_{lm}(\mathbf{r}-\mathbf{R}_n)\,, \quad (9)$$

we obtain (after few algebraic manipulations)

$$\sum_{l'm'}\sum_{p} [(t^p_{l'})^{-1}\, \delta_{ll'}\delta_{mm'}\delta_{pn} - g^{(h)}_{lml'm'}(\mathbf{R}_p-\mathbf{R}_n)\,(1-\delta_{pn})] \times b^p_{l'm'} = a^{0n}_{lm}\,. \quad (10)$$

Using Eq. (10), which constitutes a linear algebraic system, one can calculate the coefficients b^n_{lm}, and through them the total field and the *transmission coefficient*, in terms of the coefficients a^{0n}_{lm} of the incident wave.

For the calculation of the *dispersion relation* of an infinite periodic system, i.e. for the eigenmodes of the system in the absence of any external field, the coefficients a^{0n}_{lm} of Eq. (10) are set equal to zero, the coefficients b^p_{lm} of the different lattice sites are connected through Bloch's theorem, i.e. $b^p_{lm} = \mathrm{e}^{i\mathbf{k}\cdot(\mathbf{R}_p-\mathbf{R}_n)} b^n_{lm}$, and one seeks the frequencies for which the determinant of the homogeneous system

$$\sum_{l'm'}\Big[(t^p_{l'})^{-1}\,\delta_{ll'}\delta_{mm'} - \sum_p \mathrm{e}^{i\mathbf{k}\cdot(\mathbf{R}_p-\mathbf{R}_n)} \times g^{(h)}_{lml'm'}(\mathbf{R}_p-\mathbf{R}_n)\,(1-\delta_{pn})\Big]\, b^n_{l'm'} = 0 \quad (11)$$

vanishes. The calculation of this determinant requires the truncation of the summation over $l'm'$ and the calculation of the "infinite" sum $\sum_p \mathrm{e}^{i\mathbf{k}\cdot(\mathbf{R}_p-\mathbf{R}_n)} g^{(h)}_{lml'm'}(\mathbf{R}_p-\mathbf{R}_n)$. The way to perform this calculation, since the sum is not convergent, is through a technique known as Ewald's summation [12, 28, 40], which transforms the non-convergent to two equivalent convergent sums. The Ewald's summation procedure as it is applied in our case is described in detail in Ref. [12].

2.2.2 Generalized transmission coefficient

The transmission coefficient, T, for an acoustic wave transmitted through a periodic or random finite system is given by the transmitted energy flux (in the far field regime), normalized by the incident energy flux, $T = |\mathbf{J}|/|\mathbf{J}^0|$. The energy flux vector, $\mathbf{J}$, is given by

$$J_i = (\mathrm{Re}\,\sigma_{ij})\,(\mathrm{Re}\,\dot{u}_j) = \frac{\omega\,\mathrm{Im}\,(\sigma^*_{ij}u_j)}{2}\,, \quad (12)$$

where u_j are the components of the displacement vector, $\mathbf{u}$, and σ_{ij} are the stress tensor components [41]. The last part in the r.h.s. of Eq. (12) is obtained for a time dependence of the form $\mathbf{u}$, $\sigma \propto \mathrm{e}^{-i\omega t}$.

For *fluids* $\sigma_{ij} = -p\delta_{ij}$ and $\mathbf{u} = \nabla p/(\varrho\omega^2)$; thus, Eq. (12) becomes

$$\mathbf{J} = -\frac{1}{2\varrho\omega}\,\mathrm{Im}\,[p^*(\nabla p)]\,. \quad (13)$$

For an incident wave of the form

$$p^0(\mathbf{r}) = h_l(k_o r)\, Y_{lm}(\mathbf{r})\,, \quad (14)$$

and in the far field ($r \to \infty$), we have

$$p^0(\mathbf{r}) = (-i)^{l+1}\,\frac{1}{k_o}\,Y_{lm}(\mathbf{r})\,\frac{\mathrm{e}^{ik_o r}}{r} = f^0(\hat{\mathbf{r}})\,\frac{\mathrm{e}^{ik_o r}}{r} \quad \text{and} \quad J^0_r = -\frac{1}{2\varrho\omega}\,\frac{k_o}{r^2}\,|f^0(\hat{\mathbf{r}})|^2\,. \quad (15)$$

Under the presence of the sample (in the far field),

$$p(\mathbf{r}) = p^0(\mathbf{r}) + \sum_n p^{sc}_n(\mathbf{r}) = [f^0(\hat{\mathbf{r}}) + f^{sc}(\hat{\mathbf{r}})]\,\frac{\mathrm{e}^{ik_o r}}{r} \Rightarrow\; J_r = -\frac{1}{2\varrho\omega}\,\frac{k_o}{r^2}\,|f^0(\hat{\mathbf{r}}) + f^{sc}(\hat{\mathbf{r}})|^2\,. \quad (16)$$

Thus

$$qT = \left|1 + \frac{f^{sc}(\hat{\mathbf{r}})}{f^0(\hat{\mathbf{r}})}\right|^2\,. \quad (17)$$

The scattering amplitude f^{sc} can be calculated using $\sum_n p^{sc}_n(\mathbf{r}) = f^{sc}(\hat{\mathbf{r}})\,(\mathrm{e}^{ik_o r})/r$ and the expansions of the $p^{sc}_n(\mathbf{r})$ in the far field. Manipulating these expansions properly, one can find either the expression

$$f^{sc}(\hat{\mathbf{r}}) = \sum_n\sum_{lm}\sum_{l'm'} b^n_{lm} g^{(j)}_{l'm'lm}(\mathbf{R}_n)\,\frac{(-i)^{l'+1}}{k_o}\,Y_{l'm'}(\mathbf{r}) \quad (18)$$

or its alternative,

$$f^{sc}(\hat{\mathbf{r}}) = \sum_n\sum_{lm} b^n_{lm}\,\frac{(-i)^{l+1}}{k_o}\,Y_{lm}(\mathbf{r}-\mathbf{R}_n)\,\mathrm{e}^{ik_o|\mathbf{R}_n|\cos\theta_n}\,, \quad (19)$$

with θ_n the angle between $\mathbf{r}$ and $\mathbf{R}_n$.

3. Finite difference time domain method

3.1 Introduction

The FDTD method presented here is based on the discretization of the full elastic time dependent wave equation through a finite difference scheme. Both the time and the space derivatives are approximated by finite differences and the field at a given time point is calculated through the field at the previous points. Thus, one can obtain the field as a function of time at any point of a slab. The frequency dependence of the field is obtained through fast Fourier transform of the time results.

The FDTD method, while it was well known in the acoustics and seismology communities [42]–[45], had not been applied until only few years ago in the study of phononic crystals. Here the most important advantages of the method are that: a) it can give the field at any point inside and outside a sample, at every time; b) it can give the field in both frequency and time domains; c) its results can be directly compared with the experimental data, since the method calculates the transmission through finite samples; d) it can be applied in systems with arbitrary material combination (e.g. solids in fluids or fluids in solids); e) it can be applied in periodic systems as well as in systems with arbitrary configuration of the scatterers, giving thus the possibility to study defect states, waveguides, random systems etc. These important advantages of the method have been already exploited extensively in the field of electromagnetic wave band gap materials (photonic crystals) [46]–[51]. Here we will present the method as it is applied in elastic two-dimensional systems, i.e. systems of cylinders embedded in a host material, for transmission coefficient calculations.

3.2 Description of the method

The elastic wave equation in isotropic inhomogeneous media is [41],

$$\frac{\partial^2 u_i}{\partial t^2} = \frac{1}{\varrho}\,\frac{\partial \sigma_{ij}}{\partial x_j}\,, \tag{20}$$

where $\sigma_{ij} = \lambda(\mathbf{r})\,u_{ll}\delta_{ij} + 2\mu(\mathbf{r})\,u_{ij}$ and $u_{ij} = (\partial u_i/\partial x_j + \partial u_j/\partial x_i)/2$ (in Cartesian coordinates). In the above expressions u_i is the ith component of the displacement vector, $\mathbf{u}(\mathbf{r})$, σ_{ij} are the stress tensor components and u_{ij} the strain tensor components; $\lambda(\mathbf{r})$ and $\mu(\mathbf{r})$ are the so-called Lamé coefficients of the medium [41] and $\varrho(\mathbf{r})$ is the mass density. The λ, μ and ϱ are connected with the wave velocities in a medium through the relations $\mu = \varrho c_t^2$ and $\lambda = \varrho c_l^2 - 2\varrho c_t^2$, where c_l and c_t are, respectively, the velocity of the longitudinal and the transverse component of the wave. In a multicomponent system the λ, μ and ϱ are discontinuous functions of the position, $\mathbf{r}$.

As was mentioned above, here we consider systems consisting of infinitely long cylinders embedded in a homogeneous material. A cross section of such a system (periodic) is shown in Fig. 1. We consider the z axis to be parallel to the axis of the cylinders and propagation in the $x-y$ plane. As the system has translational symmetry along z-direction, the parameters $\lambda(\mathbf{r})$, $\mu(\mathbf{r})$ and $\varrho(\mathbf{r})$ do not depend on the coordinate z, and the wave equation for the z component is decoupled from the equations for the x and the y component. The equations for the x and the y component can be written as

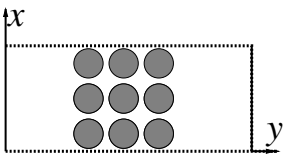

Fig. 1. The computational cell.

$$\begin{aligned}\frac{\partial^2 u_x}{\partial t^2} &= \frac{1}{\varrho}\left(\frac{\partial \sigma_{xx}}{\partial x} + \frac{\partial \sigma_{xy}}{\partial y}\right),\\ \frac{\partial^2 u_y}{\partial t^2} &= \frac{1}{\varrho}\left(\frac{\partial \sigma_{xy}}{\partial x} + \frac{\partial \sigma_{yy}}{\partial y}\right),\end{aligned} \tag{21}$$

where

$$\begin{aligned}\sigma_{xx} &= (\lambda + 2\mu)\,\frac{\partial u_x}{\partial x} + \lambda\,\frac{\partial u_y}{\partial y}\,,\\ \sigma_{yy} &= (\lambda + 2\mu)\,\frac{\partial u_y}{\partial y} + \lambda\,\frac{\partial u_x}{\partial x}\,,\\ \sigma_{xy} &= \mu\left(\frac{\partial u_x}{\partial y} + \frac{\partial u_y}{\partial x}\right).\end{aligned} \tag{22}$$

The above Eqs., (21) and (22), constitute the basis for the implementation of the FDTD in 2D systems. For this implementation the computational domain is divided into $i_{\max} \times j_{\max}$ subdomains (grids), with dimensions Δx, Δy, and the displacement vector components are discretized according to

$$u_\ell(i, j, k) = u_\ell(i\,\Delta x, j\,\Delta y, k\,\Delta t)\,, \quad \ell = x, y\,, \tag{23}$$

with $1 \le i \le i_{\max}$, $1 \le j \le j_{\max}$ and $k \ge 0$.

In the Eqs. (21) and (22), the derivatives are approximated in both space and time with finite differences [46]. For the space derivatives, central differences are used:

$$\begin{aligned}\left.\frac{\partial u_\ell}{\partial x}\right|_{i,j,k} &\approx D_0^x u_\ell(i, j, k)\\ &= [u_\ell(i + {}^1\!/_2, j, k) - u_\ell(i - {}^1\!/_2, j, k)]/\Delta x\,,\\ \left.\frac{\partial u_\ell}{\partial y}\right|_{i,j,k} &\approx D_0^y u_\ell(i, j, k)\\ &= [u_\ell(i, j + {}^1\!/_2, k) - u_\ell(i, j - {}^1\!/_2, k)]/\Delta y\,.\end{aligned} \tag{24}$$

For the time derivatives, a combination of forward and backward differences are used:

$$\left.\frac{\partial^2 u_\ell}{\partial t^2}\right|_{i,j,k} \approx D_+^t D_-^t u_\ell(i, j, k)\,, \tag{25}$$

where

$$\begin{aligned}D_+^t u_\ell(i, j, k) &= [u_\ell(i, j, k+1) - u_\ell(i, j, k)]/\Delta t\,,\\ D_-^t u_\ell(i, j, k) &= [u_\ell(i, j, k) - u_\ell(i, j, k-1)]/\Delta t\,,\end{aligned} \tag{26}$$

and $\ell = x, y$.

From the equation for u_x of (21), expanding around (i, j, k) and following the procedure described above, one

obtains

$$u_x(i, j, k+1) = 2u_x(i, j, k) - u_x(i, j, k-1) + \frac{\Delta_t^2}{\varrho(i, j)\,\Delta_x}\left[\sigma_{xx}(i+{}^1\!/_2, j, k) - \sigma_{xx}(i-{}^1\!/_2, j, k)\right] + \frac{\Delta_t^2}{\varrho(i, j)\,\Delta_y}\left[\sigma_{xy}(i, j+{}^1\!/_2, k) - \sigma_{xy}(i, j-{}^1\!/_2, k)\right]. \tag{27}$$

Similarly, from the equation for u_y of (21), expanding around $(i+{}^1\!/_2, j+{}^1\!/_2, k)$, one finds

$$\begin{aligned} u_y(i+{}^1\!/_2, j+{}^1\!/_2, k+1) &= 2u_y(i+{}^1\!/_2, j+{}^1\!/_2, k) - u_y(i+{}^1\!/_2, j+{}^1\!/_2, k-1) \\ &+ \left\{\frac{\Delta_t^2}{\varrho(i+{}^1\!/_2, j+{}^1\!/_2)\,\Delta_x} \times \left[\sigma_{xy}(i+1, j+{}^1\!/_2, k) - \sigma_{xy}(i, j+{}^1\!/_2, k)\right]\right\} \\ &+ \left\{\frac{\Delta_t^2}{\varrho(i+{}^1\!/_2, j+{}^1\!/_2)\,\Delta_y} \times \left[\sigma_{yy}(i+{}^1\!/_2, j+1, k) - \sigma_{yy}(i+{}^1\!/_2, j, k)\right]\right\}. \end{aligned} \tag{28}$$

The σ_{xx}, σ_{xy}, σ_{yy} at the time $k\,\Delta t$ are functions of the displacement vector components at the same time, $k\,\Delta t$, and are used for the updating of the fields for the next time. They are also discretized through Eq. (24) and their expressions after the discretization are given in 3.3.

The discretization presented in the previous equations insures second order accurate central differencing for the space derivatives. This has as a result, however, the field components u_x and u_y to be located at different space points, i, j for the u_x and $i+{}^1\!/_2$, $j+{}^1\!/_2$ for the u_y.

Using the procedure described above, the components u_x and u_y at the time step $k+1$ are calculated through their values at the step k. For insuring stability of the calculation the stability criterion used is [46]

$$\Delta t \leq 0.5/c\,\sqrt{1/\Delta x^2 + 1/\Delta y^2}\,, \tag{29}$$

where the velocity c is the highest among the sound velocities of the components of the composite.

To treat periodic systems, one can use Bloch's (periodic) boundary conditions $[u(\mathbf{r}+\mathbf{R}) = \exp(i\mathbf{k}\cdot\mathbf{R})\,u(\mathbf{r})$ ($\mathbf{R}$: lattice vector)] at the boundaries of the computational system along the propagation direction (at the $i=1$ and $i = i_{\max}$ of Fig. 1 − see dotted lines in Fig. 1), reducing thus considerably the computational memory and time.

For closing the computational space along the other boundaries, avoiding any back reflection from those boundaries, usually absorbing boundary conditions are used. Absorbing conditions are used also in all boundaries if non-periodic systems are treated. Among a variety of absorbing boundary conditions which have been discussed and utilized in the literature, the most common are the so-called Mur's [46, 52] and Liao's [46, 53] boundary conditions. Here we will present the absorbing conditions introduced by Zhou *et al.* [44, 45], which are first order absorbing conditions, giving almost no reflection from the boundaries, even after long computational times. Zhou's conditions are obtained by requiring the reflection at the boundaries to be zero for two angles of incidence (θ_1, θ_2); they can be written in the form

$$A\frac{\partial\bar{\mathbf{u}}}{\partial x} + B\frac{\partial\bar{\mathbf{u}}}{\partial y} + I\frac{\partial\bar{\mathbf{u}}}{\partial t} = 0\,, \tag{30}$$

where I is the identity 2×2 matrix, $\bar{\mathbf{u}}$ is the 2×1 matrix $[u_x, u_y]^T$ (T denotes the transpose of a matrix), and A, B are 2×2 matrices. For the boundary $j = j_{\max}$ the matrices A and B can be expressed as

$$A(\theta_1, \theta_2) = \frac{\eta_1}{\eta_1\xi_2 - \eta_2\xi_1}\,Q_2 - \frac{\eta_2}{\eta_1\xi_2 - \eta_2\xi_1}\,Q_1\,, \tag{31}$$

$$B(\theta_1, \theta_2) = \frac{\xi_2}{\eta_1\xi_2 - \eta_2\xi_1}\,Q_1 - \frac{\xi_1}{\eta_1\xi_2 - \eta_2\xi_1}\,Q_2\,, \tag{32}$$

with

$$Q_1 = \begin{bmatrix} c_{lo}\xi_1^2 + c_{to}\eta_1^2 & (c_{lo} - c_{to})\,\xi_1\eta_1 \\ (c_{lo} - c_{to})\,\xi_1\eta_1 & c_{lo}\eta_1^2 + c_{to}\xi_1^2 \end{bmatrix}, \tag{33}$$

$$Q_2 = \begin{bmatrix} c_{lo}\xi_2^2 + c_{to}\eta_2^2 & (c_{lo} - c_{to})\,\xi_2\eta_2 \\ (c_{lo} - c_{to})\,\xi_2\eta_2 & c_{lo}\eta_2^2 + c_{to}\xi_2^2 \end{bmatrix}, \tag{34}$$

and $\xi_i = \sin\theta_i$, $\eta_i = \cos\theta_i$ $(i = 1, 2)$. c_{lo} and c_{to} are, respectively, the longitudinal and the transverse wave velocity in the host material of the composite. For the boundary $j = j_{\min}$ the expressions of A and B are obtained from Eqs. (31) and (32) by replacing θ_i by $\theta_i + \pi$ $(i = 1, 2)$.

The condition (30) is discretized also using central differences in space and forward differences in time. For the implementation of (30) in phononic systems the requirement of complete absorption for $\theta_1 = 0$ and $\theta_2 = \pi/4$ gives in most of the cases exceptionally satisfactory results.

For calculating the transmission, the incident wave that is usually used is a pulse with a Gaussian envelop in space. The pulse is formed at $t = 0$ at the left side of the composite and propagates along the y-direction (see Fig. 1) A longitudinal pulse like that has the form

$$u_y = \alpha\,\sin(\omega t - y/c_{lo})\,\exp\left[-\beta(\omega t - y/c_{lo})^2\right], \tag{35}$$

while for a transverse one u_y is replaced by u_x and c_{lo} by c_{to}. The incident pulse is narrow enough in space as to permit the excitation of a wide range of frequencies.

The components of the displacement vector as a function of time are collected at various detection points depending on the structure of interest. They are converted into the frequency domain using fast Fourier transform. The transmission coefficient (T) is calculated either by normalizing the (frequency dependent) transmitted field intensity $(u_x^2 + u_y^2)$ by the incident field intensity or by normalizing the transmitted energy flux vector, $\mathbf{J}$ ($J_i = \sigma_{ij}\,\mathrm{d}u_j/\mathrm{d}t$ for real fields), by the incident one.

The pure acoustic waves case (waves in fluid composites) can also be treated with the FDTD using the Eqs. (21)–(22), but one has to omit the terms containing

the Lamé coefficient μ. The equations are discretized through the same procedure as for the full elastic case. The boundary conditions coefficients are calculated again through the Eqs. (31)–(34) where the velocity c_{to} must be replaced by c_{lo} (this replacement is essential in all the cases where the host material is fluid).

3.3 The calculation of the coefficients σ_{xx}, σ_{yy}, σ_{xy}

$$\sigma_{xx}(i+{}^1\!/_2, j, k) = (\lambda+2\mu)\,(i+{}^1\!/_2, j) \times [u_x(i+1, j, k) - u_x(i, j, k)]/\Delta_x + \lambda(i+{}^1\!/_2, j) \times \left[u_y(i+{}^1\!/_2, j+{}^1\!/_2, k) - u_y(i+{}^1\!/_2, j-{}^1\!/_2, k)\right]/\Delta_y\,, \tag{36}$$

$$\sigma_{xx}(i-{}^1\!/_2, j, k) = (\lambda+2\mu)\,(i-{}^1\!/_2, j)\,[u_x(i, j, k) - u_x(i-1, j, k)]/\Delta_x + \lambda(i-1/2, j) \times [u_y(i-{}^1\!/_2, j+{}^1\!/_2, k) - u_y(i-{}^1\!/_2, j-{}^1\!/_2, k)]/\Delta_y\,, \tag{37}$$

$$\sigma_{xy}(i, j+{}^1\!/_2, k) = \mu(i, j+{}^1\!/_2)\,[u_x(i, j+1, k) - u_x(i, j, k)]/\Delta_y + \mu(i, j+{}^1\!/_2) \times [u_z(i+{}^1\!/_2, j+{}^1\!/_2, k) - u_y(i-{}^1\!/_2, j+{}^1\!/_2, k)]/\Delta_x\,, \tag{38}$$

$$\sigma_{xy}(i, j-{}^1\!/_2, k) = \mu(i, j-{}^1\!/_2)\,[u_x(i, j, k) - u_x(i, j-1, k)]/\Delta_z + \mu(i, j-{}^1\!/_2) \times [u_y(i+{}^1\!/_2, j-{}^1\!/_2, k) - u_y(i-{}^1\!/_2, j-{}^1\!/_2, k)]/\Delta_x\,, \tag{39}$$

$$\sigma_{xy}(i+1, j+{}^1\!/_2, k) = \mu(i+1, j+{}^1\!/_2) \times [u_x(i+1, j+1, k) - u_x(i+1, j, k)]/\Delta_y + \mu(i+1, j+{}^1\!/_2) \times [u_y(i+{}^3\!/_2, j+{}^1\!/_2, k) - u_y(i+{}^1\!/_2, j+{}^1\!/_2, k)]/\Delta_x\,, \tag{40}$$

$$\sigma_{xy}(i, j+{}^1\!/_2, k) = \mu(i, j+{}^1\!/_2) \times [u_x(i, j+1, k) - u_x(i, j, k)]/\Delta_y + \mu(i, j+{}^1\!/_2) \times [u_y(i+{}^1\!/_2, j+{}^1\!/_2, k) - u_y(i-{}^1\!/_2, j+{}^1\!/_2, k)]/\Delta_x\,, \tag{41}$$

$$\sigma_{yy}(i+{}^1\!/_2, j+1, k) = (\lambda+2\mu)\,(i+{}^1\!/_2, j+1) \times [u_y(i+{}^1\!/_2, j+{}^3\!/_2, k) - u_y(i+{}^1\!/_2, j+{}^1\!/_2, k)]/\Delta_y + \lambda(i+{}^1\!/_2, j+1) \times [u_x(i+1, j+1, k) - u_x(i, j+1, k)]/\Delta_x\,, \tag{42}$$

$$\sigma_{yy}(i+{}^1\!/_2, j, k) = (\lambda+2\mu)\,(i+{}^1\!/_2, j) \times [u_y(i+{}^1\!/_2, j+{}^1\!/_2, k) - u_y(i+{}^1\!/_2, j-{}^1\!/_2, k)]/\Delta_y + \lambda(i+{}^1\!/_2, j)\,[u_x(i+1, j, k) - u_x(i, j, k)]/\Delta_x\,. \tag{43}$$

Part II: Theory-numerical results

4. General remarks

This section serves as an introduction to the vibrational band structures of periodic elastic composites which is the main theme of this review. Most of the composites now proposed for practical applications have only two constituents, and we will focus our attention on this class of composite materials; albeit improved fabrication technology is expected to lead to the synthesis of more sophisticated composite materials in the future. An important motivation for a systematic investigation of the vibrational band structure of phononic crystals came from the analogous theoretical and experimental findings in photonic crystals. EM waves in photonic crystals and elastic waves in phononic crystals represent classical analogues of the quantum mechanical waves of electrons in crystals. Some contrasting properties of electronic, photonic, and phononic crystals are listed in Table 1. Of special interest are phononic crystals, tailored from two materials which differ in their elastic properties, with a *complete absolute* frequency-gap; this is a frequency region wherein phonons (vibrations) are prohibited, irrespective of the polarization of the phonon and of the direction of its propagation in space.

From a fundamental point of view, cleverly synthesized periodic elastic composites exhibiting a *complete* band-gap may offer a systematic route to realize the Anderson localization of sound and vibrations, just as the Anderson localization of light. The term localization has recently appeared in the literature on wave propagation in random media, but less commonly than in the theory of disordered condensed systems. Shortly after the seminal paper of Anderson on electron localization in disordered systems [54], the problem of phonon localization in random systems was considered [55]. However, a closely related subject of localization of elastic (and acoustic) waves in macroscopic systems, where the role of the disordered material is played by a medium with a sharply varying elastic (and acoustic) properties which can strongly scatter the respective vibrations, has drawn attention only more recently [56]–[61]. The concept of classical localization focused initially on elastic waves in disordered solids. John *et al.* [62–64] studied the localization of phonons in a $2+\varepsilon$ dimensions using a first-principles theory based on the field theoretical formulation of electron localization by Wegner [65]. It was demonstrated that all finite-frequency phonons in one and two dimensions are localized with low-frequency localization length diverging as ω^{-2} and e^{1/ω^2}, respectively, and that a mobility edge, ω_*, separating low-frequency extended states from high-frequency localized states exist for $n > 2$; n refers to the number of dimensions. This field theory (or nonlinear σ-model) was later recovered and extended by diagrammatic perturbation techniques [66]. Other important theoretical [67]–[76] and experimental [77]–[86] developments related with the classical wave localization were exhaustively discussed in [3].

From practical point of view, periodic elastic composites comprised of two (or, more) different materials are becoming of increasing importance in modern technology. Such composites allow the tailoring of some special prop-

erties, unavailable in their homogeneous constituents. A periodic elastic composite can be synthesized such as to exhibit a *complete* elastic band-gap. Thus a vibrator or a small (real) crystal introduced into an otherwise periodic composite as a defect would be unable to generate sound or vibrations within the band-gap. This implies that such periodic elastic composites could be engineered to provide a vibrationless environment for high precision mechanical devices in a given frequency range. Ferroelectric, piezoelectric, pyroelectric, and piezomagnetic periodic composites have had long-standing applications as medical ultrasonic and naval transducers, as well as for related tasks in medical imaging [87]–[96]. Such composites were initially constructed and used for sonar applications, and are now being widely used for ultrasonic transducers. Combining, for example, a piezoelectric ceramic and passive polymer to form a periodic composite allows the transducer engineer to design new piezoelectrics which offer substantial advantages over the conventional piezoelectric ceramics and polymers. The novelty of the resultant structure lies not in the constituents but in the way they are assembled to produce materials with properties suitable to each specific application. The effective properties of the composites are usually expressed in terms of averages over the properties of the constituents. However, examining these composites on a scale in which the substructure of the constituent ceramic and polymer are evident leads one to understand the principles used to design the composite. Often these substructures are just miniature versions of transducers familiar to the design engineer on a much larger scale.

The extensive research on elastic and/or acoustic periodic composites actually started when Sigalas *et al.* [97] reported a narrow but *complete* band-gap for Au cylinders in Be matrix. The opening up of the spectral gaps in a perfectly periodic, binary elastic composite owes, in general, to *five* mismatched parameters involved in the problem. These are the ratio of the mass densities, ratio of the longitudinal velocities, ratio of the transverse velocities, ratio of the longitudinal and transverse velocities, and the filling fraction. The prospects of achieving such band-gaps for acoustic waves in periodic binary system of liquids and/or gases would, however, much improve because only longitudinal modes are supported therein. This means that only *three* parameters will effectively be involved. Both elastic and acoustic cases thus contrast their photonic counterparts where only two dimensionless parameters are involved. It is thus conceivable that the phononic crystals offer a richer — and more complex — behavior, and may require relatively more extreme conditions for the obtention of *complete* band-gaps.

At the outset, it is interesting to remark that in all *artificial* periodic structures the existence of complete gaps is attributed to the joint effect of the Bragg diffraction and the Mie scattering. The destructive interference due to Bragg diffraction accompanied by the Mie resonances due to strong scattering from individual scatterer is the conceptual base of a complete gap. The latter becomes effective when the dimension of the scatterer is close to an integer multiple of wavelength [97]. A complete gap is, by definition, the one that persists independent of the direction of propagation and of the polarization of the wave. However, if the separability of the z and $x-y$ modes is legitimate, as is the case with the two-dimensional (2D) phononic crystals, the term *absolute* is preferred to *complete*, just to avoid the confusion. As a matter of fact, each of these modes can be excited independently of the other, at least in the 2D phononic crystals. Such a separation of the z- and $x-y$ modes suggests an application, namely, a polarization filter. Suppose that the elastic/acoustic waves of arbitrary polarization are incident at the surface of a periodic composite. Then, provided that their frequency lies within a band gap for z modes, the z-polarization component will be totally reflected, and only the $x-y$ modes will be transmitted.

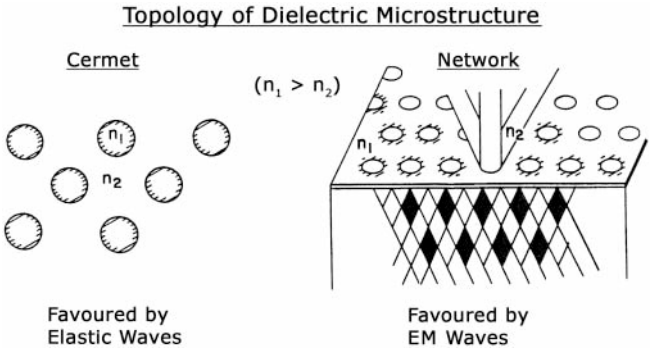

Fig. 2. The cermet topology which is favored by elastic wave consists of high index (low velocity) inclusions in a connected low index (high velocity) background. The network topology favored by EM waves consists of two interpenetrating, connected components.

In conclusion, the literature is a live example that, despite some of the scattered articles [98]–[100] remotely concerned with the subject, research in phononic crystals became more solid [101]–[150]. New ideas emerged for potential device applications, but the driving force was the rich fundamental physics governing the elastic wave propagation in diversely designed phononic crystals. The optimum choice for the design of such phononic crystals which can (and do) exhibit complete large band gaps, irrespective of the dimensionality of the system, is governed by the topology of the resultant structure. The early experience of the two above-mentioned research groups led to infer that it is the cermet topology that favors the creation of elastic/acoustic stop bands as compared to the network topology that favors the creation of the optical band gaps in the photonic crystals. These two topologies are illustrated in Fig. 2. *W note that in describing the results reported in the following sections, we reserve the term elastic (acoustic) waves for the sound/vibrations propagating in inhomogeneous solids (fluids).* In addition, it should be pointed out that we will sometimes recall some equations directly from Ref. [4], without specifying further details. In that sense, the following sections heavily rely on Ref. [4].

5. Longitudinal vibrations

In this section we aim at describing the numerical results on the band structure related problem for longitudinal vibrations, which include both acoustic and elastic waves.

While the former are the well-known modes supported only by the liquids and gases, the propagation of the latter is allowed only within a one-dimensional inhomogeneous medium; two- and three-dimensional inhomogeneous media do not support purely longitudinal elastic waves.

5.1 One-dimensional systems

Here we start with a simplest example for understanding how the band-gaps (or stop-bands) can be realized in a one-dimensional periodic system. This could be visualized as an infinitely long and thin tube of fluid that has been perturbed by a periodic (of period 'd') δ-function-like variations (increases or decreases) in the density along its length. In this situation, the dispersion relation between the Bloch vector K and the (bulk) frequency ω is given by [99]

$$\cos(Kd) = \cos(\varkappa d) - \frac{s}{2}(\varkappa d)\sin(\varkappa d) \equiv f(\varkappa d). \quad (44)$$

Equivalence between Eqs. (44) and (2.42) in Ref. [4] is evident: with $\varkappa = \omega/c_l$, where c_l refers to the longitudinal speed in the bulk between the δ-functions, and $s = \varrho_1 d_1/\varrho_2 d$ is a measure of the strength of δ-functions.

Clearly, Eq. (44) can only be satisfied for $|f(\varkappa d)| \leq 1$. For frequency values $\varkappa d$ where this condition holds, the propagation through the lattice is allowed; for a range of $\varkappa d$ where it is violated, the band-gaps appear. These results are indicated schematically, for $s = 2$, in Fig. 3. Although this proof of the opening up of band-gaps is one dimensional, the scalar nature of the sound field is closely paralleled by the scalar (spinless) Schrödinger electron function that observes energy band structure in many three-dimensional periodic potentials-Kronig-Penney model, for instance, illustrates the similar picture. From the plots of two step functions $\pm\theta[1 - |f(\alpha)|]$, with $\alpha = \varkappa d$, as bold solid line, one can see enclosed by rectangles the first three propagation windows, each of which begins at $\alpha = n\pi$; $n = 0, 1, 2$. The condition $\alpha = n\pi$ implies $d = n(\lambda_k/2)$ and hence occurs when an integer number of half wavelengths of a normal-mode wave function fits across one period interval of length d. In order to probe the acoustic band, as depicted in Fig. 3, Dowling [99] also considered the steady-state power output of a localized source in the tube of fluid with a periodically varying density. The computed radiated energy from such a source led him to infer that it would be possible to quench these sources at the frequencies lying within the band-gaps, while amplifying their outputs in the propagation windows. This is analogous to the behavior of one-dimensional "atom" radiating electromagnetically between one-dimensional mirrors.

Next we turn to the propagation of elastic waves in one-dimensional superlattice systems. Longitudinal modes in such systems are supported in the situation discussed in the beginning of Sec. 2.5 in Ref. [4]. Here we are concerned with a binary superlattice system made up of alternate layers of Al and epoxy [100]. The band structure for longitudinal elastic waves propagating in this system is depicted in Fig. 4. Numerical results in this figure are based on Eq. (2.41), with c_{ti} replaced by c_{li} and the propagation vector $\vec{k}_{\|} = 0$. The layering gives rise to the splitting of longitudinal waves with Bloch vector $q = \pm 2n\pi/d$; d being the period. In general, real q leads to the allowed bands and imaginary q to the band-gaps. Inset in Fig. 4 shows the reflectivity as a function of frequency. As it is expected, the reflectivity approaches unity for the frequencies lying within the band-gaps. One also notes (see Fig. 4 in Ref. [100]) that the width of the allowed and forbidden bands decreases with increasing period. This results is, however, not unique to the elastic band structure; similar behavior has been noted for the electrons in crystal lattices and for plasmons in metallic or semiconductor superlattices.

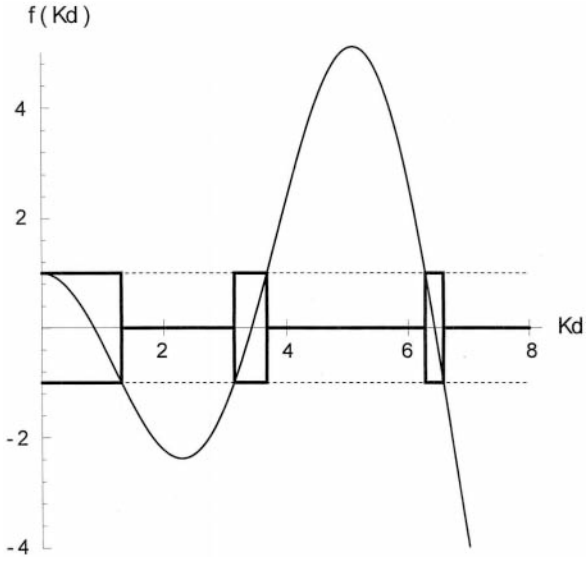

Fig. 3. We plot here as a solid curve, the right-hand side of the dispersion relation, Eq. (44), denoted by $f_s(\alpha)$, where $\alpha = \varkappa d$ and take a δ function of strength $s = 2$. The dashed lines represent $f_s(\alpha) = \pm 1$. From the condition $|f_s(\alpha)| \leq 1$, we can see that sonic band gaps occur when this inequality is violated and sonic passbands occur when it is obeyed. If we plot the two step functions $\pm\theta[1 - |f_s(\alpha)|]$ as bold solid lines then we see enclosed by solid rectangles the first three passband regions, each of which begins at $\alpha = n\pi$, $n = 0, 1, 2$. The condition $\alpha = n\pi$ implies $d = n\lambda_k/2$ and hence occurs when an integer number of half-wavelengths of a normal-mode wave function fits across one period interval of length d. (After Dowling, Ref. [99]).

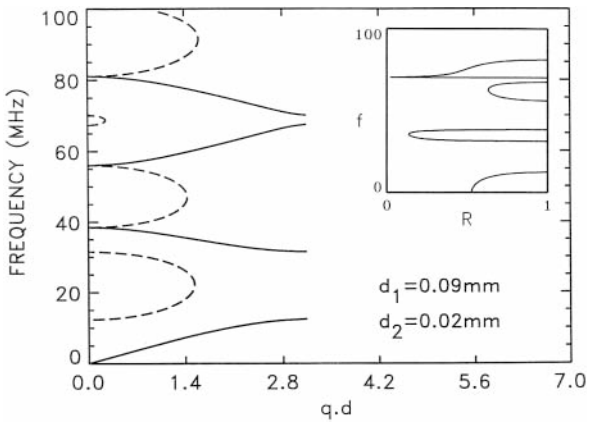

Fig. 4. Band structure for the longitudinal elastic waves propagatling in a periodic layered binary system. Computation was performed for Al ($d_1 = 0.09$ mm)/epoxy ($d_2 = 0.02$ mm) system. The inset shows the reflectivity as a function of frequency for the corresponding semi-infinite system. (After Esquivel-Sirvant and Cocoletzi, Ref. [100]).

This can be understood by realizing that large separation of elastic films reduces the coupling strength between the (surface) excitations on each film, which in turn reduces the band-widths – a result similar to the reduction in band-width for electronic states when the atoms are moved farther apart. Other factor that does influence the band structure is the ratio of the sound speeds in the two media of the unit cell.

Finally, we present some band structure results for longitudinal (acoustic) wave propagation in a system made up of N' dangling side branches (DSB) periodically grafted at each of the N equidistant sites on a slender tube [112]. For the sake of simplicity, we embark on the simpler system of air and/or water tubes. Of course, in practice, the gas or liquid within these tubes would be contained by means of some latex material. The mass density and speed of sound in rubber are comparable to those of water [see, e.g., C.R.C. Handbook of Chemistry and Physics, 66th Edition (CRC Press, Florida, 1985), p. E-43]. Hence for a sufficiently thin latex partition, the presence of this third extra layer should not affect the calculations significantly and, in fact, we will neglect it. We have considered the situation both for open and closed tubes. Evidently, the relevant parameters involved in the problem are ϱ_i, v_i, d_i, and a_i; as well as the integers N and N'; with subscript $i \equiv 1(2)$ for slender tube (DSB). For the reasons of space, we will discuss only the results for $N' = 1$. It is worth mentioning that the validity of our results is subject to the requirement $\sqrt{a_i} \ll d_i$, λ. It should also be pointed out that the methodology employed in this particular work is based on the interface response theory of Dobrzynski [Surf. Sci. Rep. **6** (1986) 119].

Figure 5 shows the band structure and the transmission coefficient for the open tubes with identical media inside the DSB and the slender tube. The opening up of the stop bands in the band structure is very well substantiated by the transmission spectrum. Most important aspect of these results is the cutoff frequency Ω_c below which no propagation at all is allowed. This gives rise to the utter discretization of the propagation starting right from zero frequency. As regards the regular repetitive pattern of the band structure (and the transmission spectrum), one can easily understand this from Eq. (3) in Ref. [112]. For instance, for identical media inside the DSB and the slender tube, Eq. (3) simplifies to $\Omega = \cos^{-1}[(2/3)\cos(kd_1)] + 2n\pi$; where $\Omega = q_1 d_1 / v_1$ is the reduced frequency, $-\pi \leq kd_1 \leq +\pi$, and n is an integer (including zero). This clearly suggests the periodic pattern depicted in Fig. 5, where the cutoff frequency Ω_c is defined by the lowest frequency of the lowest mode ($n = 0$) at the zone center. Other details regarding the physical conditions subject to the material (ϱ_i and v_i) and geometrical (d_i and a_i) parameters required to achieve the complete stop bands can be seen in Ref. [119]. Note that the situation is dramatically different at $d_2/d_1 = 0.5$, where the aforesaid conclusion may be seen to fail as compared to the neighboring cases – every pair of bands (counting from the bottom) becomes degenerate at the zone boundary to form a closed loop. What is important to note is that the existence of the lowest gap below Ω_c is more often the rule than the exception: its magnitude varies with the variation of both material and geometrical parameters, though.

The numerical results for a system of closed tubes with identical material media inside the slender tube and the DSB are illustrated in Fig. 6. There are two major differences when compared to the case of open tubes: the lowest gap extending up to zero has disappeared, and the unit cell of the repetitive pattern now contains four bands (as compared to *two* in Fig. 5. The numerical results for a system of closed tubes with the identical material media inside the slender tube and the DSB are illustrated in Fig. 6. There are two major differences as compared to the case of open tubes: the lowest gap extending up to zero

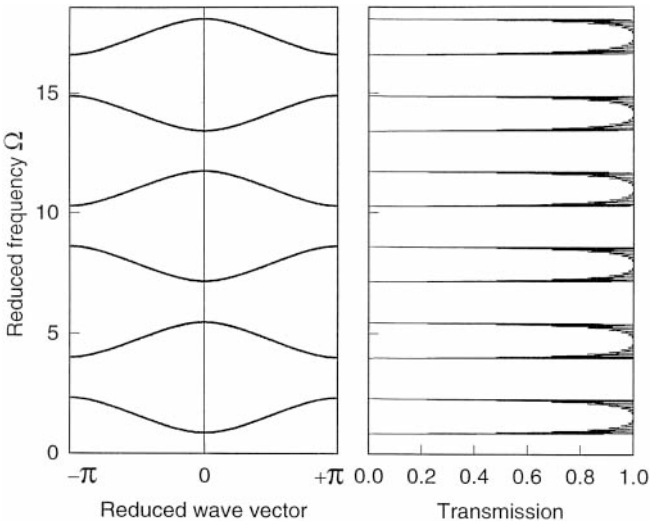

Fig. 5. Band structure (left panel) and transmission spectrum (right panel) for the system of open tubes. Reduced wave-vector refers to the dimensionless Bloch vector kd_1 and the reduced frequency is defined by $\Omega = \omega(d_1/v_1)$. We consider identical fluid (air or water, for example) both inside the dangling side branches (DSB) and inside the slender tube. The material and geometrical parameters are such that $\varrho_2/\varrho_1 = 1$, $v_2/v_1 = 1$, $d_2/d_1 = 1$, and $a_2/a_1 = 1$. We call attention to the periodic pattern of the band structure and the lowest gap below the lowest frequency (referred to as the cutoff or threshold frequency Ω_c in the text) at the zone center. In the right panel $N = 20$ was considered; $N' = 1$ everywhere. (After Kushwaha *et al.*, Ref. [112]).

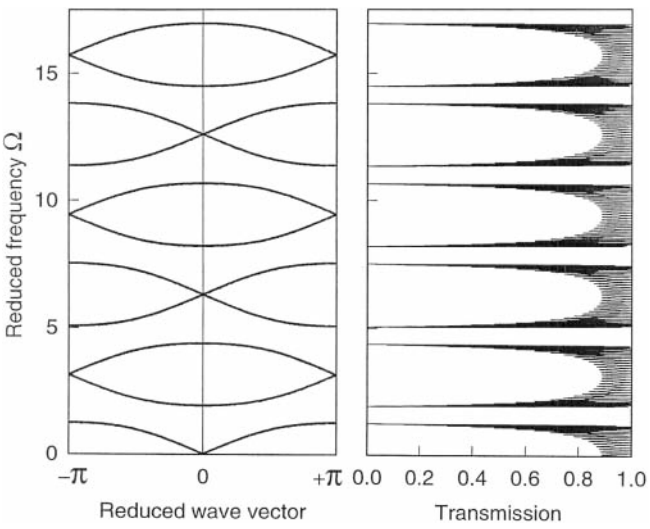

Fig. 6. The same as in Fig. 5, but for a system of closed tubes. Note that the unit cell of the periodic pattern now contains *four* bands as compared to *two* in Fig. 4 and that the lowest gap pertaining to the system of open tubes no longer exists. (After Kushwaha *et al.*, Ref. [112]).

has disappeared, and the unit cell of the repetitive pattern now contains four bands (as compared to *two* in Fig. 5). There are full intracell gaps – but no intercell gaps. The repetitive pattern observed in the band structure (and the transmission spectrum) can be understood through a simple analysis of Eq. (4) in Ref. [112]. Again, the formation of the band at $d_2/d_1 = 0.5$ is unique where all the closed loops, like the one formed by the second and third bands from the bottom, disappear altogether.). There are full intracell gaps – but no intercell gaps. The repetitive pattern observed in the band structure (and the transmission spectrum) can be understood through a simple analysis of Eq. (4) in Ref. [112]. Again, the formation of the band at $d_2/d_1 = 0.5$ is unique where all the closed loops, like the one formed by the second and third bands from the bottom, disappear altogether.

Figure 7 illustrates the evolution of the transmission spectrum with increasing number of N for the case of open tubes. We present the results for the case of identical fluids inside the slender tube and the DSB. For $N = 1$ (the uppermost panel), the transmission coefficient becomes immeasurably small (but never approaches *exactly* zero) at the midgap frequency corresponding to the larger N. For smaller N, vanishingly small transmission represents the low density of states which are referred to as pseudogaps. It is observed that as N increases the pseudogaps gradually turn into the complete gaps (with transmission equal to zero). However, it is interesting to note that the magnitude of the gap remains the same for $N \geq 5$. The number of oscillations in the transmission coefficient within the passband has been noted to be unfailingly N or $N - 1$.

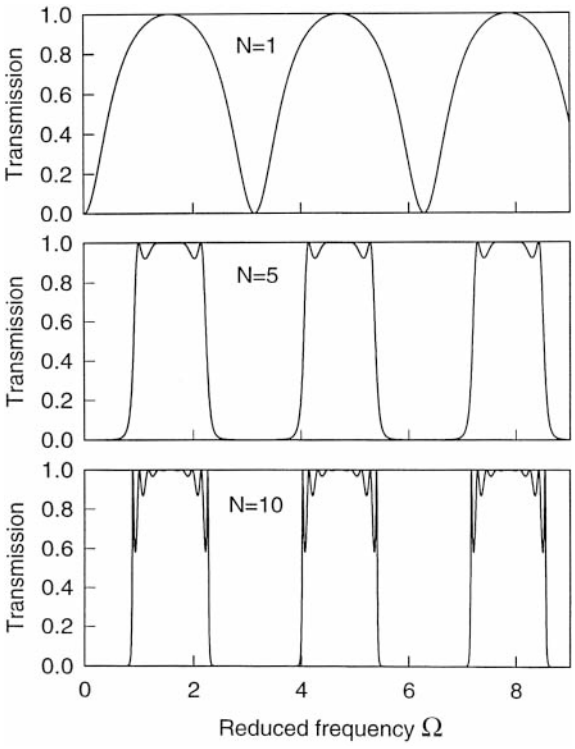

Fig. 7. Evolution of the transmission spectrum as a function of N for a system of open tubes. Note that as N increases the visible slopes in the minimum of the transmission diminish and ultimately vanish. The parameters (both material and geometrical) are the same as in Fig. 5. (After Kushwaha *et al.*, Ref. [112]).

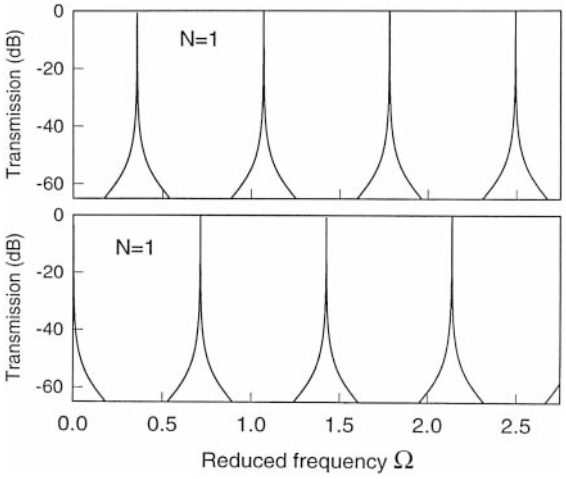

Fig. 8. *Discrete* transmission spectrum for a system of open tubes of *airy* dangling side branches grafted on a slender *water* tube for $N = 1$. The geometrical parameters are the same as in Fig. 5. Existence of the lowest gap is noteworthy. (After Kushwaha *et al.*, Ref. [112]).

The crux in this work [112] was on the results for the transmission spectrum depicted in Fig. 8. This refers to a simplest geometry of a long slender tube with airy DSB. We consider the length of the DSB equal to the period of the system (i.e., $d_2 = d_1$) and the cross-sections of the DSB and the slender tube are also taken to be the same (i.e., $a_2 = a_1$). The upper (lower) panel demonstrates the transmission spectrum for the system of open (closed) tubes. Apart from the fact that the transmission coefficient does not approach *exactly* zero – it remains at immeasurably small height above zero – the magnitude of the stop bands for $N = 1$ was seen to be surprisingly the same as for $N \gg 1$. This is found to be true for the systems of both open and closed tubes. Note that the lowest gap for the open tubes persists below the cutoff frequency. The discretization of the transmission spectrum is attributed to the presence of the DSB (whose number in the case at hand is just *one*) that suppresses the transmission over almost the whole range of frequencies except for those defined by $C_2 = 0$ ($S_2 = 0$) for open (closed) tubes. That this so can easily be seen through a careful diagnosis of the expression of transmission coefficient T in Eq. (5) for $N = 1$ [112]. This refers to a simplest geometry of a long slender tube with airy DSB. We consider the length of the DSB equal to the period of the system (i.e., $d_2 = d_1$) and the cross-sections of the DSB and the slender tube are also taken to be the same (i.e., $a_2 = a_1$). The upper (lower) panel demonstrates the transmission spectrum for the system of open (closed) tubes. Apart from the fact that the transmission coefficient does not approach *exactly* zero – it remains at immeasurably small height above zero – the magnitude of the stop bands for $N = 1$ was seen to be surprisingly the same as for $N \gg 1$. This is found to be true for the systems of both open and closed tubes. Note that the lowest gap for the open tubes persists below the cutoff frequency. The discretization of the transmission spectrum is attributed to the presence of the DSB (whose number in the case at hand is just *one*) that suppresses the transmission over almost the whole range of frequencies except for those defined by $C_2 = 0$ ($S_2 = 0$) for open (closed) tubes. That this so can easily be seen through a

careful diagnosis of the expression of transmission coefficient T in Eq. (5) for $N = 1$ [112].

5.2 Two-dimensional systems

In this section we discuss the exciting possibility of creating *complete* acoustic band-gaps in a two-dimensional system made up of liquids. We chose water pipes of circular cross-section immersed in mercury which can be arranged to have two macroscopic geometries of interest-square and hexagonal lattices. Analytical results for the longitudinal waves propagating in such systems are describable in the framework of Eq. (2.67) in Ref. [112], with $\vec{k}$ and $\vec{g}$ being the two-dimensional vectors. The relevant expressions for the filling fraction f and the structure factors $F(G)$ are given by

$$f = \begin{cases} \pi(r_0/a)^2, & \text{for square lattice} \\ \dfrac{2\pi}{\sqrt{3}}(r_0/a)^2, & \text{for hexagonal lattice} \end{cases} \tag{45}$$

and

$$F(G) = 2fJ_1(Gr_0)/(Gr_0)\ , \tag{46}$$

where a and r_0 are, respectively, the lattice constant and the radius of the pipes. $J_1(x)$ is the Bessel function of the first kind of order one. Our choice of the specific materials (i.e., water and mercury) was motivated by the density contrast; although there is no substantial contrast in the speed of sound in liquids, in general. The longing question of how to sustain water pipes in mercury and the role played by the latex material which the walls of the pipes are made of will be discussed later in this section. The standard eigenvalue problem represented by Eq. (2.70) in Ref. [112] was solved to obtain real eigenfrequencies. A good convergence (of better than 1%) was achieved by limiting the number of plane waves to 361, in both square and hexagonal geometries. To be more explicit, the integers n_x and n_y, in the reciprocal lattice vector $\vec{G}$, were permitted to take the values between -9 and +9 (i.e., 361 plane waves). As discussed below, multiple low-frequency band-gaps were found for both geometries [105]. However, the width of the lowest (and the widest) band-gaps, for the same value of filling fraction, is found to be larger in the hexagonal pattern than in the square pattern.

Figure 9 illustrates the density of states (DOS) for a square pattern of infinitely long, circular water pipes in mercury that occupy 35% of the total area. The computation of DOS involves 4950 $\vec{k}$-points covering the boundaries as well as the interior of the irreducible part of the first Brillouin zone. DOS curve depicts vividly the existence of two *complete* acoustic band-gaps appearing within the first ten bands. The first gap opens up between the first (with $\bar{M}_{1\,\max}$) and the second (with $\bar{X}_{2\,\min}$) bands. Similarly, the second band-gap exists between fourth ($\bar{X}_{4\,\max}$) and fifth ($\bar{X}_{5\,\min}$) bands. It is worth mentioning that one can choose to plot as many or as few bands as one likes, albeit the computer does calculate all (i.e., $(2n+1)^2$ bands; $n = 9$ in the present case) bands. We have noticed that if we plot first 50 bands, there appear several narrow but *complete* band-gaps at higher frequencies. Again, this is true for both square and hexagonal lattices.

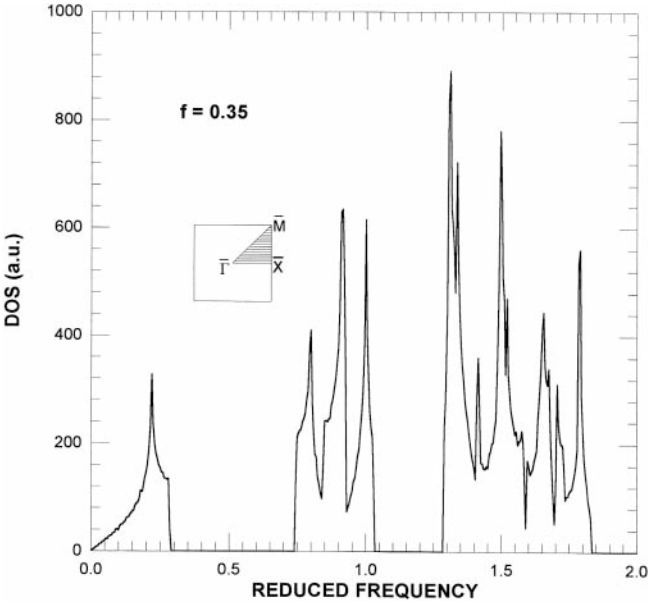

Fig. 9. Computed DOS for acoustic waves in a 2D periodic system of circular water pipes in mercury. The filling fraction $f = 0.35$. The computation involves 4950 $\vec{k}$-points covering the boundaries as well as the interior of the irreducible triangle $\bar{\Gamma}\bar{X}\bar{M}$ of the first Brillouin zone. The material parameters are: $\varrho = 1.025$ (13.5) gm/cm^3, $c_l = 1531$ (1450) m/sec for sea-water (mercury). We call attention to the two wide spectral gaps: The first gap opens up between the first (with $\bar{M}_{1\,\max}$) and second (with $\bar{X}_{2\,\min}$) bands; the second gap occurs between fourth (with $\bar{X}_{4\,\max}$) and fifth (with $\bar{X}_{5\,\min}$) bands. (After Kushwaha and Halevi, Ref. [105]).

We summarize the existence of the lowest, which is always the widest, band-gap for the whole range of filling fraction and for both geometries in Fig. 10. The curve designated as SWM (HWM) refers to the square (hexagonal) lattice with water pipes in Mercury. The reverse (i.e., mercury pipes in water host) is the case with the curves labeled as SMW and HMW. One can easily notice that in each case there is a certain minimum value of the filling fraction, $f_{\min}$, for a gap to be opened; and likewise there is a certain maximum, $f_{\max}$, where the gaps cease to exist. For the square lattice, with water pipes in mercury host (SWM), $f_{\min}(f_{\max})$ is defined as 0.017 (0.77); and for hexagonal lattice, $f_{\min}(f_{\max})$ is given by 0.008 (0.79). It is noticeable that the gaps cease to exist before the close-packing is attained – close packing corresponds to the geometrical pattern when the containers of the inclusions (pipes in the present case) start touching each other. The close-packing in the square (hexagonal) lattice is defined by $f = 0.7854$ (0.9069); these values of f correspond to $r_0 = a/2$.

Let us now describe briefly the situation when the mercury pipes are embedded in the water as a host. The computation of the lowest (and the only ones) band-gaps versus filling fraction is demonstrated by the curves labeled as SMW and HMW, respectively, for square and hexagonal lattices in Fig. 9. In this case the $f_{\min}(f_{\max})$ is given by ~ 0.35 (0.7854) for the square lattice; the corresponding values for the hexagonal lattice are $\sim$0.48 (0.822). It is noteworthy that while SMW refers to the lowest band-gap existing between the first and the second bands; HMW stands for the gap occurring between the third (with $\bar{\Gamma}_{3\,\max}$) and fourth (with $\bar{X}_{4\,\min}$) bands. In this situation there are no other band-gaps at least as far as 50th band. This comment is valid for both geometries.

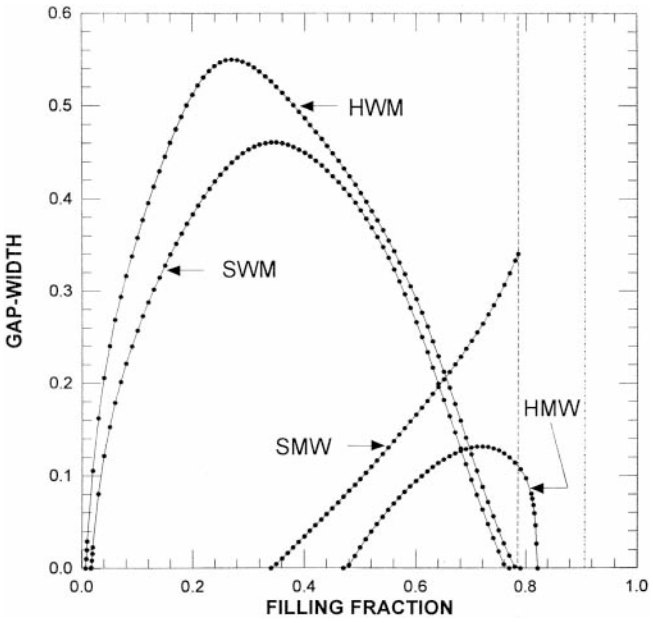

Fig. 10. Normalized gap-widths of the lowest band-gaps as a function of filling fraction f. The curves designated as SWM (HWM) refer to the square (hexagonal) lattice with water pipes in mercury. The reverse (i.e., mercury pipes in water) is the case with the curves labelled as SMW and HMW. The material parameter are the same as in Fig. 8. The dashed and dashed-dotted vertical lines refer to the close-packing values of the filling fraction for square and hexagonal lattices, respectively. (After Kushwaha and Halevi, Ref. [105]).

An extensive investigation of this specific two-dimensional inhomogeneous system of liquids leads us to infer that low-density, high-velocity inclusions in the high-density, low-velocity host is the optimum geometry for the obtention of multiple wide band-gaps and hence for the localization of the acoustic waves in a weakly disordered system. This finding is in entire agreement with our conclusion drawn in the case of cubic arrays of spherical gaseous balloons in air (see the following subsection). However, this does disagree with the conclusion [6] that the optimum case for the appearance of gaps or for the localization of acoustic waves is low-density, low-velocity spheres occupying a volume fraction of the order of 10% of the host material. It should be emphasized, however, that this was the conclusion arrived at on the basis of a calculation carried out for fictitious material parameters by the authors of Ref. [6].

Now we turn our attention to the latex material – considering the optimum geometry where the water pipes are embedded in mercury host. In the latex material (i.e., inside the walls of the pipes) both transverse and longitudinal vibrations are allowed. As such, it is quite likely that these shear oscillations produce a finite DOS within the acoustic band-gaps. We expect, however, that this DOS should be very small if the walls of the pipes are thin enough. We estimated the error involved in neglecting the *longitudinal* vibrations in the latex by calculating the correction to $\sigma(\vec{G})$, Eq. (3.60) in Ref. [4], due to a circular shell of thickness Δ and mass density ϱ_w. Provided that $\varrho_w > \varrho_b (> \varrho_i)$ and $\Delta \ll r_0$, this correction is given by [4]

$$\sigma_w(\vec{G}) = \varrho_w^{-1} \left[\delta_{\vec{G},0} + \left(\frac{\Delta}{r_0} \right) E(\vec{G}) \right], \tag{47}$$

where $E(\vec{G})$ is a function of the same order of magnitude as $F(\vec{G})$, Eq. (3.3) in Ref. [4]. A careful look at Eqs. (2.60) and (3.4) in [4] reveals at once that these compressive oscillations in latex wall would not alter our results significantly provided that $(\Delta/r_0) \ll (\varrho_w/\varrho_i - \varrho_w/\varrho_b)$. The left-hand side of this inequality is assumed to be much less than one, whereas the right-hand side is indeed much greater than one if ϱ_i is considerably smaller than ϱ_b, as is the case for water pipes in mercury. A remark made on the rubber as the latex material in the previous section is still valid here.

It is worth noting that a simple two-dimensional inhomogeneous system of liquids as the one discussed in this section exhibited the widest band-gaps reported for elastic, acoustic, or optical waves up to that time. To justify this comment, we calculate the gap/mid-gap ratios for both the square and hexagonal patterns, respectively, for $f = 0.34$ and 0.27. The result is a gap/mid-gap ratio for square (hexagonal) lattice of 0.901 (0.984). These were, to our knowledge, the largest numbers that define the magnitude of the acoustic band-gaps; irrespective of whether the systems studied in the past were solids, fluids, or gases [100]–[122]. Recently, the 2D (3D) systems of airy cylinders (air bubbles) in water have been shown to exhibit even larger band gaps, with a gap/midgap ratio of 1.8 [113, 114]; these remain to be the widest gaps ever reported for photonic and/or phononic crystals to date. Within these band-gaps the sound and longitudinal vibrations are forbidden and the total silence prevails.

The simplest way of realizing such acoustic band-gaps in two-dimensional periodic systems is to embed the infinitely long thin water pipes in a substrate that forms a bottom of mercury tank. If the bottom is smooth, one should obtain the *complete* acoustic band-gaps – otherwise (i.e., if the bottom is rough or non-periodic) one should be able to observe the localized acoustic modes existing within these gaps [79].

5.3 Three-dimensional systems

Now we focus on the longitudinal modes propagating in an inhomogeneous three-dimensional system comprised of liquids and/or gases. The methodology used for computing the band structure in such systems is the one discussed above (see Sec. 2.6 in Ref. [4]). Here we discuss our numerical results on the band structure of cubic arrays of spherical balloons in *fcc*, *bcc* and *sc* arrangements. The filling fraction f and the structure factor $F(\vec{G})$ for such geometries are given by

$$f = n \, \frac{4\pi}{3} \left(\frac{r_0}{a} \right)^3 \tag{48}$$

and

$$F(\vec{G}) = \frac{1}{V_c} \int_a d^3 r \cdot \mathrm{e}^{-i\vec{G}\cdot\vec{r}} \tag{49}$$

$$= \frac{3f}{(Gr_0)^3} \left[\sin(Gr_0) - (Gr_0)\cos(Gr_0) \right], \tag{50}$$

where n, r_0, and a are, respectively, the number of spheres in the *unit* cell, radius of the sphere, and the lattice con-

stant. We made use of Eq. (2.70) in Ref. [4] to compute the band structure of *fcc*, *bcc*, and *sc* arrays of hydrogen balloons in air [107]. For a realistic situation where all three media (i.e., gas inside the balloons, the latex walls, and the background gas) were considered, we obtained the real eigenvalues and good convergence (of better than 2%) by limiting the number of plane waves to 343. *Complete* band-gaps were found for *fcc* and *bcc* geometries; however no gap was obtained for *sc* lattice. Numerical results for the *fcc* arrangement of balloons that occupy 35% of the total volume are depicted in Fig. 11. The left panel of Fig. 10 shows the band structure in the principal symmetry directions in the Brillouin zone. The middle panel is the result of an extensive scanning of $|\vec{k}|$ in the irreducible part of the first Brillouin zone – including the interior of this zone and its surface, as well as the principal directions shown in the left panel. The right panel illustrates the density of states whose computation is based on the scanning of $|\vec{k}|$ depicted in the middle panel. There appears a *complete* acoustic band-gap between the first and the second bands, and there are no more gaps at least as far as the 50th band. Three panels together establish that this is, indeed, a *complete* gap, irrespective of the direction of propagation. Similar results are obtained for the *bcc* geometry; the *sc* geometry did not observe a *complete* gap for any value of filling fraction, however.

The dependence of the (lowest) band-gap on the filling fraction, for *fcc* and *bcc* structures is summarized in Fig. 12. It is found that the filling fraction must exceed a certain minimum value, $f_{\min}$, for opening up of a gap. If the pressure inside the balloons is 1.1 atm, then for *fcc* (curve A) and *bcc* (curve E) structures $f_{\min} \simeq 0.12$ and 0.21, respectively. The corresponding maximum values are $f_{\max} \simeq 0.63$ and 0.54. For any value of filling fraction, the *fcc* structure gives a wider band-gap than the *bcc* structure. For both lattices, the band-gaps are widest when $f \simeq 0.38$, that is when the balloons occupy 38% of the

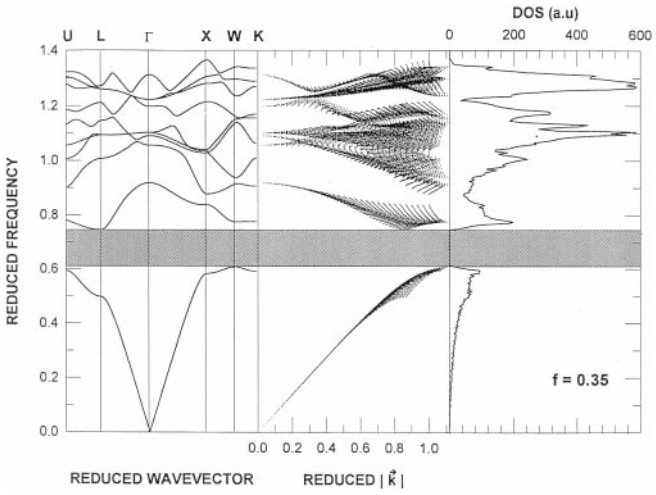

Fig. 11. Acoustic band structure for an fcc array of spherical balloons containing hydrogen gas in air (left panel of triptych). Middle part: frequency eigenvalues as a function of $|\vec{k}|$ (the magnitude of the Bloch vector) scanned throughout the irreducible part of the Brillouin zone. DOS as a function of reduced frequency is graphed in the right panel of the figure. The hatched area refers to the spectral gap for sound or vibrations. The parameter contrast are $\varrho(H_2)/\varrho(\text{air}) = 0.076$ and $c_l(H_2)/c_l(\text{air}) = 3.706$. (After Kushwaha and Halevi, Ref. [107]).

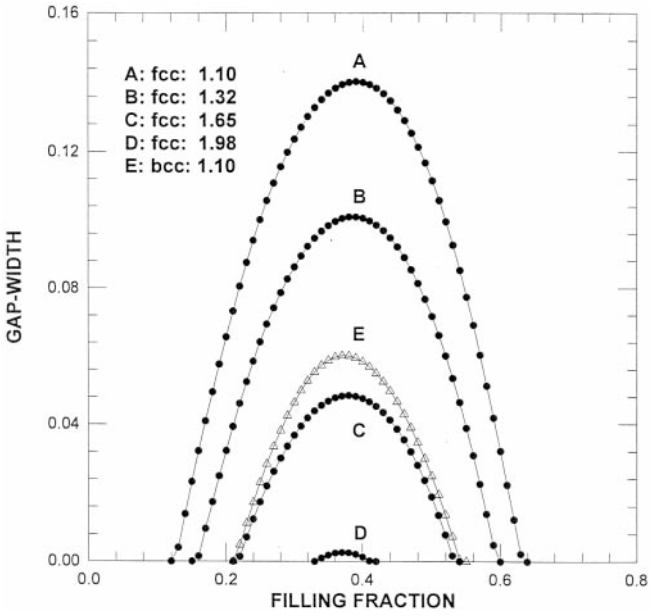

Fig. 12. Normalized gap-widths versus filling fraction f for *fcc* and *bcc* structures (there is no gap for *sc* structure). For both structures the largest gap is obtained for $f \simeq 0.38$, and, for a pressure $p = 1.10$ atm, the approximate gap/midgap ratios are 0.2 and 0.1 for the *fcc* (curve A) and *bcc* (curve E) lattices, respectively. The variation of the gap with pressure is also shown for *fcc* structure. As p increases to 1.32 atm (curve B), 1.65 atm (curve C), and 1.98 atm (curve D), the gap gradually disappears. (After Kushwaha and Halevi, Ref. [107]).

space. However, the gap/midgap ratio is considerably larger for *fcc* array – about 0.2 (0.1) for *fcc* (*bcc*). The curves B, C, and D (in Fig. 12) illustrate what happens when the pressure inside the balloons is successively increased to 1.32, 1.65, and 1.98 atms – considering the *fcc* structure. This leaves the speed of sound unaltered, though the density contrast decreases. If the pressure inside is almost twice the pressure outside, the density contrast is about 7, and the band-gap almost disappears (see curve E). It is then apparent that, for high-velocity balloons in a low- velocity host, the band-gaps can exist only if the density of the (gas inside the) balloons is considerably smaller than the density of host.

A word on the latex material which the wall of the balloons is made of is in order. In this substance transverse, as well as longitudinal, vibrations are permitted. It is quite likely that these shear oscillations produce a finite density of states (DOS) within the acoustic band-gaps. We expect, however, that this DOS should be very small provided that the balloon's wall is thin enough. We estimated the error involved in neglecting the *longitudinal* waves in the latex by calculating the correction to $\sigma(\vec{G})$, Eq. (2.60), due to a spherical wall of thickness w and mass density ϱ_w. If $\varrho_w \gg \varrho_b (> \varrho_i)$ and $w \ll r_0$, this correction is [4]

$$\sigma_w(\vec{G}) = \varrho_w^{-1} \left[\delta_{\vec{G},0} + \left(\frac{w}{r_0} \right) H(\vec{G}) \right], \tag{51}$$

where $H(\vec{G})$ is a function of the same order of magnitude as $F(\vec{G})$, Eq. (50). By comparing Eqs. (51) and (2.60) in Ref. [4], we see that the compressive oscillations of the latex wall are not expected to alter significantly our results provided that $w/r_0 \ll (\varrho_w/\varrho_i - \varrho_w/\varrho_b)$. The left-hand

side of this inequality has been assumed to be much smaller than one, while the right-hand side is indeed much greater than one if ϱ_i is substantially smaller than ϱ_b, just as is the case for hydrogen balloons in air. We recall the remark made in the previous section on rubber as the latex material.

Within the gaps of Figs. 11 and 12, the perfectly periodic "phononic" crystals, stand still and total silence reigns. The situation is of comparable interest to the full photonic band-gaps in periodic dielectric composites [151]. These, however, were realized only with certain complex structures of the *fcc* unit cell – not with the simple *fcc* lattice, and much less for *bcc* and *sc* lattices. The cubic arrays of balloons discussed here are probably the simplest physical systems that exhibit *complete* band-gaps.

Similar theoretical investigations on the band structures for cubic arrays of spherical water balloons surrounded by mercury host exhibit multiple, complete acoustic stop bands for all the three (*fcc*, *bcc*, and *sc*) arrangements [106]. These stop bands are seen to be widest for a volume fraction $f \approx 24\%$ and the corresponding gap/midgap ratios are about 0.83, 0.77, and 0.62, respectively, for *fcc*, *bcc*, and *sc* lattices. In the reverse situation, where mercury balloons are surrounded by water, the gaps obtained are found to be surprisingly small.

6. Transverse vibrations

As one can see from the analysis presented in Sec. 5 in Ref. [4], the propagation of purely transverse modes is permissible only in one- dimensional periodic systems, superlattices, for examples, and two-dimensional periodic elastic composites; three-dimensional periodic composites do not allow the resolution of this polarization. In this section, we would discuss the transverse modes propagating in the infinite and semi-infinite elastic superlattices. The main emphasis would be laid on the creation of elastic band-gaps in two-dimensional periodic, both square and hexagonal patterns, elastic composites. These elastic composites are made up of an array of infinitely long, thin rods of an isotropic solid "i" and embedded in a different elastic background "b", which is also isotropic. The intersection of the parallel rods with a perpendicular plane form a square or hexagonal lattice. There is a translational invariance in the direction $\hat{z}$ parallel to the rods and the system has a two-dimensional periodicity in the transverse $(\hat{x} - \hat{y})$ plane. As already mentioned, we will confine to the transverse modes with $\vec{u} = \hat{z}u$ and $\vec{\nabla} \cdot \vec{u} = 0$. The justification lies in the fact that this is the only case when the general wave equation for inhomogeneous solids greatly simplifies.

6.1 One-dimensional systems

The problem of elastic wave propagation has been the subject of numerous theoretical and experimental studies during the past decade (see for example Sec. 1 in Ref. [4]). The extended states propagating in a superlattice of infinite extent form the bulk bands which are separated by small gaps. The surface phonon-polaritons, which are the elastic waves localized at and decaying exponentially away from the interfaces, may exist within these gaps. The spatial location of these surface modes in the $\omega - k_{\|}$ plane much depends on the way an otherwise perfectly periodic superlattice system is truncated. For the details of these mechanisms, the reader is referred to the recent work by Djafari-Rouhani and collaborators [152, 153]. Here we are interested to give a taste for the simplest geometry where the periodicity of the superlattice is truncated with a semi-infinite homogeneous elastic medium. The dispersion relation for such a semi-infinite superlattice system was derived by Camley *et al.* [154] almost two decades ago. The results is

$$F_1 \tanh(\alpha_1 d_1) + F_2 \tanh(\alpha_2 d_2) = 0 \tag{52}$$

where the symbols have the same meanings as defined in Sec. 2.5 in Ref. [4]. In order to examine the effect of perturbing the periodicity of the superlattice, one has to solve Eq. (2.41) in Ref. [4], which describes the bulk bands, and Eq. (57), which traces the dispersion of the surface modes, independently. The existence of the surface modes is characterized not only by the relative thickness but also by the parameter contrasts (in the densities and speed of sound in the two layers of a binary superlattice, as well as in the surface layer and the truncating medium).

Figure 13 illustrates the numerical example for the Nb–Cu superlattice system. One can notice that the dispersion curves for the periodic system break up into different bulk bands depending on the value of Kd, where K denotes the Bloch vector and d is the period of the superlattice. The band edges exist at $Kd = n\pi$, $n = 0, 1, 2, \ldots$ These bulk bands are depicted by hatched areas. The surface modes, drawn by dotted curves, exist below the lowest bulk band and within the gaps between the bulk bands. The existence of the surface modes within the gaps be-

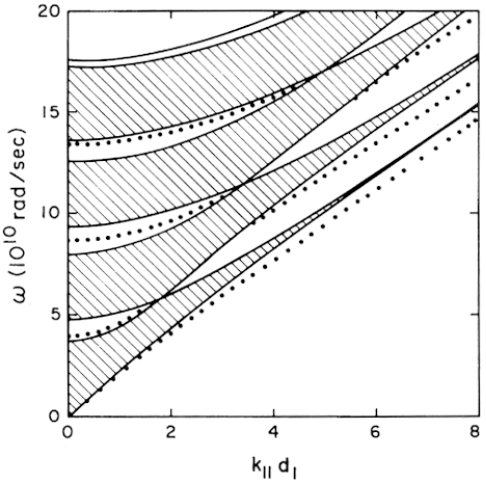

Fig. 13. Band structure for transverse elastic modes propagating in a one-dimensional superlattice system. The hatched areas show the bulk bands for an infinite periodic system and dotted curves refer to the surface modes in a truncated semi-infinite superlattice. The lowest surface mode merges with the lower edge of the lowest bulk band as the parallel component of the wave vector $\vec{k}_{\|} \to 0$. The edges of the bulk bands correspond to the Bloch vector $k = n\pi/d$, where d is the period and $n = 0, 1, 2, \ldots$ The computation is performed for Nb ($d_1 = 1000$ Å)/Cu ($d_2 = 500$ Å) system. (After Camely *et al.*, Ref. [154]).

tween the bulk bands was, in fact, predicted by Auld and collaborators [155] much before the superlattice era came into being.

Authors of Ref. [154] argue that the surface mode lying below the lowest bulk band is similar to the Love modes, which by definition are the guided modes of an unsupported plate, in several respects. This surface mode exists only when the outermost layer has the lower c_t. In the limit of $\vec{k}_{\|} \to \infty$, the velocity of this mode approaches the sound velocity of the outermost layer. Another characteristic of this surface mode is that it has a sinusoidal variation through the layers of lower c_t and an exponential decay through those of higher c_t. The surface modes that lie within the gaps between the bulk bands, on the other hand, have sinusoidal variations through both layers, and they do exist even if the outermost layer has a higher c_t. For the relevant details on the surface modes in the semi-infinite medium (Reyleigh waves), in the unsupported media with sagittal polarization (Lamb waves) and shear-horizontal polarization (Love waves), and in the supported media with sagittal polarization (Sezawa waves), the reader is referred to Ref. [156].

6.2 Two-dimensional systems

By two-dimensional systems we mean the elastic (binary) composites which are synthesized to exhibit two-dimensional periodicity in the plane perpendicular to infinitely long elastic rods embedded in a background with different elastic properties. This leads us to realize two different geometries – square lattice and hexagonal lattice. In both of these geometries, we would confine our attention to the elastic rods of circular cross-section; other possibilities on the shape of the inclusions have been considered in the literature (see, for example, Refs. [97] and [103]). It is noteworthy that although the eigenvalue problem for both hexagonal and square lattices is describable formally by the same Eq. (3.38) in Ref. [4], the two structures are distinguishable through the values attained by $\vec{K}$, $\vec{G}$ and the structure factor $F(\vec{G})$. This is true whether or not the same shape of inclusions is considered for both geometries.

6.2.1 Square lattices

Since we consider an array of cylinders of circular cross-section, the structure factor $F(\vec{G})$ is specified by Eq. (46). The secular equation used to compute the band structure is Eq. (2.40) in Ref. [4] which corresponds to the standard eigenvalue problem. The integers n_x and n_y were permitted to take the values between -10 and $+10$ (441 plane waves). This resulted in a very good convergence. We performed the computation for specific materials of Ni(Al) alloy cylinders in Al(Ni) alloy background. Numerical results for a filling fraction $f = 0.35$ are shown in Fig. 14. The figure is comprised of three parts. In the first part, we have plotted the band structure in the three principal symmetry directions, letting $\vec{k}$ scan only the periphery of the irreducible triangle of the first Brillouin zone. There appears a band-gap opened up between the first two bands. For this value of f, there is another very narrow band-gap lying between the fourth and the fifth bands,

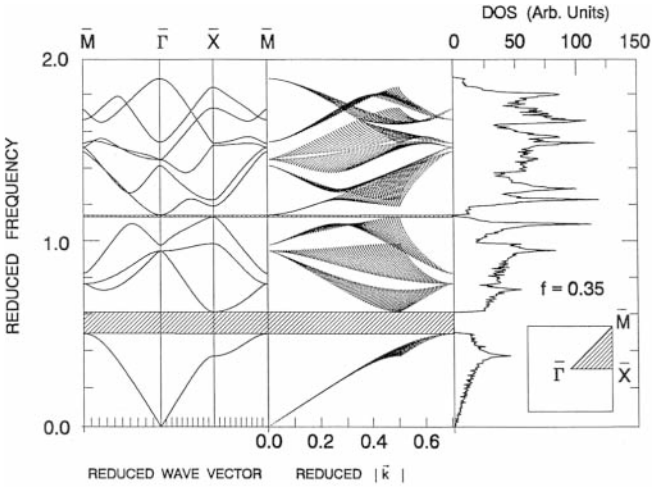

Fig. 14. Elastic band structure and density of states for Ni cylinders in an Al matrix – square lattice. The figure is comprised of three parts. In the first part, we plot the band structure in three principal symmetry directions letting $\vec{k}$ scan the periphery of the triangle $\bar{\Gamma}\bar{X}\bar{M}$. The middle part of this figure illustrates the eigenvalue Ω_k as a function of $|\vec{k}|$; i.e., the distance of a point in the irreducible part of the Brillouin zone from the $\bar{\Gamma}$ point. The third part depicts the DOS. The material parameters are $\varrho = 8.936(2.697)$ gm/cm^3, $C_{44}(= \varrho c_t^2) = 7.54(2.79) \times 10^{11}$ dyn/cm^2 for Ni(Al), and $f = 0.35$. Attention is drawn to the vibrational band-gap between the first two bands extending throughout the first Brillouin zone. (After Kushwaha *et al.*, Ref. [101]).

with $\Delta\Omega \simeq 0.02$. (There are no higher gaps, at least as far as 50th band.) The middle part of this figure illustrates an interesting way to present the band structure, namely, here we plot the eigenvalues Ω_n as a function of $|\vec{k}|$, i.e., the distance of a point in the irreducible triangle of the Brillouin zone from the origin. In doing so we have scanned not only the periphery but also the interior of the irreducible triangle $\bar{\Gamma}\bar{X}\bar{M}$ of the Brillouin zone (see the inset of Fig. 14). This part of the computation embodies 1326 values of the *uniformly* distributed grid of $\vec{k}$-points throughout the irreducible part of the Brillouin zone. Making use of the same number of $\vec{k}$-points, we have computed the density of states (DOS), plotted in the third part of the figure. The magnitudes of the elastic band-gaps coincide in all the three parts of the figure, which leads us to infer that the existing band-gaps extend throughout the Brillouin zone. This in turn establishes the fact that the wave propagation in the transverse plane is forbidden for the vibrations parallel to the cylinders. The value of the normalized lowest gap in this case is $\Delta\Omega \simeq 0.12$.

Next we examine the magnitude of the lowest band-gap as a function of the parameter contrasts (i.e., ΔC_{44} and $\Delta\varrho$). The geometry is the same as for Fig. 14, i.e., Ni alloy cylinders in Al alloy matrix. The numerical results, for $f = 0.35$, are depicted in Fig. 15. This three-dimensional plot contains a wealth of information about the existence of elastic band-gaps and the choice of materials to create such gaps. For instance, the arrow (on the right-hand side of this surface) indicates our explicit choice of the materials generating a gap given by $\Delta\Omega \simeq 0.12$ (see Fig. 14). In other words, the plot in Fig. 15 provides a guide to the feasibility of designing the phononic crystals that can possess the elastic band-gaps by an appropriate choice of the materials for a binary composite. In particu-

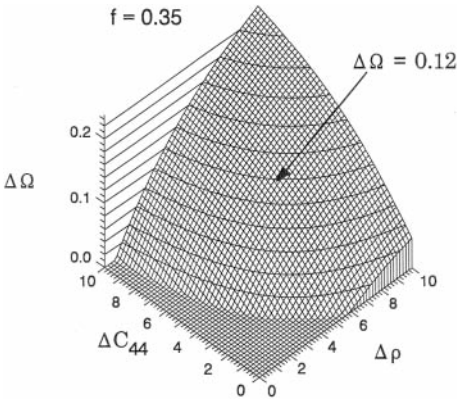

Fig. 15. Normalized magnitude of the lowest band-gap as a function of the contrasts in the elastic constant and in the density. We emphasize that this three-dimensional plot provides a guide to the feasibility of designing vibrational band-gaps by an appropriate choice of the materials for a binary composite in the square geometry. Here $f = 0.35$, just as in Fig. 14. The contrast parameters have the same units as defined in Fig. 14. (After Kushwaha *et al.*, Ref. [101]).

lar, let us remark that according to Fig. 11 the opening up of large band-gaps require that the contrast $\Delta\varrho$ and ΔC_{44} both be large. Here we have explored only the case where $\varrho_i > \varrho_b$ and $C_{44i} > C_{44b}$ – other possibilities are worth attempting, however.

Now we turn to the situation where Al alloy cylinders are embedded in a Ni alloy background. The numerical results are illustrated by the specific example $f = 0.75$ in Fig. 16. We find one elastic band-gap existing between the first two bands. The existence and magnitude of this gap is well established by the band structure (middle part of this figure) and by the density of states (the third part of the figure). It is thus concluded that this elastic band-gap extends throughout the Brillouin zone. The rest of the discussion related to Fig. 14 is still valid. It is worth mentioning that there are no other band-gaps opening up above the second band, or up to the 50th band, at least.

Finally, we scrutinize the width of the lower gap as a function of filling fraction for both cases. The numerical results are shown in Fig. 17. The curve marked case A (case B) represents the situation with Ni(Al) alloy cylin-

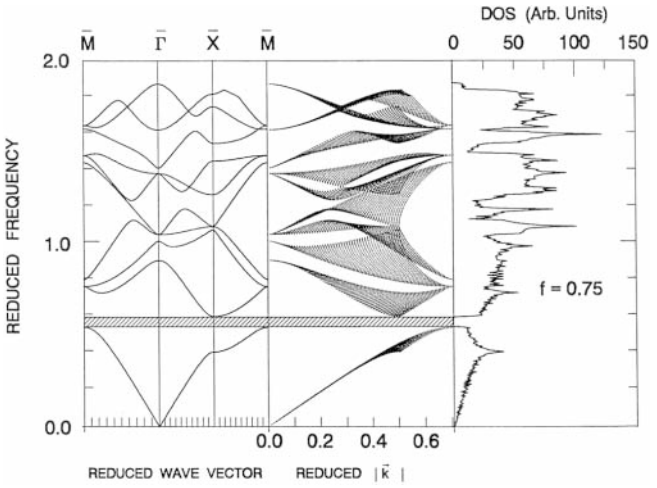

Fig. 16. The same as in Fig. 14, but for Al cylinders in Ni host matrix. The filling fraction is $f = 0.75$. (After Kushwaha *et al.*, Ref. [101]).

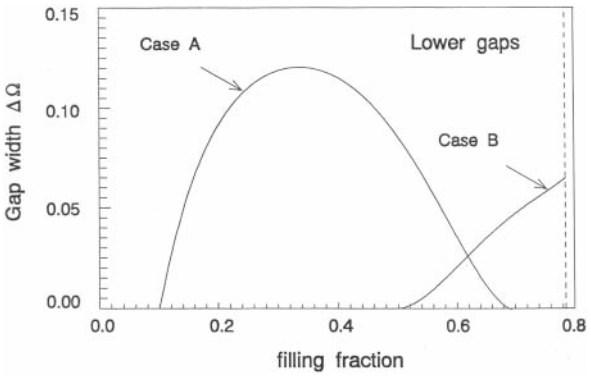

Fig. 17. The width of the lowest band-gap as a function of filling fraction. Case A (case B) refers to the Ni(Al) cylinders in Al(Ni) background. (After Kushwaha *et al.*, Ref. [101]).

ders in the Al(Ni) alloy matrix. It is found that the widest band-gap in case A corresponds to the filling fraction $f \simeq 0.33$. Similarly, the widest band-gap in case B opens up at a filling fraction corresponding to the close-packing ($f \simeq 0.7854$). It is noteworthy that, in case A, an *absolute* band-gap exists over a large range of filling fraction defined by $0.10 \leq f \leq 0.69$. In case B, on the other hand, there is no elastic band-gap for $f \leq 0.52$.

6.2.2 Hexagonal lattices

This section is devoted to discuss the possibility of achieving elastic band-gaps in the two-dimensional periodic elastic composites where the periodic array of parallel metallic rods of circular cross-section forms a hexagonal lattice in the perpendicular plane. The problem of *classical* band structure, both photonic and phononic, in the hexagonal pattern has received relatively less attention for the time being. This seems to be true in spite of the fact that the hexagonal pattern has exhibited wider band-gaps as compared to its square pattern counterpart, for the same value of the filling fraction [97, 102, 105, 113]. Since the array of cylinders forms a hexagonal lattice (of lattice constant a), the reciprocal lattice vector $\vec{G}$ is given by $\vec{G} = (2\pi/a)\,[n_x\hat{x} + (-n_x + 2n_y)\,\hat{y}/\sqrt{3}]$; we allowed the integers n_x and n_y to take the values in the range defined by $-10 \leq n_x, n_y \leq +10$. This implies 441 plane waves considered in the computation; with an estimated error of less than 1% and hence a very good convergence.

Figure 18 illustrates the band structure and the density of states (DOS) for Ni alloy cylinders in an Al alloy background. The plots are rendered in terms of dimensionless frequency $\Omega = (\omega a/2\pi)\,(\bar{\varrho}/\bar{C}_{44})^{1/2}$ versus the dimensionless Bloch vector $\vec{k} = a\vec{K}/2\pi$; just as in the plots in the preceding section. The figure is comprised of three parts. In the first part we plot the lowest ten bands in the three principal symmetry directions, letting $\vec{k}$ scan only the periphery of irreducible triangle of the first Brillouin zone (see inset of Fig. 18). We obtain a wide elastic band-gap opened up between the first two bands. Note that for this value of filling fraction ($f = 0.20$) there are no higher gaps, at least so far as 50th band. The second part of this figure shows a novel way to plot the band structure. Here we plot Ω_n as a function of $|\vec{k}|$. In this (middle) part of the figure we have scanned not only the periphery but also

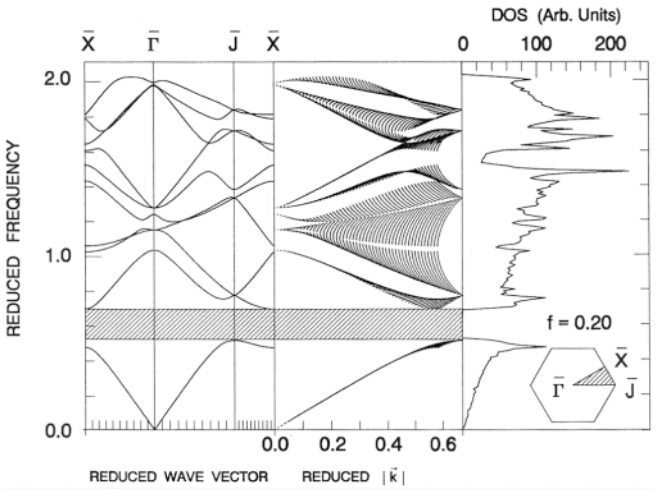

Fig. 18. The same as in Fig. 14, but for hexagonal lattice. The irreducible part of the first Brillouin zone (see the inset) is $\bar{\Gamma}\bar{J}\bar{X}$. The filling fraction is $f = 0.20$. We call attention to a wide band-gap existing between the first two bands and extending throughout the Brillouin zone. (After Kushwaha *et al.*, Ref. [102]).

the interior (for 1326 $\vec{k}$-points) of the irreducible triangle $\bar{\Gamma}\bar{J}\bar{X}$ of the Brillouin zone. In the third part of the figure we plot DOS, using the same number of $\vec{k}$-points as in the middle part of the figure. We draw attention to the magnitude of the gap which coincides in all the three parts of the figure. One can thus conclude that the existing gap extends throughout the Brillouin zone, and hence establishes the fact that within this gap, wave propagation in the transverse plane is forbidden for vibrations parallel to the cylinders. The value of the normalized gap-width in this case is $\Delta\Omega \simeq 0.18$.

Next we examine the situation when the filling fraction is increased. It is found that as f increases the magnitude of the lower gap attains a maximum (at $f = 0.29$) followed by a decrease for still higher values of f. Now, precisely at $f = 0.29$ another gap opens up between third and fourth bands. This upper gap also attains a maximum – at $f \simeq 0.48$. An example for the coexistence of the two gaps is illustrated by plotting the dependence of the gap-widths on the filling fraction in Fig. 19. The solid curves marked as upper gap and lower gap correspond to the present (hexagonal) case while the dashed curve refers to the lower gap for the square lattice (see the curve designated as case A in Fig. 17). The latter (dashed curve) is plotted here just for the sake of comparison. As one can see, for any value of f, the hexagonal pattern exhibits a wider elastic band-gap than the square pattern. Also, the range of f for the existence of the gaps is larger for the hexagonal case than for the square lattice. The specific range of the lower (upper) gap for the hexagonal lattice is defined by $0.04 \leq f \leq 0.73$ ($0.29 \leq f \leq 0.71$).

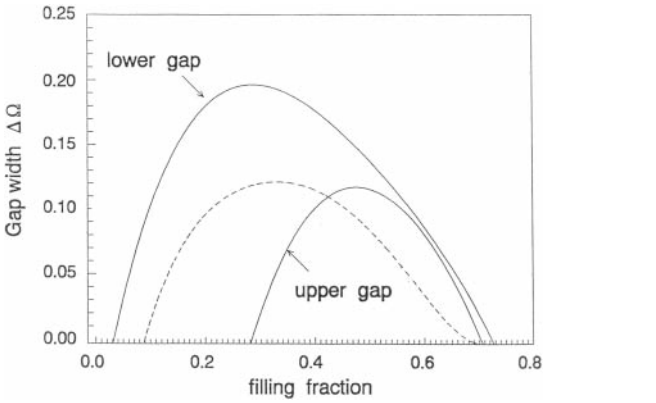

Fig. 19. Normalized widths of the lower and upper gaps (solid curves) as a function of filling fraction. The dashed curve refers to the lower gap in the square lattice for the same elastic composite (i.e., Ni cylinders in Al matrix). (After Kushwaha *et al.*, Ref. [102]).

From the definition of the normalized frequency Ω it is clear that all the gaps, both in the square and hexagonal lattices, are proportional to $(\bar{C}_{44}/\bar{\varrho})^{1/2}$ and are inversely proportional to the lattice constant a. For a given f the gap-width also depends on the contrast parameters $\Delta\varrho$ and ΔC_{44}.

We examine the magnitude of the lowest band-gap as a function of the elastic constant and density contrasts. The geometrical configuration is the same as before, i.e., infinitely long cylinders in a host material. The numerical results, for $f = 0.20$, are depicted by a three- dimensional plot in Fig. 20. This plot provides us with useful information about the existence of elastic band-gaps and the choice of materials to tailor such gaps. For instance, our specific choice of the Ni–Al composite gives rise to a gap given by $\Delta\Omega = 0.18$. This choice of alloys is represented by the dot next to the "1". Similarly, the numbers 2–5 correspond to other pairs of alloys (see the figure caption). In other words, the plot in Fig. 20 helps to engineer a desired elastic band-gap by an appropriate choice of the materials for a binary composite.

It should be pointed out that, unlike the square lattice, we find no gaps for the inverted geometry, namely, Al alloy cylinders in a Ni alloy background. We note that in this case we have a higher-velocity inclusions (the Al) surrounded by a lower-velocity materials (the Ni). It has already been commented that such a situation is less favorable for the creation of gaps than when a lower-velocity inclusions are surrounded by a higher-velocity material [115]. The larger range of filling fraction for opening up the wider (lowest) band-gap in the hexagonal lattice, than

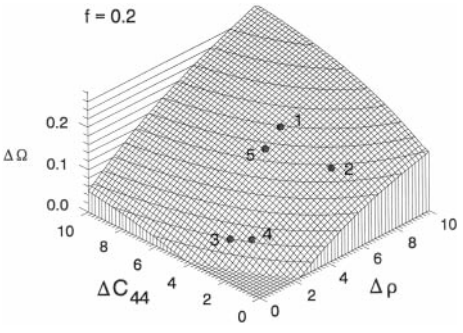

Fig. 20. Normalized magnitude of the lowest band-gap as a function of the contrasts in the density and in the elastic constant. The dots mark the gaps, assuming $f = 0.20$, for the following pairs of alloys: (a) Ni–Al, (2) Cu–Al, (3) Cu–Sn, (4) Pt–Au, and (5) Fe–Al. [The first (second) alloy of the pair corresponds to the cylinder (host).] The dot "1" describes the gap in Fig. 18. We stress that this three-dimensional plot provides a guide to the feasibility of engineering vibrational band-gaps by an appropriate choice of the materials for a binary composite in the hexagonal geometry. (After Kushwaha *et al.*, Ref. [102]).

that in the square lattice, is attributed to the fact that the constant energy surfaces of a hexagonal lattice are closer to the circular shape than those of a square lattice.

It is important to note that purely transverse (or, $\hat{z}$-polarized) modes propagating in the two-dimensional periodic systems are independent of the mixed (or plane-polarized) modes (see Sec. 2.4 in Ref. [4]), have legitimacy in their own right, and can be excited separately from the mixed modes [141]–[144]. As such, a composite of periodic, long cylinders is the simplest system that can give rise to the stop bands in which oscillations of a certain polarization are forbidden.

The existence of these *absolute* gaps in two-dimensional composites is expected to guarantee, with gradual disordering, the Anderson localization of transverse vibrations. The transition between the localized and the extended states in a two-dimensional disordered system is a question of considerable current interest [74]–[76]. It has been conjectured that there could exist the quasi-mobility edge(s) in two-dimensional disordered systems [85], which separate the strongly localized states from the weakly localized states (or power-law localized states). This has questioned the scaling theory of localization [157] which theorizes that no extended states should occur for any amount of disorder in one- and two-dimensional systems. Theoretically, such systems cannot be treated as regular systems with a small perturbation. Thus their characterization, particularly in respect of their transport properties, poses a substantial problem. The simpler systems as discussed in this section are believed to address the complex issue of quasi-mobility edge(s) in the classical (elastic) wave localization unambiguously – the root-cause of the expected unambiguity lies, of course, in the separability of the transverse and the mixed elastic waves.

7. Mixed and coupled vibrations

Before discussing the specific numerical examples on the band structure related problems that belong to the title of this section, we should make "crystal clear" the terms like longitudinal modes, transverse modes, mixed modes, and coupled (longitudinal-transverse) modes, which have often been used in this review. We need to do so at this stage in order to avoid any confusion associated particularly with the terms mixed modes and coupled modes. Note that defining these terms has much to do with the (periodic) dimensionality of the system concerned. Remember, we are concerned with these terminologies in the context of elastic and/or acoustic waves in liquids, gases, and solids – in the EM case the same terms are defined in a different frame.

As we mentioned earlier, the longitudinal waves are supported only in liquids and gases. One-dimensional periodic elastic composites, superlattices, for example, can, however, allow either pure longitudinal or pure transverse *elastic* waves, provided that the displacement vector $\vec{u}$ depends only on the spatial coordinate along the direction of the periodicity. In the case that the displacement vector $\vec{u}$ depends on the spatial coordinates in the sagittal plane (i.e., plane through $\vec{k}_{\parallel}$ and surface normal), one-dimensional systems can support either pure transverse elastic waves or the mixed modes, which are neither longitudinal nor transverse. In the two-dimensional periodic elastic composites (see Sec. 2.4 in Ref. [4]), we have seen that only pure transverse or mixed modes are allowed. The former are characterized by the displacement vector $\vec{u}$ along the cylinders ($\hat{z}$-axis) and perpendicular to the plane of propagation ($\hat{x}-\hat{y}$); while the latter are characterized by both $\vec{u}$ and $\vec{k}$ in the $\hat{x}-\hat{y}$ plane. In the literature the *complete* elastic band-gaps are assigned to the frequency window wherein overlapping of both pure transverse and mixed modes *together* prohibit the wave propagation in *all* possible directions. In the three-dimensional periodic elastic composites – solid inclusions in a solid background – no resolution of any polarization is possible and hence the propagating modes always remain coupled; *only* these modes will be referred to as coupled (longitudinal – transverse) modes.

This nomenclature of vibrational modes does not preclude the coupling of the longitudinal and transverse modes in the two-dimensional periodic elastic composites, however. But for the sake of clarity and because the purely transverse and mixed modes in these systems can be excited independently [141]–[144], we prefer to maintain the usage of the terms transverse and mixed modes. In fact, as one can see from Eq. (2.33) in Ref. [4], the mixed modes do involve both longitudinal and transverse speeds of sound. Sometimes, mixed modes have also been referred to as $x-y$ modes or plane-polarized modes. Thus it must be clear that this confusion of coupling between longitudinal and trasnverse modes does prevail in one- and, particularly, in two-dimensional periodic elastic systems.

7.1 Two-dimensional systems

This section is devoted to review the mixed (or plane-polarized) modes in the two-dimensional periodic elastic composites. We confine our attention to the geometry where the intersections of an array of parallel rods with a perpendicular plane form a square lattice. In this sense this is a supplement to the Sec. 6.2 where only transverse modes were considered. Two shapes of inclusions will be considered: circular cross-section, where the structure factor is specified by Eq. (46), and square cross-section of width $2l$, where the structure factor is given by [103]

$$F(\vec{G}) = f\,\frac{\sin(G_x l)}{(G_x l)}\,\frac{\sin(G_y l)}{(G_y l)} \tag{53}$$

with $f = 4l^2/a^2$ $(0 \le f \le 1)$. Integers n_x and n_y, in the reciprocal lattice vector $\vec{G}$, were allowed to take the values from -6 to $+6$ (169 plane waves). This resulted in a very good convergence confirmed by allowing n_x and n_y to assume the values from -10 to $+10$. Real material parameters were used to compute the band structure.

Figure 21 illustrates the bandstructure (left part) and density of states (right part) for both transverse and the mixed modes of a square array of C cylinders of *ciruclar* cross-section in an epoxy matrix, the filling fraction $f = 0.55$. The plots are given in terms of the dimensionless frequency $\Omega = \omega a/2\pi c_0$ (with $c_0 = (\bar{C}_{44}/\bar{\varrho})^{1/2}$) and

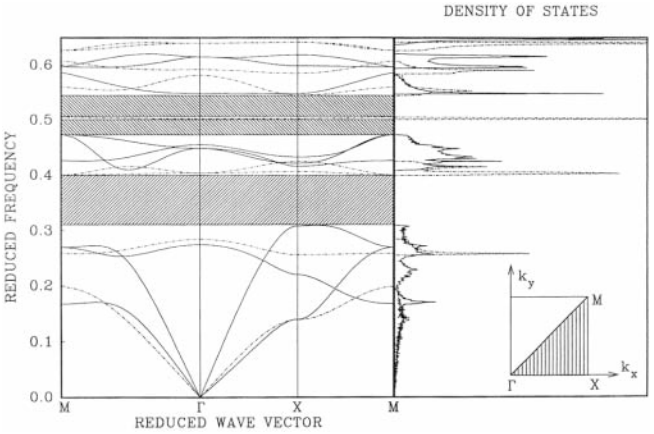

Fig. 21. The band structure (left panel) and DOS (right panel) for 2D square lattice made up of C cylinders of circular cross-section in an epoxy matrix. The filling fraction $f = 0.55$. Dash-dotted (solid) lines refer to the transverse (mixed) elastic waves. Attention is drawn to the three complete band-gaps shown by hatched regions (a fourth narrow but complete gap can be seen between ninth mixed mode and eighth transverse mode) and the (fifth) transverse mode occurring in the region separating the second and third lowest band-gaps. That the band-gaps are complete (and extend throughout the Brillouin zone) is evident from the gap regions coinciding exactly in the band structure and the DOS; the DOS was computed using equidistant mesh of 1275 $\vec{k}$-point covering boundaries as well as the interior of the irreducible triangle $\bar{\Gamma}\bar{X}\bar{M}$ of the first Brillouin zone. The material parameters are: $\varrho = 1.75(1.2)$ gm/cm^3, $C_{11} = 30.96(0.964) \times 10^{11}$ dyn/cm^2, $C_{44} = 8.846(0.161) \times 10^{11}$ dyn/cm^2 for C(epoxy). (After Vasseur *et al.*, Ref. [103]).

the dimensionless Bloch vector $\vec{k} = a\vec{K}/2\pi$, just as the previous plots in Sec. 6. For the calculation of the DOS, we incorporated 1275 $\vec{k}$-points covering the periphery as well as the interior of the irreducible triangle of the first Brillouin zone. As one can notice, within a few bands (nine for each polarization) plotted in this figure, the overlapping of the *absolute* gaps create three *complete* elastic band-gaps within which no propagation of sound or vibrations is possible. All of these band-gaps are specified by the minimum and maximum occurring at the high-symmetry points $\bar{\Gamma}, \bar{X}, \bar{M}$; except the bottom of the lowest band-gap, which lies at the top of the third mixed mode at a wave vector within the $\bar{X}$-$\bar{M}$ direction. An exact coincidence of the spectral-gap regions in the band structure and the DOS establishes the fact that these band-gaps extend throughout the first Brillouin zone. We draw attention to the *nearly flat* transverse mode propagating in the region between the second and the third lowest band-gaps. This corresponds to δ-function-like peak in the DOS.

Magnitudes of the three band-gaps versus filling fraction is depicted in Fig. 22. The solid, dash-dotted, and dashed lines refer, respectively, to the first, second and third lowest band-gaps. As one can see, there is a certain minimum of filling fraction f for all the three gaps to appear and similarly there is a certain maximum of f where these gaps cease to exist. The specific range of these band-gaps is specified by $0.2 \lesssim f \lesssim 0.65$, $0.43 \lesssim f \lesssim 0.65$, and $0.45 \lesssim f \lesssim 0.65$. Accidentally, the $f_{\max}$ at which each of the three band-gaps ceases to exist is *very nearly* the same (i.e., $f \sim 0.65$). It is interesting to note that the most usually available commercial C fiber reinforced epoxy composite conforms to a filling fraction $f = 0.6$ [158].

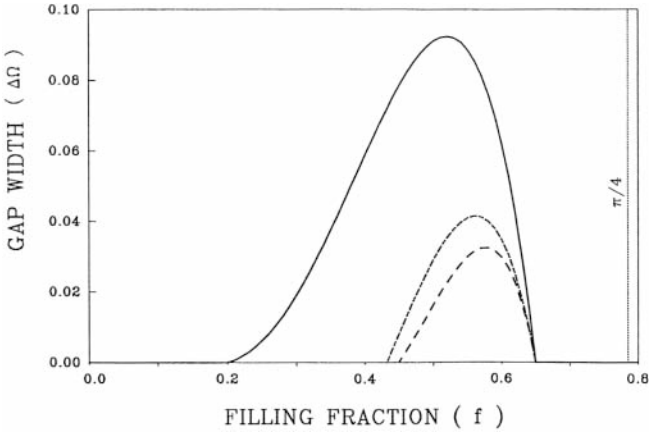

Fig. 22. Normalized gap-widths of the first three complete band-gaps versus filling fraction. Solid line, dash-dotted line, and dashed line refer to the first, second, and third lowest gaps, respectively. The dotted vertical line stands for the close-packing value ($\pi/4$) of the filling fraction. (After Vasseur *et al.*, Ref. [103]).

Next, we turn to the case where the C cylinders of *square* cross-section embedded in an epoxy matrix from a square lattice. The band structure for this composite, for $f = 0.65$, is illustrated in Fig. 23. Two *complete* elastic band-gaps shared by both polarizations appear in the range of frequency considered – only first nine bands for each polarization are plotted. The width of the lowest (and widest) band-gap in this case is $\Delta\Omega \simeq 0.14$ as compared to $\Delta\Omega \simeq 0.09$ in Fig. 20. The opening up of the upper

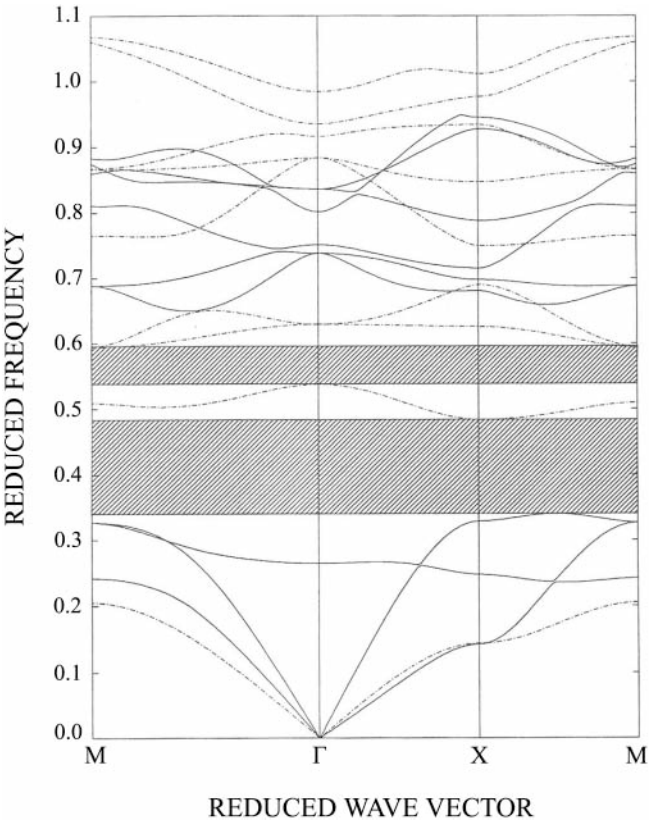

Fig. 23. The band structure for 2D square lattice made up of C cylinders of square cross-section in an epoxy matrix. The filling fraction $f = 0.65$. The dash-dotted (solid) lines refer to the transverse (mixed) elastic waves. The rest is the same as in Fig. 21. (After Vasseur *et al.*, Ref. [103]).

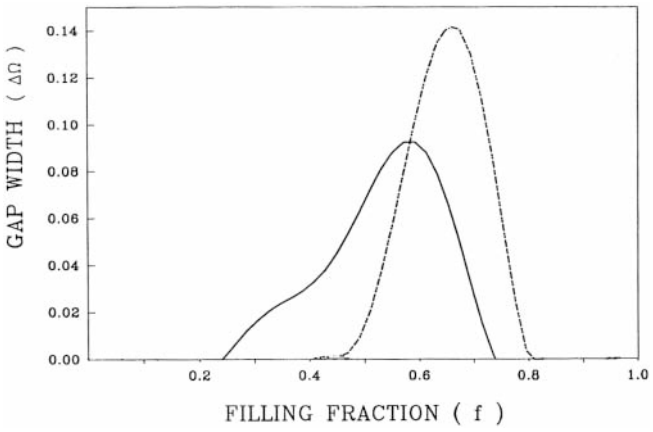

Fig. 24. Normalized gap-widths of the first two complete band-gaps versus filling fraction. Solid (dash-dotted) line refer to the first (second) lowest gaps. Note that the second lowest gap, which starts occurring at higher filling fraction, is larger than the first lowest gap. (After Vasseur *et al*., Ref. [103]).

band-gap in this geometry is analogous to the third lowest band-gap in the previous case (Fig. 21) in the sense that both the top and the bottom of these gaps are defined by the transverse modes at high symmetry points. This geometry is seen to provide large band-gaps for two independent polarizations (see, for example, the first and second bands for transverse modes depicted by dash-dotted curves and the third and fourth bands for mixed modes shown by solid curves) and this explains the large *complete* elastic band-gaps in this case.

The existence of the two band-gaps (Fig. 22) versus filling fraction is shown in Fig. 24. The first (second) lowest band-gap is represented by solid (dash-dotted) lines. The existence of the first (second) gap is specified by the $0.4 \lesssim f \lesssim 0.8$ ($0.25 \lesssim f \lesssim 0.74$). The maximum value of gap-width $\Delta\Omega \simeq 0.14$ (0.092) corresponding to $f \simeq 0.65$ (0.58) for the first (second) lowest gap. Comparing the results plotted in Figs. 26 and 28, respectively, for the inclusions of circular and square cross-sections, leads one to infer that the gap-widths are larger for the latter geometry. This is quite contrary to the idea of Sigalas and Economou [103] who stressed that inclusions of square cross-section (in two-dimensional systems) make the appearance of band-gaps more difficult.

We also investigated the case of inclusions with square cross-sections rotated through 45° with respect to the $\hat{x}$, $\hat{y}$ axes (see, for numerical examples, Ref. [103]). The specific materials were the C cylinders in an epoxy matrix, and the geometry was the square lattice. The band structure, for $f = 0.35$, depicted two *complete* gaps. The widest (the lowest) band-gap displayed $\Delta\Omega \simeq 0.033$. Within a first few bands these two *complete* gaps were specified by the range of filling fraction given by $0.225 \lesssim f \lesssim 0.43$ (the lower gap) and $0.3 \lesssim f \lesssim 0.45$ (the upper gap). There we also presented some interesting results on metallic systems [103]; W(Al) cylinders in Al(W) host, for example. A system of relatively more technological interest, namely, glass fiber reinforced epoxy matrix depicted, for $f = 0.6$, a wide *complete* elastic band-gap [104].

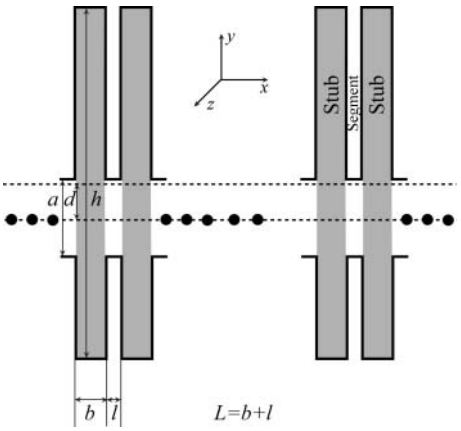

Fig. 25. Schematics of a quasi-one-dimensional periodic waveguide. The double stubs can be made of the same or diffferent material than that of the main waveguide. $L = b + l$ is the period of the system. (After Wang, Kushwaha, and Vasilopoulos, Ref. [131]).

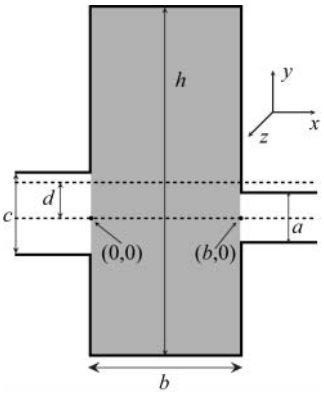

Fig. 26. Schematics of a general unit cell with asymmetric stubs. (After Wang, Kushwaha, and Vasilopoulos, Ref. [131]).

8. Periodically stubbed waveguides

This section is devoted to study the acoustic band structure and transmission spectrum in a periodically modulated quasi-one-dimensional waveguide, as depicted in Fig. 25. The system has a finite extension along the y direction and is periodically modulated, along the x direction by the addition of double, in general, asymmetric stubs, with different elastic properties than those of the main waveguide. The motivation stems from recent studies with interesting results pertinent to electronic and photonic waveguides modulated in the same fashion. Using the transfer-matrix technique, we demonstrate the tunability of the acoustic band gaps as a function of various parameters of the system, e.g., the length and/or width of the stubs. For the sake of generality, we start with a crossbar-like geometry of a single unit cell, as shown in Fig. 25. The origin of the Cartesian coordinates is at the uniaxial line intersecting perpendicularly the left arm of the stub of width b and length h. The center of the asymmetric stub lies at $(x = b/2, d)$. We denote the width of the left (right) waveguide segments by $c(a)$ and take the x axis parallel to the direction of propagation. We are interested in the solution of the wave equation for the out-of-plane vibrations, which, in a sense, correspond to the z-modes in a two-dimensional periodic system. It is noteworthy that this section heavily relies on Ref. [131].

8.1 Two-dimensional systems with one-dimensional periodicity

For the sake of clarity we discuss the numerical results in two parts. First, we consider the case when the waveguide and the stubs are made up of the same material. Clearly the band structure and/or transmission spectrum in this case reveals the influence of the various parameters involved in the problem. Then we take up the case when the materials in the waveguide and the stubs are different. Practically speaking, this case is more complex but richer than the previous one in the sense that one has more options to modulate the band structure and/or transmission spectrum. We have chosen carbon and epoxy resin as the suitable materials the acoustic system considered is made of. This is because these are the materials whose combination was first demonstrated to give rise to a complete band gaps, i.e., independent of the polarization of the wave and of the direction of propagation, in 2D periodic phononic crystals [103]. The parameters used are $\varrho = 1.75$ (1.2) g/cm^3 and $v_t = 711{,}095$ (115,830) cm/sec for carbon (epoxy).

8.1.1 Same material in waveguide and stubs

The left part of Fig. 27 shows the first nine bands for a symmetrically stubbed system made up of epoxy, with parameters $a_L = a/L = 0.5114$, $b_L = b/L = 0.4886$, $h_L = h/L = 1.125$, and $d_L = d/L = 0.0$. As one can see, all the nine bands are separated from each other by stop bands, or gaps, within which the acoustic wave propagation is forbidden. Unlike the other 2D and 3D periodic systems [4], there is a complete gap below a cutoff frequency $\Omega_c \simeq 1.6$ down to $\Omega = 0$. It is found that this (the lowest) gap persists independent of the values of the variable parameters. The existence of all nine gaps is well corroborated by the energy dependence of the transmission coefficient for $n_{\text{stub}} = 50$ on the right part of Fig. 27. The numerical results clearly reveal the zeros and ones in the transmission. It is noteworthy that the band structure

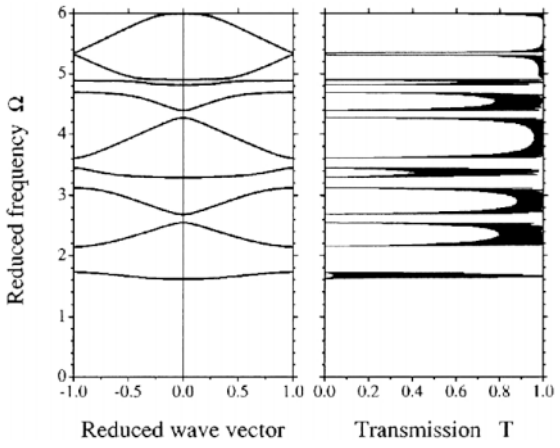

Fig. 27. Band structure (left panel) and transmission spectrum (right panel) for a system with the same material, epoxy, in the waveguide and the stubs. The reduced wave vector and frequency are defined by $k_x L/\pi$ and $\Omega = L\Omega/\pi v_1$, where v_1 is the transverse speed of sound in the waveguide. Notice the lowest acoustic gap below the cutoff frequency $\Omega_c \simeq 1.6$. For the plot of the transmission a system of fifty ($n = 50$) stubs was considered. (After Wang, Kushwaha, and Vasilopoulos, Ref. [131]).

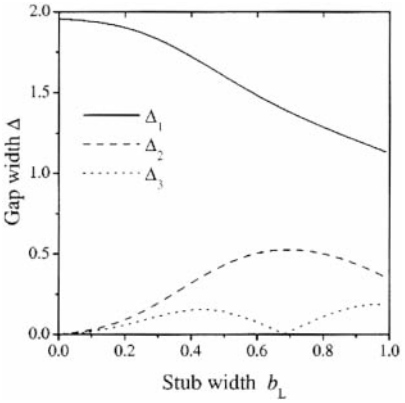

Fig. 28. The widths of the three lowest gaps as a function of the stub width $b_L = b/L$. The solid, dashed, and dotted curves refer to the lowest (Δ_1), second lowest (Δ_2), and third lowest (Δ_3) gaps. The material and the rest of the parameters are the same as those in Fig. 27. (After Wang, Kushwaha, and Vasilopoulos, Ref. [131]).

in this figure contains both direct and indirect gaps. For instance, the second, third, fifth, sixth, and ninth gaps are direct, while the rest are indirect. We consider it more appropriate to include the lowest (and also the widest) gap in the category of direct gaps. The most important aspect of these results is the cutoff frequency Ω_c below which no propagation at all is allowed. In this sense, the situation here is comparable to the semiconductor-dielectric *photonic* crystals investigated in [159, 160].

Figure 28 depicts the dimensionless gap widths of the three lowest gaps of Fig. 26 as a function of the dimensionless stub width b_L and the stubs are symmetric, i.e., $d = 0$. The width of the lowest gap Δ_1 decreases gradually, by approximately 45%, with increasing b_L but still remains finite for $b \to L$. The second lowest gap Δ_2 reaches a maximum for $b_L \simeq 0.7$ and decreases slightly before approaching the final minimum at $b \to L$. As can be seen, this gap increases enormously relative to its value for zero stub width. Similarly, the third lowest gap Δ_3 reaches one maximum at $b_L \simeq 0.44$, it then vanishes at $b_L \simeq 0.68$, and finally reaches a maximum at $b_L \to 1$.

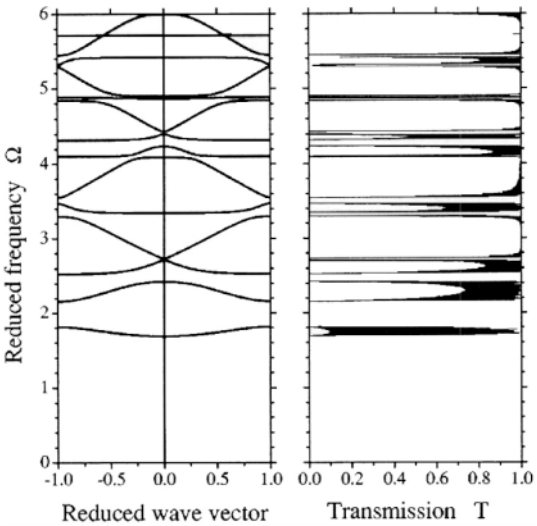

Fig. 29. Same as in 27, but for asymmetric stubs with asymmetry parameter $d_L = 0.25$. Notice the lowest acoustic gap below the cutoff frequency $\Omega_c \simeq 1.7$. (After Wang, Kushwaha, and Vasilopoulos, Ref. [131]).

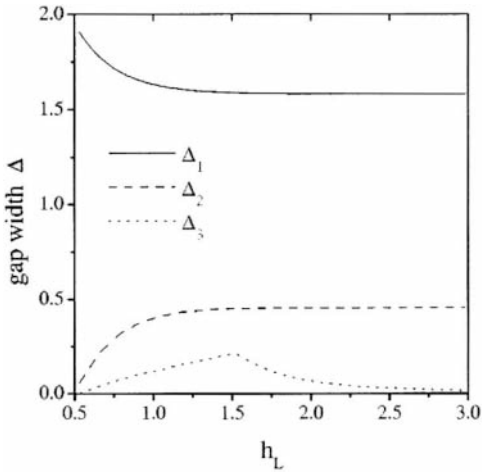

Fig. 30. The widths of the three lowest gaps as a function of the stub length $h_L = h/L$. The curves are marked as in Fig. 28. (After Wang, Kushwaha, and Vasilopoulos, Ref. [131]).

Note that all three gaps start opening up at a vanishingly small but finite value of b_L and that the lowest gap remains the widest one over the whole range of the stub width.

Figure 29 represents the band structure and the corresponding transmission spectrum for asymmetric stubs, with $d = 0.25$. The rest of the parameters are the same as in Fig. 26. We observe that the asymmetry has introduced two important effects. First, the number of bands accommodated within the same frequency range has increased, from nine to fourteen. Second, the band width of most of the bands has reduced. Overall, the effect of the asymmetry seems to result in gaps larger in number but shorter in width. This is true despite some exceptions, for instance, the case of the lowest gap, which now extends from $\Omega = 0$ to $\simeq 1.7$, instead of up to $\Omega \simeq 1.61$ in Fig. 27. All gaps in the band structure (left part of Fig. 29) are seen to be well substantiated by those in the transmission spectrum (right part of Fig. 29) for $n = 50$.

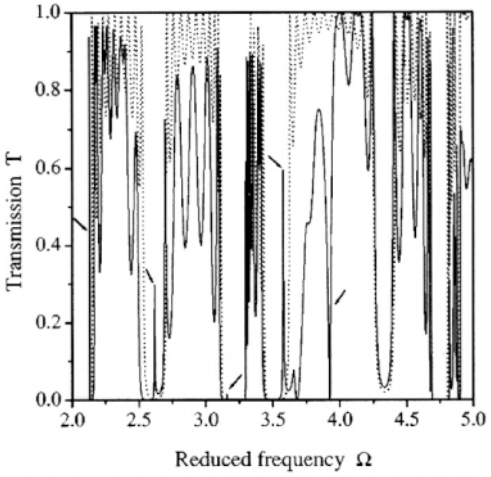

Fig. 31. Transmission spectrum for a system with eleven symmetric double stubs ($n = 11$). The central (sixth) symmetric stub is a defect with $h_L = 1.395$ and $b_L = 0.6305$. The rest of the parameters are the same as in the previous figures. Notice that the defect creates new modes or states in the gaps in an otherwise defect-free system. The peaks of these modes are marked with arrows. (After Wang, Kushwaha, and Vasilopoulos, Ref. [131]).

As a function of the asymmetry parameter d the three lowest gaps vary very little, by at most 10%, for $0 \leq d \leq 0.3$. Their dependence on b_L is similar to that shown in Fig. 4. As a function of the stub length h_L their behavior, shown in Fig. 29, is similar to that in Fig. 28 for Δ_1 and Δ_2 but somewhat different for Δ_3.

Figure 31 shows the transmission spectrum versus reduced frequency for a system made up of eleven symmetric stubs with the central (sixth) stub longer ($h_L = 1.395$) and wider ($b_L = 0.6305$) than the rest of the identical, in width and height, stubs. When unidentical to the other stubs, this central stub constitutes a defect. The solid (dotted) curves correspond to the presence (absence) of this defect. One can see that there are five complete gaps in the spectrum within the given frequency range. In addition, there is also a pseudogap, centered at $\Omega \simeq 4.35$, that corresponds to the low transmission or density of states. The defect introduces sharp transmission peaks, marked by arrows, within the first four gaps in plane analogy with the electronic and photonic case or with that of surface modes of a truncated superlattice. Another interesting consequence of introducing a defect in the system is the appearance of antiresonances, such as the one appearing in the fourth band at $\Omega \simeq 3.92$. We have noted similar effects in the case of an asymmetric ($d \neq 0$) defect introduced in the system.

8.1.2 Different materials in waveguide and stubs

We now present numerical results for a system in which the waveguide is made of epoxy and the stubs of carbon. Figure 31 shows the band structure and transmission spectrum for symmetric stubs; the parameters are $a_L = 0.9$, $b_L = 0.9$, $h_L = 1.5$, and $d_L = 0.0$. We note that there are only seven bands accommodated in the frequency range $0 \leq \Omega \leq 20$, and every pair of bands has a full gap in between. Moreover, the lowest acoustic gap extends from zero to the cutoff frequency $\Omega_c \simeq 2.3$. Some of the bands, such as the fourth and sixth, are seen to be almost flat and

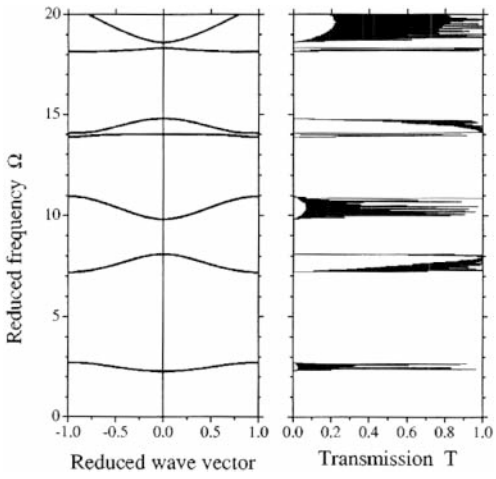

Fig. 32. Band structure (left panel) and transmission spectrum (right panel) for system with symmetric stubs with the waveguide segments (stubs) made of epoxy (carbon). The parameters used are $a_L = 0.9$, $b_L = 0.9$, and $h_L = 1.5$. Notice the lowest acoustic gap below the cutoff frequency $\Omega_c \simeq 2.3$ and extending down to $\Omega = 0.0$. (After Wang, Kushwaha, and Vasilopoulos, Ref. [131]).

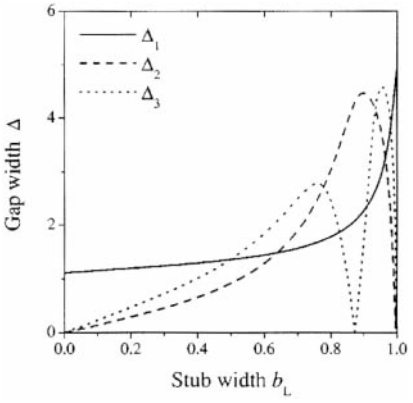

Fig. 33. The widths of the three lowest gaps versus the stub length b_L for the system studied in Fig. 31. The solid, dashed, and dotted lines refer, respectively, to the lowest (Δ_1), second lowest (Δ_2), and third lowest (Δ_3) gaps. Notice especially the strong variation of Δ_2 and Δ_3. (After Wang, Kushwaha, and Vasilopoulos, Ref. [131]).

hence have vanishingly small group velocity. All gaps in the band structure (left panel) correspond well to those in the transmission spectrum for $n = 50$ on the right panel. A prompt comparison of Figs. 27 and 32 reveals that one can achieve wider gaps in the band structure if the segments and stubs are made up of different materials.

Figure 33 shows the three lowest gaps as a function of the stub width b_L for the system specified in Fig. 32. There are several noteworthy points. First, the lowest gap is the widest one and the third gap is wider than the second one until $b_L \simeq 0.49$, where $\Delta_1 = \Delta_3$. At $b_L \simeq 0.64$, the width of the lowest and second lowest gaps are equal, i.e., $\Delta_1 = \Delta_2$. Also $\Delta_2 = \Delta_3$ at $b_L \simeq 0.78$ and 0.94. The second lowest gap is the widest one in the range specified by $0.78 \leq b_L \leq 0.94$. The third lowest gap vanishes at $b_L \simeq 0.87$ but reappears for $b_L > 0.87$ and becomes the widest in the range $0.94 \leq b_L \leq 0.98$. Also, $\Delta_1 = \Delta_3$ at $b_l \simeq 0.83$ and 0.91. Moreover, $\Delta_1 = \Delta_2$ at $b_L \simeq 0.96$ and $\Delta_1 = \Delta_3$ at $b_L \simeq 0.98$. Finally, Δ_1 reaches a maximum whereas both Δ_2 and Δ_3 vanish for $b \to L$.

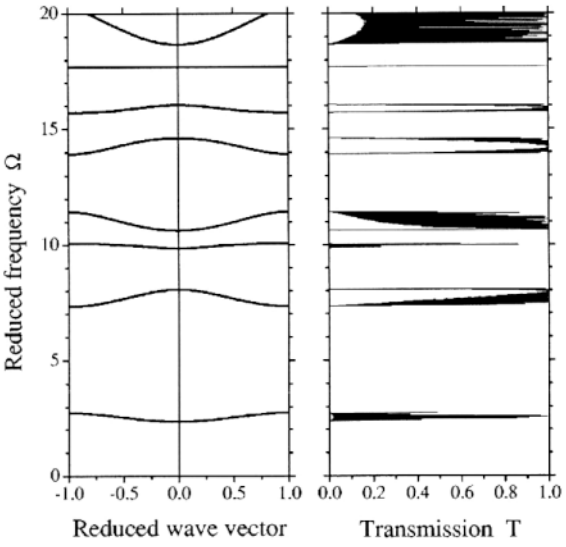

Fig. 34. Same as in Fig. 32, but for a system with asymmetric stubs ($d_L = 0.25$). The lowest acoustic gap occurs below the cutoff frequency $\Omega_c \simeq 2.4$ and down to $\Omega = 0.0$. (After Wang, Kushwaha, and Vasilopoulos, Ref. [131]).

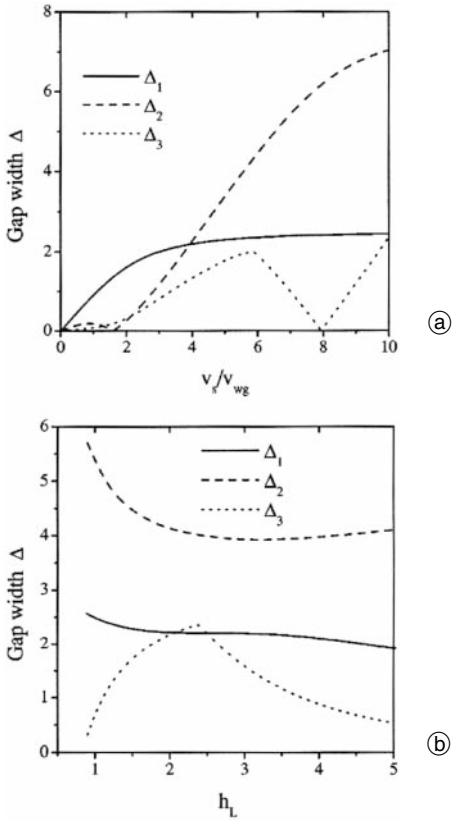

Fig. 35. (**a**) The widths of the three lowest gaps as a function of the velocities' ratio v_s/v_{wg}. (**b**) The three lowest gaps as a function of the stub width h_L. Notice the strong variation of Δ_2 and Δ_3, especially in (a). (After Wang, Kushwaha, and Vasilopoulos, Ref. [131]).

Figure 34 depicts the band structure and transmission spectrum considered in Fig. 31 but with asymmetric stubs. The asymmetry parameter is $d_L = 0.25$ and the other parameters the same as those used in Fig. 31. Now there are eight bands and eight gaps in the band structure. The lowest gap now extends from $\Omega = 0.0$ to $\Omega \simeq 2.4$. The asymmetry is seen to have brought about a number of interesting effects. A larger number of bands is accommodated in the same frequency range but the bandwidth is reduced. Again, the gaps in the band structure (left panel) correspond well to those in the transmission spectrum for a system with $n = 50$ stubs (right panel).

As a function of the stub width b_L the three lowest gaps behave qualitatively as those of Fig. 33. More important is their dependence, shown in Fig. 35(a), on the velocity contrast between two materials. As can be seen a wide modulation can be achieved in this asymmetric structure by just changing the ratio v_g/v_{wg}, more than two orders of magnitude for Δ_2. A less pronounced variation of the same gaps is shown in Fig. 35(b) as a function of the stub length h_L. As can be seen, Δ_1 remains almost insensitive to changes in h_L and Δ_2 changes by at most 30%; however, Δ_3 can change by a factor of 10 reaching a maximum at $h_L \sim 2.4$.

Figure 36 shows the transmission spectrum versus reduced frequency for a symmetric defect introduced in an otherwise periodic system with seven stubs ($n = 7$). The central (fourth) stub is defect in the sense that its length ($h_L = 3.0$) and width ($b_L = 0.4$) are different than those of the rest of the stubs. The other parameters are $a_L = 0.6$,

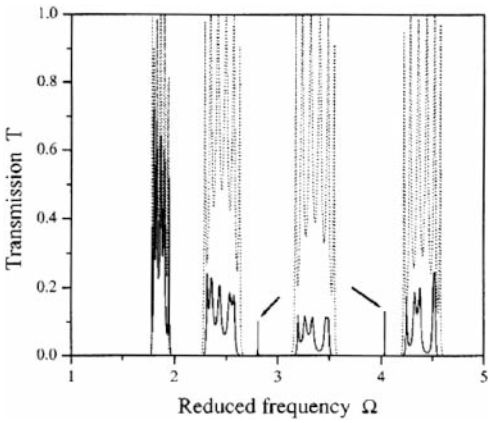

Fig. 36. Transmission spectrum for a system with seven symmetric ($d = 0$) double stubs ($n = 7$). The waveguide segments (stubs) are made of epoxy (carbon). The central (fourth) stub is a defect with $h_L = 3.0$ and $b_L = 0.4$. The other parameters are $a_L = 0.6$, $b_L = 0.2$, and $h_L = 1.4$. The solid (dotted) lines refer to the transmission with (without) the defect. The defect gives rise to modes in the gaps in an otherwise defect-free system. The peaks of these modes are marked with arrows. (After Wang, Kushwaha, and Vasilopoulos, Ref. [131]).

$b_L = 0.2$, $h_L = 1.4$, $d_L = 0.0$. The solid and dotted curves correspond, respectively, to the presence (absence) of the defect. There are five complete gaps in this frequency range in the spectrum before introducing the defect. Inserting this single defect in the system gives rise to one peak in the third gap and another in the fourth gap. These transmission peaks correspond to defect modes similar to those appearing in Fig. 31.

Finally, Fig. 37 illustrates the transmission spectrum versus reduced frequency Ω in a symmetric system made up of one (top panel), two (middle panel), and five (bottom panel) stubs. We remind that the waveguide segments (stubs) are made of epoxy (carbon) materials. The parameters are $a_L = b_L = h_L = 0.9$. That is, the waveguide has no stubs. The lowest panel shows the corresponding band structure. For $n = 1$ (top panel), the transmission coefficient becomes very small but it never approaches zero. In this sense we have only pseudogaps, not full gaps, in the system. As n increases the pseudogaps gradually turn into complete gaps (with transmission equal to zero) centered at almost the same midgap frequency. It has also been observed that the number of such complete gaps increases with increasing n.

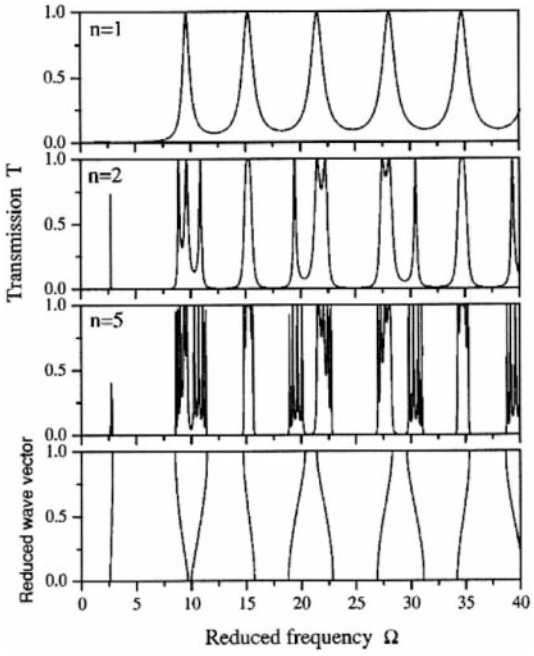

Fig. 37. Evolution of the transmission spectrum as a function of the number of stubs n for a system with waveguide segments (stubs) made of epoxy (carbon). The parameters are $a_L = b_L = h_L = 0.9$. Notice that as n increases the pseudogaps gradually turn into sharply defined complete gaps. The lowest panel shows the band structure. Notice that the first band is very narrow. (After Wang, Kushwaha, and Vasilopoulos, Ref. [131]).

9. The sculptures that can filter the noise

It is generally believed that sculptures or *objects d'art* at the public places are worthless from the scientific point of view. And yet a recent experiment has demonstrated that certain types of sculptures are (and can be) of considerable scientific relevance [139] and which can be related to the systems useful for studying, for example, the band-gap engineering in phononic crystals that can give rise to complete or pseudogaps in the band structure. In the case that these gaps turn out to be *complete*, such sculptures can behave as legitimate objects for noise control in their vicinity. The purpose of this section is to discuss this experiment [139] and subsequent theoretical work that have stirred considerable research interest in such *objects d'art*.

9.1. Two-dimensional systems

9.1.1 Experiment on Sempere's sculpture

The presentation of this section is motivated by the experimental measurement of sound attenuation on the sculpture, by Eusebio Sempere, exhibited at the Juan March Foundation in Madrid (Spain) [139] (see Fig. 38). It consists of a periodic distribution of hollow stainless steel cylinders, with a diameter of 2.9 cm and a unit cell of edge 10 cm. The cylinders are fixed on a circular platform (with 4 m in diameter) which can rotate on a vertical axis. The sound attenutation was measured in outdoor conditions for wave vectors perpendicular to the cylinder's vertical axis. The sculpture corresponds to a cermet topology with a volume

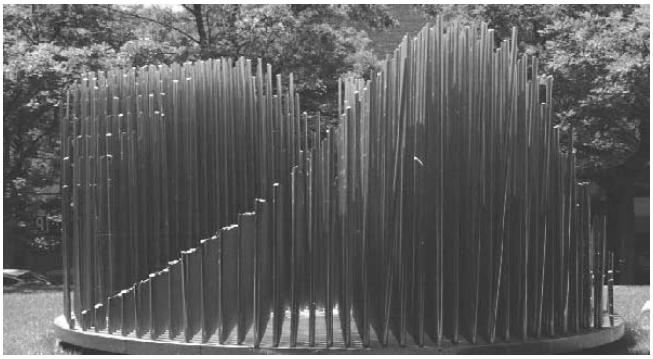

Fig. 38. Kinematic sculpture, by Eusebio Sempere, exhibited at the Juan March Foundation in Madrid. (Courtesy of F. Meseguer, CSIC, Spain).

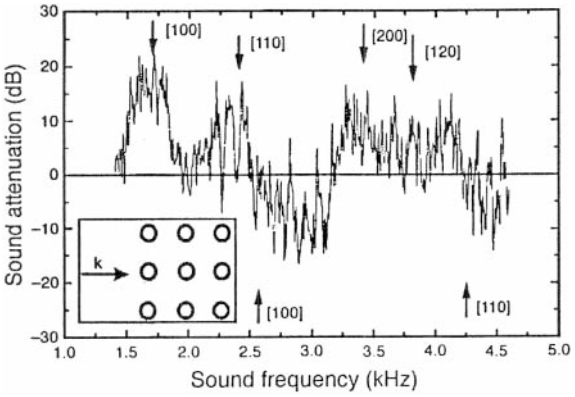

Fig. 39. Sound attenuation as a function of sound frequency. The wave vector is along the [100] direction as shown in the inset. Arrows indicate the calculated maxima and minima due to interference from the different crystal planes of the structure. (After Martinez-Sala *et al.*, Ref. [139]).

fraction occupied by the scatterers of 0.066 and sound-speed ratio of 17.9. The experimentalists' expectation, based on their observation, was that the sound attenuation peak at 1.67 kHz (see Fig. 39) could be ascribed to the formation of the first (lowest) gap in the band structure calculated for the geometry of this sculpture.

We call attention to the two important points: first, the sculpture represents a 2D periodicity in the $x-y$ plane (provided that the cylinders' vertical axis is presumed to be oriented along the z-axis); second, the sculpture consists of finite (in length) cylinders and is not strictly periodic (in the sense that it does not extend infinitely in the $x-y$ plane).

9.1.2 Ideal square lattices

This experimental finding was soon followed by a rigorous theoretical investigation embarking on the ideal situation and employing the actual experimental parameters – we refer to the true dimensions of the sculpture [108]. The complete band structure and density of states (DOS) were computed for an ideal 2D periodic system (in the square lattice) to draw the following conclusions. It was found that for the experimental situation (i.e., for the cylinders of 2.9 cm in diameter and system-period of 10 cm implying to the filling fraction $f = 0.066$) there is *no* acoustic gap for frequencies below 6.4 kHz. However, the DOS reveal prominent minima at 1.7 and 2.4 kHz. These frequencies do agree with those of the first two attenuation maxima in Ref. [139], and are indeed related to the diffraction from [100] and [110] planes (i.e., the $\overline{X}$ and $\overline{M}$ high symmetry points in the Brillouin zone). Thus, *even with idealization*, Sempere's sculpture was seen to exhibit only pseudogaps – *not full gaps*. This can clearly be seen from Fig. 40. It is noteworthy that similar conclusion was drawn through an independent investigation in Ref. [120].

Next we made an extensive investigation of band structure computation to explore under what circumstances such a geometry of sculpture can exhibit complete gaps. The results are illustrated in Fig. 41. The lowest (upper) gap is characterized by $0.31 \leq f \leq 0.7854$ $(0.40 \leq f \leq 0.61)$. This leads us to infer that there is no band gap for filling fraction $f \leq 0.30$. It is important to note that in the limit

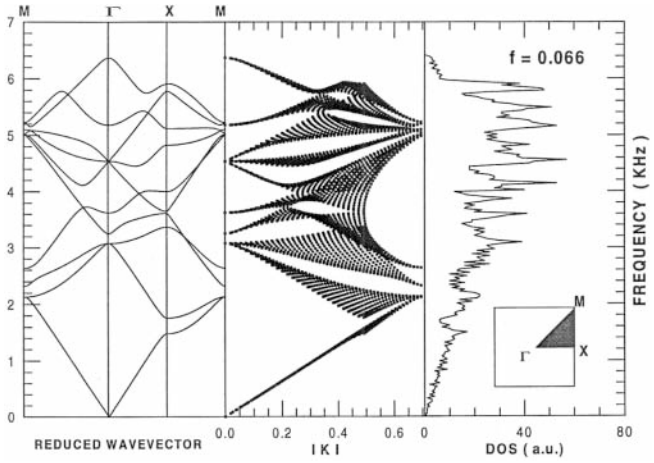

Fig. 40. Acoustic band structure and density of states for a square array of *rigid* stainless steel cylinders in air. The filling fraction is $f = 0.066$ and the period $a = 10$ cm. The tryptych is comprised of three parts. In the left panel, we plot the band structure in the three principal symmetry directions, letting the Bloch vector $\vec{k}$ scan only the periphery of the irreducible part (see the triangle ΓXM in the inset) of the first Brillouin zone. The middle panel demonstrates a novel way of plotting the eigenvalues as a function of $|\vec{k}|$; i.e., the distance of a point in the irreducible part of the Brillouin zone from the Γ point. The right panel illustrates the DOS. Note that there is absolutely no stop-band occurring within the first 10 bands. (After Kushwaha, Ref. [108]).

of close-packing six full gaps were found within the first ten passbands. An unexpected small amount of propagation (in the limit of close-packing) is attributed to the impossibility of achieving an *exact* physical condition for close-packing. What one would, in fact, expect in the limit of close-packing are the isolated vortices that would disallow any propagation at all.

An explicit and detailed example emerging from Fig. 40 is shown in Fig. 42. For a filling fraction of $f = 0.55$, the three parts of the triptych together clearly demonstrate that the two hatched regions stand for the two genuine, *complete* stop bands. The first stop band exists

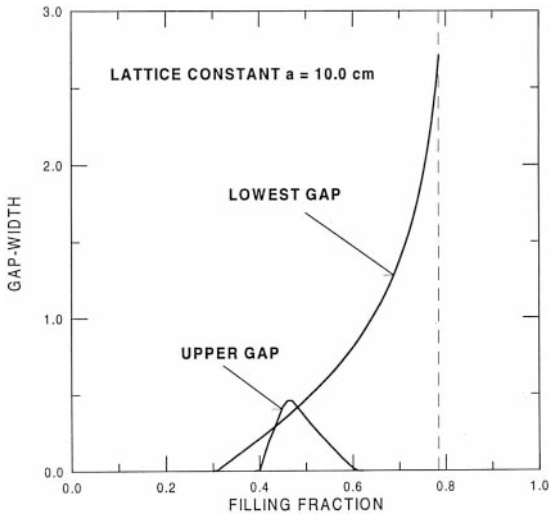

Fig. 41. Gap-widths (arbitrary units) of the only existing two stop-bands vs. filling fraction. The period of the system (the lattice constant) $a = 10$ cm. The vertical dashed line refers to the close-packing value ($f = 0.7854$). Evident is the fact that there is no acoustic stop-band for $f \leq 30\%$. (After Kushwaha, Ref. [108]).

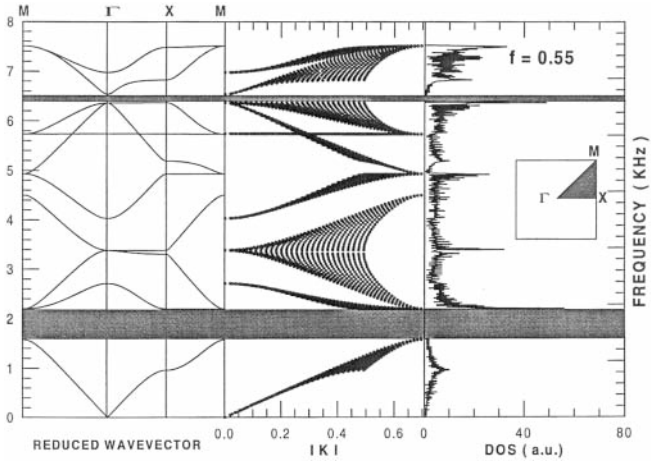

Fig. 42. The same as in Fig. 39, but for a filling fraction of $f = 0.55$. We call attention to the two complete stop-bands (shaded regions) extending throughout the Brillouin zone. (After Kushwaha, Ref. [108]).

between the first and second bands; and the second one between the eighth and ninth bands. Both of these stop bands are indirect in the language of solid state physics. We refer the reader for further details to Ref. [108].

Our experience on notoriously heavy computation on band structures enabled us to propose the fabrication of a tandem structure that could allow to achieve an ultra-wide-band filter for noise within the human audible range of frequencies [109]. The results of such an ultra-wide-band filter for the lowest band gap are summarized in Fig. 43. The curves ('wedges') labeled 1–5 are based on numerous band structure calculations – one for every value of the filling fraction f. These are, in fact, eigenvalue problems for the frequency $\omega/2\pi$ as a function of the Bloch vector k scanned in all directions. Consider the two dots on 'wedge' # 1, computed for $a = 2.0$ cm. Both dots are derived from a band structure computation for $f = 0.55$, hence radii $r = 0.84$ cm. This gives a stop band for sound between $\omega/2\pi = 7.85$ and 11.0 kHz. The dots mark these lower and upper edges of the stop band, and vertical distance between the dots is the width of the stop band. We see that a minimal filling fraction $f_{\min} \approx 0.3$ is needed for the obtention of a forbidden band (see Fig. 41), and that the stop band rapidly increases with f, until approaching the close-packing value $f_{\max} \approx 0.785$. The same procedure is repeated for four successively greater values of the lattice constant, until $a = 7.6$ cm corresponding to the 'wedge' # 5. We selected $f = 0.55$ for all sets of the tandem structure (see vertical dash-dotted line). Then, fixing the lattice constant of set 1 at $a_1 = 2.0$ cm, we choose a_2 (= 2.8 cm) in such a way that the upper branch of 'wedge' # 2 intersects the lower branch of 'wedge' 1 at $f = 0.55$. This procedure is continued until reaching the lower branch of 'wedge' # 5, resulting in five stop bands precisely joined so as to form a continuous 'super stop band'. In principle, our tandem structure should shield from noise in the entire range between 2.0 and 11.0 kHz. It is noteworthy that each one of the five sets also exhibits a second narrower stop band, lying higher in frequency (see Fig. 41). For the parameters of the figure the upper five stop bands are discontinuous and disconnected from the 'super stop band'.

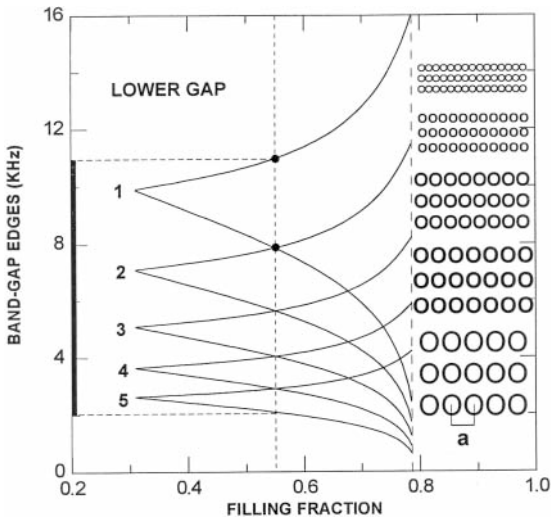

Fig. 43. Inset: cross-section of tandem structure of periodic, long arrays of circular metallic rods. Each of the five sets produces a stop band, whose upper and lower edges are plotted as a function of the filling fraction f ('wedges' 1–5). For $f = 0.55$ (vertical dashed line) the five stop bands join precisely so as to form a 'super stop band' ranging from 2.0 to 11.0 kHz; see vertical frequency bar (between two horizontally dashed lines). The required lattice constants are 2.0, 2.8, 3.9, 5.4, and 7.6 cm. The long-dashed vertical line stands for the close-packing value $f = 0.7854$. (After Kushwaha and Halevi, Ref. [109]).

For a given filling fraction, by increasing (decreasing) the separation a between neighboring cylinders one can lower (raise) the frequency range of the stop bands and hence that of the 'super stop band'. In fact, there is an inverse proportionality between ω and a and for $f = 0.55$, ω (kHz) $\approx C/a$ (cm); where $C = 21.94$ (15.72) for the upper (lower) edges of all the 'wedges'. An ultra-wide-band filter for environmental or industrial noise could thus be designed according to required specifications.

9.1.3 Ideal hexagonal lattices

The aforesaid experiment and subsequent theoretical work motivated us to explore the similar possibility of achieving complete sonic stop bands for honeycomb structure [110]. Extensive band structures computed for periodic arrays of rigid metallic rods in air (in the honeycomb structure) led us to achieve multiple complete acoustic stop bands within which sound and vibrations are forbidden. These gaps start opening up for a filling fraction $f \geq 8\%$ and tend to increase with the filling fraction, exhibiting a maximum at the close-packing. Figure 44 illustrates the gap-widths of all the *four* stop bands as a function of filling fraction, for a system of period $a = 10$ cm. Evident is the fact that there is no acoustic stop band for $f \leq 8\%$. Except for the third gap which opens in a very narrow range of filling fraction ($0.53 \leq f \leq 0.56$), the rest of the three gaps observe a maximum and a minimum before the close-packing (i.e., when the cylinders start touching each other implying the filling fraction $f = 0.9068$). It is interesting to note that at $f = 40\%$ there are no gaps opening up in the system, just as for $f \leq 8\%$. All the three gaps, which open over a wide range of filling fraction, observe a second maximum at the close-packing where the band structure reveals flat, degenerate passbands depicting huge stop

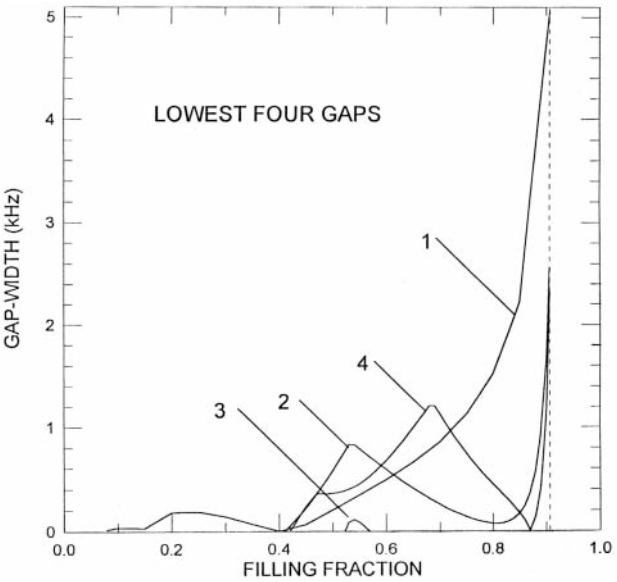

Fig. 44. Gap-widths of the existing four stop-bands vs. filling fraction for a 2D array of *rigid* metallic rods in air – honeycomb structure. The period of the system (i.e., the lattice constant) $a = 10$ cm. The vertical dotted line refers to the close-packing value ($f = 0.9068$). Evident is the fact that there is no acoustic stop-band for $f \leq 8\%$. The numbers 1 to 4 refer to the lowest, second lowest, third lowest and the uppermost (fourth) gaps in Fig. 2 of Ref. [110]. (After Kushwaha and Djafari-Rouhani, Ref. [110]).

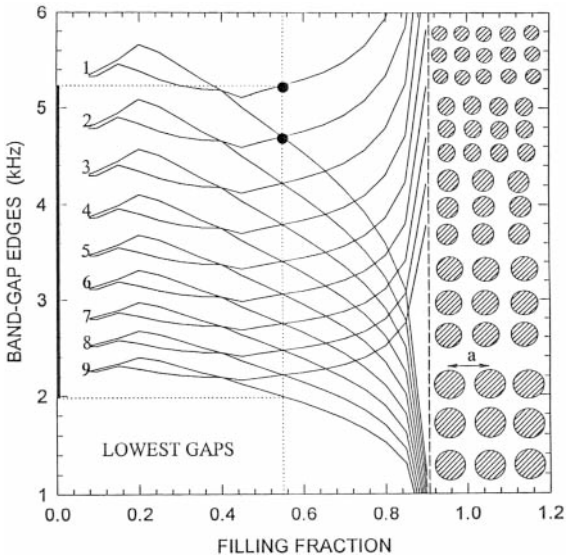

Fig. 45. Design of an ultra-wide-band filter corresponding to the lowest stop band in Fig. 44. Inset: schematic of the cross-section of tandem structure of (periodic) 2D arrays of *rigid* metallic rods in the honeycombe structure – what is shown is the front of a face of a unit cell of an individual periodic system. The "wedges" numbered 1–9 correspond, respectively, to the periods of 6.51, 7.24, 8.06, 8.98, 10.0, 11.13, 12.39, 13.80, and 15.37 cms. Each of the nine sets produces a stop band, whose upper and lower edges are plotted as a function of the filling fraction f. For $f = 0.55$ (vertical dotted line), the nine stop bands join precisely so as to form a "super stop band" within a frequency range between 1.99 kHz and 5.23 kHz (see the bold vertical frequency bar between the two horizontal dotted lines). The vertical dashed line refers to the close-packing value $f = 0.9068$. This is the most convenient way of demonstrating the existence of stop-bands in a given periodic system. (After Kushwaha and Djafari-Rouhani, Ref. [110]).

bands. This is quite easy to understand. In the limit of close-packing, the resultant 2D periodic system allows (almost) exactly isolated vortices and hence the sound cannot spin around the rigid cylinders.

Finally, the fabrication of a multiperiodic system in tandem designed so to give rise to wider stop bands in the desired frequency range is proposed. The band-gap edges of the *lowest* stop bands are computed as a function of the filling fraction for a large number systems with different periods (or lattice constants). The numerical results of such investigations are illustrated in Fig. 45. The scheme for designing an ultra-wide-band filter out of the tandem structure is the same as outlined above in the case of 2D square lattice (see Fig. 43). Consider the two dots on 'wedge' # 1 for a filling fraction $f = 55\%$. Now the ratio of the two frequencies (specified by the dots) is calculated and the next 'wedge' # 2 is created such that its upper edge (at the same f) crosses the lower edge of 'wedge' # 1. The same procedure is repeated for all the nine 'wedges' depicted in Fig. 45. In fact, we start with 'wedge' # 5 that corresponds to a period of $a = 10$ cm. The optimum situation is desirable, which refers to the lesser possible number of periodic composites and the smaller possible filling fraction. The former point concerns the cost and the latter hints to eventually avoiding construction of a wall of rigid cylinders. The filling fraction $f = 55\%$ is appealed to, where only *nine* 2D periodic composites in honeycomb structure are enough to guarantee a 'super stop band' from 1.99 to 5.23 kHz. Within the 'super stop band' the tandem structure stands still and total silence reigns. By this we mean that if one tries to transmit a wide-band wave through the tandem structure one will achieve a zero transmission within the range of the 'super stop band'. The completeness of such a 'super stop band' is promised due the overlapping of the individual stop bands in the neighboring composites. However, the frequency range of such a 'super stop band' is at the will of the designer – by increasing (decreasing) the period of the composites one can lower (raise) the frequency range of the stop bands and hence of the 'super stop band'.

Note that the second lowest stop band in Fig. 44 is the widest one in the range of filling fraction defined by $0.45 \leq f \leq 0.60$. The ultra-wide-band filter corresponding to the second lowest stop band was designed in Fig. 5 in [110]. For a filling fraction of $f = 55\%$, the tandem structure was to shown to give rise to a 'super stop band' that ranges from 3.48 to 11.00 kHz. It is interesting to note that the ultra-wide-band filter designed on the basis of the two lowest stop bands (in Fig. 44) simultaneously can cover the frequency range of the 'super stop band' lying between 1.99 and 11.0 kHz. This almost exactly was the range of the 'super stop band' covered by designing the ultra-wide-band filter on the basis of the lowest stop bands in 2D square lattice (see Fig. 43).

9.2 Three-dimensional systems

If viewed with exactitude both theory and experiment in 2D systems discussed above ignored the fact that the sound could filter along the axis of the cylinders. This then means that the term *complete* for the existing full stop bands there was reserved subject to this condition. A realistic model should have to remedy this shortcoming of

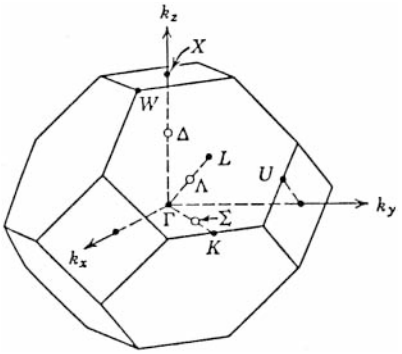

Fig. 46. The first Brillouin zone (a truncated octahedron) of the face-centered-cubic lattice showing the symmetry points and axes. (After Kushwaha *et al.*, Ref. [111]).

the present model. A better way of doing so is to investigate the realistic 3D systems instead. We embarked on the extensive band structures for cubic arrays of rigid spheres and cubes in air [111]. Complete stop bands were obtained for face-centered-cubic (*fcc*) structure; however, no gap was found for body-centered-cubic (*bcc*) and simple-cubic (*sc*) structures. These gaps (for *fcc* structure) start opening up for a filling fraction of $f \approx 54\%$ (27%) for spherical (cubic) inclusions and tend to increase with the filling fraction, exhibiting a maximum at the close-packing. We also proposed a tandem structure that allows the achievement of an ultra-wide-band filter for environmental or industrial noise in the desired frequency range. For the reasons of space, we will discuss only the results for the cubic inclusions. For the results on the spherical inclusions and the methodological details, we refer the reader to Ref. [111]. Figure 46 illustrates the first Brillouin zone for the *fcc* structure which is of immediate concern for the work discussed in this section.

Figure 47 depicts the band structure and the density of states (DOS) for rigid cubic inclusions in *fcc* structure; for a filling fraction of $f = 40\%$. The lowest ten bands are shown. The plots are rendered in terms of the eigenfrequency $\nu = \Omega(2\pi\bar{c}_l/a)$ [where a is the lattice constant and $\bar{c}_l = \sqrt{(\varrho^{-1}/C_{11}^{-1})}$] vs dimensionless Bloch vector $\vec{k} = \vec{K}a/2\pi$. The left part of the triptych represents the band structure in the five principal symmetry directions, letting $\vec{k}$ scan only the periphery of the irreducible part of the first Brillouin zone (see Fig. 46). The middle part is the result of an extensive scanning of $|\vec{k}|$ in the irreducible part of the Brillouin zone – the interior of this zone and its surface, as well as the principal directions shown in the left part of the figure. Each curve here corresponds to some direction of $\vec{k}$. The DOS in the right part of the triptych has been calculated on the basis of the scanning in the middle part, which corresponds to 1300 $\vec{k}$-points within the irreducible part of the first Brillouin zone. The three parts of the triptych in Fig. 46 together demonstrate that there is, indeed, a genuine, complete gap (the shaded region) existing between the first and second bands; and we consider such calculations as essential. It was noticed that there is *no other* band gap existing at least up to the 50th band. We did not find any gap for *bcc* and *sc* structures. Note that the existing band gap in *fcc* lattice is an indirect one in the language of solid state physics – with

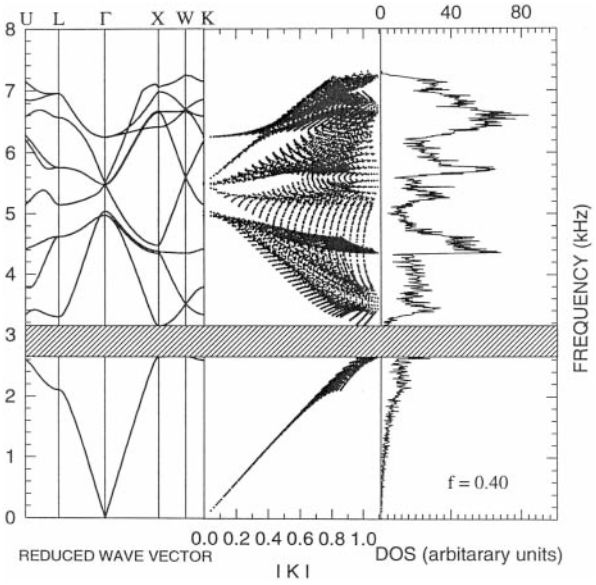

Fig. 47. Acoustic band structure and density of states for a *fcc* array of *rigid* cubic inclusions in air. The plots are rendered in terms of the frequency $\nu = \Omega(2\pi\bar{c}_l/a)$ [where a is the lattice constant and $\bar{c}_l\sqrt{(\varrho^{-1}/C_{11}^{-1})}$] vs. dimensionless Bloch vector $\vec{k} = \vec{K}a/2\pi$. The filling fraction is $f = 0.40$ and the period is $a = 10$ cm. The triptych is comprised of three parts: In the left panel, we plot the band structure in the five principal symmetry directions, letting the Bloch vector $\vec{k}$ scan only the periphery of the irreducible part of the first Brillouin zone. The middle panel demonstrates a novel way of plotting the eigenvalues as a function of $|\vec{k}|$; i.e., the distance of a point in the irreducible part of the Brillouin zone from the Γ point. The right panel illustrates the DOS. We call attention to the complete stop-band (hatched region) extending throughout the Brillouin zone. (After Kushwaha *et al.*, Ref. [111]).

the minimum (maximum) of the second (first) band lying at the high symmetry point X (W) in the Brillouin zone.

Next we plot the gap-width of the only existing stop band within the first ten bands in the *fcc* structure in Fig. 48. The size of a complete gap is usually expressed

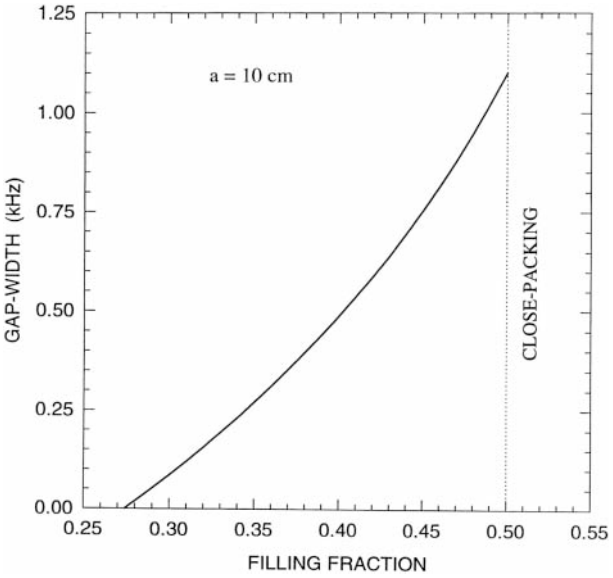

Fig. 48. Gap-widths of the only existing stop-band vs. filling fraction for a *fcc* array of *rigid* cubes in air. The period of the system is $a = 10$ cm. The vertical dotted line refers to the close-packing value ($f = 0.50$). Clearly, there is no stop-band for $f < 27.4\%$. (After Kushwaha *et al.*, Ref. [111]).

as the ratio of the gap-width and the midgap frequency. Here the *y*-axis represents just a difference in frequencies of the top and bottom of the stop band, for a given filling fraction. As can be seen from the figure, the filling fraction must exceed a certain minimum value, $f_{\min}$, for opening up a gap. The figure dictates the $f_{\min}$ to be 27.4% (as compared to $f_{\min} = 54\%$ for the spherical inclusions, see Fig. 3 in Ref. [111]). The magnitude of the gap is largest at the close-packing when the cubic inclusions fill exactly 50% of the space. The gap/midgap ratio in the limit of close-packing ($f = 50\%$) is found to be 0.4, i.e., almost double of that achieved from the lower gap in the case of spherical inclusions (see Fig. 3 in Ref. [111]).

Figure 49 demonstrates the design of the ultra-wide-band filter that could create a 'super stop band' within the frequency range between 1.35 and 6.18 kHz, for a filling fraction $f = 40\%$ through a tandem structure made up of nine 3D periodic composites in *fcc*. The essential difference, as compared to the spherical inclusions, is that the band gaps are larger and these are opened at relatively smaller filling fractions. From the technological point of view, this has an obvious advantage of designing ultra-wide-band filters for noise control with relatively lesser number of 3D composites with larger periods; and this is because of the lower filling fraction serving the purpose.

Figure 49 (as well as Figs. 43 and 45 in 2D systems) addresses a typical question concerned with the strategy of unwanted noise abatement: is it feasible to devise low-tech means that could forbid the sound propagation in the human audible range of frequencies (20 Hz−20 kHz)? This is a very important question that has become a major concern of scientists, engineers, and architects involved in the design of the buildings and in the planning of the cities, working together to find technically feasible solutions to the problem of noise. Fundamental to bring about a solution is the better understanding of sound propagation through the city streets and in the atmosphere above the city. For such an understanding the availability of band structures is essential. Our theoretical concern is thus simply meant to emphasize the fundamental issues involved in the sister subject of band-gap engineering of periodic elastic composite systems.

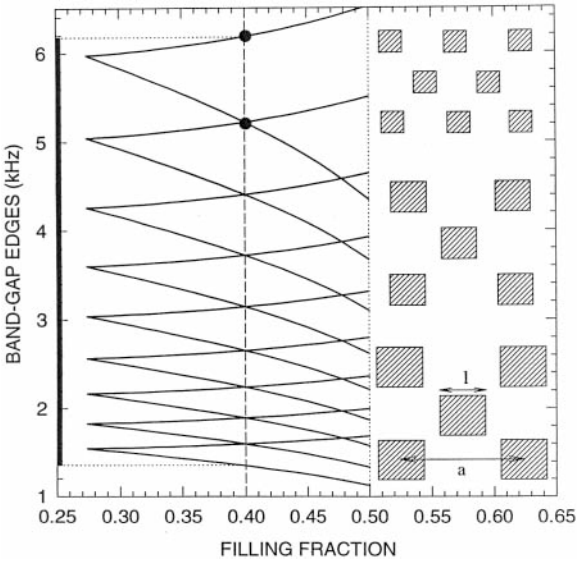

Fig. 49. Inset: cross-section of tandem structure of (periodic) cubic arrays of *rigid* cubes in *fcc* arrangement − what is shown is the front of a face of a unit cell of an individual periodic system. The "wedges" numbered 1–9 correspond, respectively, to the period of 5.08, 6.02, 7.13, 8.44, 10.00, 11.84, 14.02, 16.60, and 19.66 cms. Each of the nine sets produces a stop band, whose upper and lower edges are plotted as a function of the filling fraction f. For $f = 0.40$ (vertical solid line), the nine stop bands join precisely so as to form a "super stop band" within a frequency range between 1.35 kHz and 6.18 kHz (see the bold vertical frequency bar between the two horrizontal dotted lines). The vertical dotted line refers to the close-packing value $f = 0.50$. (After Kushwaha *et al.*, Ref. [111]).

10. Single scattering: a prediction tool for the band structure

10.1 Introduction

The largest part of the existing research on periodic elastic systems concerns systems of spherical scatterers [101–103, 107, 117–119]. Some of the basic conclusions of this research are that [117–119] the appearance of a gap is favored for (i) spheres concentration 10%–50%, (ii) non-connected spheres (cermet topology), (iii) heavy spheres in light host (i.e. small ϱ_o/ϱ_i) for solids *while* light spheres in heavy host (i.e. large ϱ_o/ϱ_i) for fluids, (iv) large velocities contrast between scatterers and host, with the velocities of the host to be larger than those of the scatterers, when the density is everywhere constant, *while* in the presence of density contrast small velocity contrast favors the gap. Indeed there were found surprisingly large gaps in solid systems of heavy spheres in polymer host [119], where the velocities contrast between scatterers and host is almost absent. Moreover it was found a not strong dependence of the gap on the lattice structure and on the scatterers filling ratio.

The attempts to understand the above results and to find an easy way to predict or to explain them led us to the study of the single scattering [38, 39, 161], i.e. scattering from only one sphere. Single scattering has the advantage that comprises a simple physical system both in its study and in its explanation. Moreover the relative independence of the band structure characteristics on the lattice structure and the scatterers filling ratio that has been observed is a strong indication for its possible dominant role in the formation of the band structure characteristics.

The single scattering study is done here through calculations and analysis of the single scattering cross-section [162–164]. The attempt is to examine the possible relation of the cross-section resonances with the band structure characteristics and thus to transform the conditions for the gap to conditions on the cross-section, something which can facilitate a lot their explanation.

In what follows we discuss the cross-section calculation method, the typical cross-section characteristics in acoustic or elastic systems, the cross-section dependence on the various system parameters that affect the existence of the gap in a periodic system, as well as the form of the cross-section associated with the cases of wider gap. The connection of the band structure characteristics with the cross-section form led to the understanding of the mechan-

ism of the gap formation and to the interpretation of the optimum for the gap conditions, something that it is presented in the last section of this part.

10.2 Cross-section calculation

The calculation of the single scattering cross-section is done by considering a plane wave, either longitudinal or transverse, impinging upon the surface of a sphere, and by calculating the scattered wave through the application of proper conditions at the sphere surface [162]. The incident plane wave, $\mathbf{u}^{\mathrm{inc}}$, is expanded in a sum of spherical waves [37] and thus the scattered wave $\mathbf{u}^{\mathrm{sc}}$ and, through it, the scattering cross-section, σ, are also obtained as sums of the contribution of each partial spherical wave: $\mathbf{u}^{\mathrm{sc}} = \sum_n \mathbf{u}_n^{\mathrm{sc}}$ and $\sigma = \sum_n \sigma_n$.

The scattering cross-sections is defined as [38, 39, 161]

$$\sigma = \frac{\int \langle J_r^{\mathrm{sc}} \rangle \, r^2 \, \mathrm{d}\Omega}{\langle J_z^{\mathrm{inc}} \rangle} \quad \text{for} \quad r \to \infty \,, \tag{54}$$

where

$$\langle J_i \rangle = \langle \mathrm{Re}\,(\sigma_{ij}) \, \mathrm{Re}\,(\dot{u}_j) \rangle = -\tfrac{1}{2}\omega \, \mathrm{Im}\,(\sigma_{ij}^* u_j) \,. \tag{55}$$

u_j are the components of the displacement vector, $\mathbf{u}$, σ_{ij} are the stress tensor components [41], the symbol $\dot{u}_j$ denotes time derivative, the symbols $\langle\ \rangle$ and * denote time average and complex conjugate, respectively, and the superscripts *sc* and *inc* denote, respectively, scattered and incident wave. The last part of Eq. (55) is obtained taking into account time dependence of the form $\mathrm{e}^{-i\omega t}$.

For large distances, r, from the center of a sphere embedded in a host (with host velocities c_{lo} and c_{to}, for longitudinal and transverse waves respectively), the scattered wave can be written as

$$\mathbf{u}^{\mathrm{sc}}(\mathbf{r}) = \mathbf{f}_{ml}(\theta, \varphi) \, \frac{\mathrm{e}^{ik_{lo}r}}{r} + \mathbf{f}_{mt}(\theta, \varphi) \, \frac{\mathrm{e}^{ik_{to}r}}{r} \quad \text{for} \quad r \to \infty \,, \tag{56}$$

where the angular distribution of the scattered wave is given by the scattering amplitudes $\mathbf{f}_{ml}$, $\mathbf{f}_{mt}$ ($m = l, t$ depending on whether the incident wave is longitudinal or transverse); $k_{lo} = \omega/c_{lo}$, $k_{to} = \omega/c_{to}$.

The total scattering cross-section is related with the scattering amplitudes through the well-known *optical theorem*, a result of the conservation of energy. For a longitudinal incident plane wave, propagated along the z-direction ($\theta = 0$), the optical theorem gives [39, 165]

$$\sigma = \sigma_l = \frac{4\pi}{k_{lo}} \, \mathrm{Im}\,[\hat{\mathbf{z}} \cdot \mathbf{f}_{ll}]_{\theta=0} \,, \tag{57}$$

where θ is the polar angle and $\hat{\mathbf{z}}$ the unit vector along z-direction. For a transverse incident wave, polarized along x-axis,

$$\sigma = \sigma_t = \frac{4\pi}{k_{to}} \, \mathrm{Im}\,[\hat{\mathbf{x}} \cdot \mathbf{f}_{tt}]_{\theta=0} \,. \tag{58}$$

The calculation of the cross-section is done using equations (57) and (58) combined with the expansions of $\mathbf{f}_{ll}$ and $\mathbf{f}_{tt}$ in spherical waves. For the details of calculation and for an alternative way of calculation without the use of optical theorem see Refs. [38, 39].

10.3 Typical cross-section characteristics

A typical single scattering cross-section for a system of relatively rigid ($c_l/c_t \approx \sqrt{2}$) solids is shown in Fig. 50. Fig. 50(a) shows the cross-section for longitudinal incident wave, while Fig. 50(b) shows that for transverse incident wave. As can be seen from Fig. 50, the cross-sections exhibit sharp resonances, occurring when the incident wave frequency coincides with one of the approximate eigenmodes of the system. Each of the resonances is contribution of a distinct partial spherical wave, reflecting the symmetry of the corresponding eigenmode (see the numbers above the resonances in Fig. 50). Note that in the transverse incident wave case there is no spherically symmetric ($n = 0$) resonance as the $n = 0$ wave is purely longitudinal. With the exception of the $n = 0$ mode the other resonant modes are either mixed longitudinal and transverse (being excited with both longitudinal and transverse incident waves) or only transverse (being excited with transverse incident wave, when the host material is solid). The last, purely transverse modes are usually very sharp, something that implies high energy concentration inside the sphere and small leakage to the host.

Studying the cross-sections for a variety of material combinations [38, 39, 119, 161], we found that when the host material is solid the first resonance comes from the $n = 1$ spherical wave, while when the host material is fluid the first resonance comes from the $n = 0$, spherically symmetric wave. This is the case of Fig. 51, where a typical cross section for a sphere embedded in a fluid is shown. It should be noted that when both sphere and host are fluids the successive $(\nu, \nu + 1)$ resonances are equidistant, with distance $[d/\lambda_{li}]_{\nu+1} - [d/\lambda_{li}]_{\nu} = 1$ (d is the sphere diameter and λ_{li} the wavelength inside the sphere).

A cross-section feature which can be used as an explanation tool is worth-noticing [38, 163]: When the sphere parameters approach those of a void sphere (ϱ, λ, μ, c_l, $c_t \to 0$) or of a "hard" sphere (ϱ, λ, $\mu \to \infty$, $c_l, c_t \to 0$), each of the scattering amplitudes can be written as a sum of two terms (see Fig. 51(b)); one ($f^{(0)}$ – plotted with

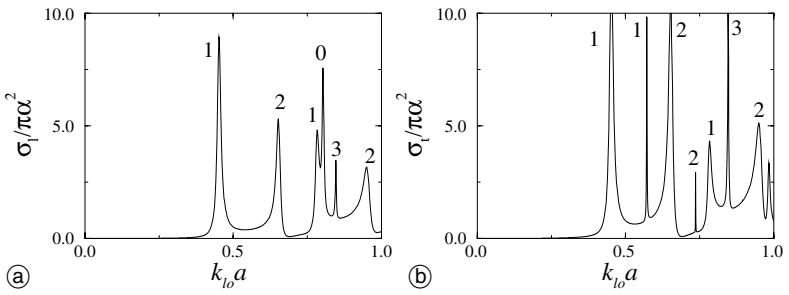

Fig. 50. Total scattering cross-section for longitudinal (**a**) and for transverse (**b**) incident wave; $c_l/c_t = \sqrt{2}$ for both sphere and host, $\varrho_o/\varrho_i = 1$ and $c_{lo}/c_{li} = 5.48$. a is the sphere radius and $k_{lo} = \omega/c_{lo}$ the longitudinal wave vector in the host. The number above each resonance denotes the spherical wave where it comes from.

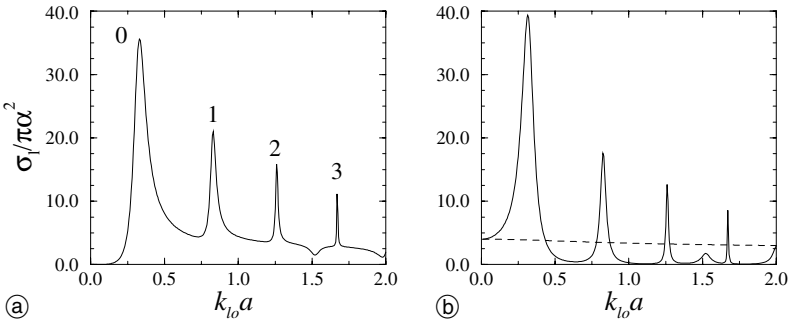

Fig. 51. (**a**) Single scattering cross-section for a fluid sphere in a fluid host with $c_{lo}/c_{li} = 3$, $\varrho_o/\varrho_i = 3$ and $c_{to} = c_{ti} = 0$. (**b**) Single scattering cross-section for an empty sphere embedded in the host of (a) (dashed line) and cross-section arising from the subtraction of the empty sphere scattering amplitude from the fluid sphere amplitude (solid line) a: sphere radius, $k_{lo} = \omega/c_{lo}$: wave vector in the host. The number above each resonance denotes the corresponding spherical wave.

dashed line in Fig. 51(b)) is the scattering amplitude of the void or the hard sphere, and corresponds to contribution to the cross-section of the scatterer shape. The other term ($f - f^{(0)}$ – solid line in Fig. 51(b)) has the form of a series of resonances, well separated from regions of almost zero scattering; these resonances are a characteristic of the material of the sphere. At the frequency regions where the first term dominates there is no significant inflow of the wave into the sphere. On the contrary, at the resonances of the second term a strong penetration of the wave inside the sphere occurs.

10.4 Cross-section dependence on the material parameters

10.4.1 Dependence on the velocities ratio c_{lo}/c_{li}

As was mentioned earlier, the gap in a periodic system of solids, under the absence of low or no density contrast between scatterers and host, is favored from high c_{lo}/c_{li} ratio, where $c_{lo}(c_{li})$ is the longitudinal wave velocity in the host (sphere). The same is not true if strong density contrast exists. There it favors low c_{lo}/c_{li} ratio. Examining now the single scattering cross-section, for $c_{lo}/c_{li} > 1$ the increase of this ratio has as a result (i) the formation of stronger and sharper resonances, (ii) the approaching of these resonances and (iii) the reduction of the background scattering, i.e. the scattering at the regions between the resonances. For $c_{lo}/c_{li} < 1$ the cross-section is smooth, its values are relatively low and it is not strongly dependent on the c_{lo}/c_{li} ratio. This difference between the $c_{lo}/c_{li} < 1$ and the $c_{lo}/c_{li} > 1$ case is not surprising, at least to people coming from the electronic waves community, if one takes into account the corresponding electronic problem as scatterers of low wave velocities correspond to deep potential wells in Schrödinger's equation, i.e. to also strong resonances. Comparing the band structures and cross-section results it is easy to understand why large c_{lo}/c_{li} favors the gap formation if no density contrast exist. It is because it is associated with stronger scattering. Why the case is not the same in the presence of density contrast it is something not easy to understand using what was discussed until now and in will discussed in the next Section.

10.4.2 Dependence on the densities ratio ϱ_o/ϱ_i

As has also been mentioned earlier, in periodic systems of fluids the increase of the ratio ϱ_o/ϱ_i has as a result a widening of the gap (if exists), i.e. the gap is favored from low scatterer (or high host) densities, i.e. high ϱ_o/ϱ_i; this is in contrast to what happens in solids, where gap is favored from high scatterer (or low host) density. The reason for this unexpected difference between fluids and solids was puzzling people of the acoustic/elastic community for quite a long time. Here we will show that the single scattering can give the key for the understanding of this difference.

What happens in the single scattering cross section? For a fluid scatterer in a fluid host the increase of the ratio ϱ_o/ϱ_i has as a result a large enhancement of the cross-section. The most considerable enhancement occurs at the first ($n = 0$) resonance and at the region between the resonances (background scattering region). On the other hand, in solids, the increase of ϱ_o/ϱ_i entails a reduction of both the height and the width of the single scattering peaks. Comparing single scattering and band structure it is easy to understand why for the gap opening there is the difference between fluids and solids mentioned above, as gap opening is connected with strong single scattering.

It remains to understand why there is the observed difference between fluids and solids concerning the dependence on the density ratio ϱ_o/ϱ_i, also in the single scattering results. This difference can be understood if one takes into account that in the case of fluids both the first resonance and the background scattering are due to the $n = 0$ spherically symmetric wave, which contributes insignificantly in the rigid solids case (there, due to the high c_t the transverse wave dominates the scattering). This $n = 0$ scattering, which corresponds to spherically symmetric oscillations of the sphere, is favored from low sphere densities, as a sphere of a lower density can experience stronger oscillations (if located in a fluid, which does not strongly resist to these oscillations), and thus stronger scattering than a sphere of a denser material.

10.4.3 Dependence on the rigidity of the materials, c_{to}/c_{lo} and c_{ti}/c_{li}

Concerning the cross-section dependence on the rigidity, c_t/c_l, of the sphere and host it is worth-noticing that the cross-section is much more sensitive to the rigidity of the host material than to that of the sphere. A solid sphere in a solid (fluid) gives similar results with those of a fluid sphere embedded in the same solid (fluid). The same "insensitivity" to the rigidity of the scatterers is observed also for the periodic system band gaps.

10.5 Relating the positions of the narrow bands and gaps, with those of the single scattering resonances

In all cases of periodic materials which were initially studied and which exhibited a gap, this gap was found to lie

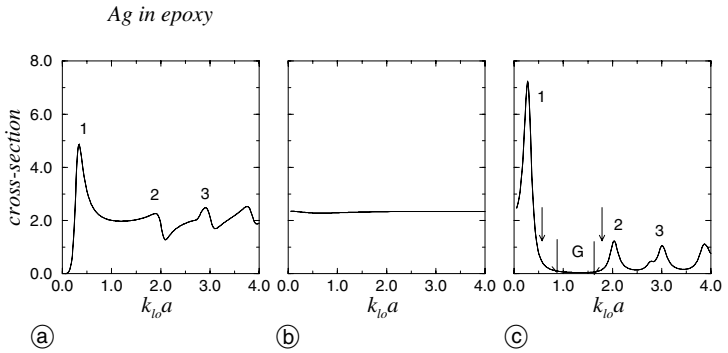

Fig. 52. (**a**) Cross-section for scattering of an incident longitudinal wave by a Ag sphere embedded in epoxy. (**b**) Cross-section for scattering from a rigid sphere in epoxy. (**c**) Cross-section arising by the subtraction of the rigid sphere scattering amplitude from the Ag sphere amplitude. a: sphere radius, $k_{lo} = \omega/c_{lo}$ the wavenumber in the host; the number next or above each resonance denotes its corresponding spherical wave. The arrows in (c) show the flat bands position in the band structure of the *fcc* periodic system which exhibits the maximum gap, while the double arrow surrounding the letter G shows the boundaries of this maximum gap.

between the first and the second resonance of the corresponding single scattering cross-section, with the gap width to be always smaller than the distance between these two resonances. Moreover, in all cases, the narrow bands of the band structure were found to lie very close to single scattering resonances, while this proximity with the resonances is as much large as narrower the band is.

Extensive study of the position of the gap and the flat bands as a function of the scatterers concentration showed that the first appearance of the gap (at low concentration of the scatterers) occurs very close to the first resonance of the corresponding single scattering cross-section. As the concentration of the scatterers is increased the gap is moved towards the middle between first and second resonance, a position at which it remains until its closing (for high scatterers concentration), while flat bands appear very close to the resonances. How this can be understood? At low concentrations the appearance of the gap very close to a resonance can be attributed to the fact that at these concentrations the propagation occurs mostly through the host materials and the resonances (strong scattering regimes) inhibit this propagation. As the scatterers concentration is increased the resonance states of the neighboring scatterers overlap, giving rise to a new propagation channel, i.e. hopping from scatterer to scatterer using these overlapping states. This propagation channel is preferable at intermediate and high scatterer concentrations as, there, propagation through the host is not easy any more. Thus the gap moves towards the middle of two successive resonances, while at the resonance positions flat bands of the periodic system appear[1]. This picture is alike the linear combination of atomic orbitals (LCAO) picture, which results to the formation bands and gaps in electronic periodic systems.

10.6 Interpretation of the optimal conditions for gap formation

As was mentioned in the introduction of this section, a noticeable result of the band structure study is that while the gap formation seems to be favored from large ratio c_{lo}/c_{li} for no density contrast between scatterers and host, under the presence of density contrast the largest gaps were found in systems where the velocities of the host were only slightly larger than those of the scatterers, and not in systems with high c_{lo}/c_{li}. Realistic cases of those systems concern spheres of a heavy metal, like, e.g., Pb, Ag, steel, in a low density host, like polymers (epoxy, PMMA etc.). The typical form of the cross-section in these "wide gap cases" is the one of Fig. 52 (concerning an Ag sphere in epoxy): The cross section is composed of strong (high and wide) resonances, well separated from each other, and with high background scattering between them. This background scattering comes almost exclusively from the contribution of the hard sphere (see subsection 10.3), as is shown in Fig. 52(c), where this background scattering has been subtracted and the resonances appear clearly. The gap here appears between the first two resonances while flat bands appear very close to them.

A careful and systematic study of many cross-section cases and of the corresponding band structure results showed that whenever in the cross-section appear *strong* and *well separated resonances* with *high background* scattering between them, the corresponding periodic system exhibits a wide gap, located between the first two resonances. This significant result can be understood if one accepts for the periodic systems the existence of the two limiting channels of propagation that we discussed in the previous section: through the host and through the spheres, hopping from one sphere to its neighboring ones through their overlapping resonance states (in most cases both channels operate). In the strong background scattering regime between the resonances neither channel is available (the host is not available due to strong background scattering and the spheres are not available due to the absence of resonances). Thus the opening of a gap is the only possibility. Moreover, the large resonances separation (result of the small velocities contrast between host and spheres) permits opening of a wide gap. Taking into account the above, it can be easily understood why under the presence of density contrast between scatterers and host (which insures strong resonances) the low velocity contrast favors the gap formation. It is because it gives strong background scattering and it keeps the resonances well separated, permitting thus a wide gap.

Studying the single scattering cross-section and examining the relation of the cross-section resonances with the band structure characteristics (gap and flat bands) of the corresponding periodic system we managed to speculate on the conditions that favor the appearance of a gap in this periodic system and to understand partly the mechanism of the gap formation. It was found that whenever in the single-scattering cross-section there are strong and well separated resonances with a strong background scattering between them, due to the hard or empty sphere, a wide gap may

[1] Hybridization or level repulsion are the reasons for which the coincidence between flat bands and resonances is not exact.

appear in the corresponding periodic system, in the frequency regime between the resonances. This can be understood by considering two limiting channels of propagation in a periodic system: Through the host, and through the scatterers, using the overlapping resonance states of the individual scatterers. Whenever both channels are blocked an opening of a gap is mostly expected to take place. Nevertheless, it has been recently shown that not only the individual scatterers but also their structural arrangement can be very important in the formation of absolute phononic gaps [132].

11. A phononic resonator

Quantum mechanics tells us that in the transmission of an electron through a double barrier, a resonance may occur. When the double barrier is symmetric the transmission coefficient at resonance equals unity, when the double barrier is not symmetric the transmission coefficient is less than unity. There is a phononic analogue of the above.

Consider a phononic *fcc* crystal of lead spheres (centered on the sites of the lattice) in epoxy and we view the crystal as a sequence of (001) *fcc* planes. The crystal has an appreciable absolute frequency band gap with a ratio of gap width to midgap frequency equal to 0.33 [166].

A sequence of five successive *fcc* planes of the crystal constitutes a phononic slab that sustains the frequency band gap mentioned above. By replacing a plane of spheres with a plane of the same 2D periodicity but with smaller spheres, we can introduced an impurity plane into our system which leads to a resonance in the transmittance of the slab as shown in Fig. 53, which shows the transmittance of a shear elastic wave incident normally on the slab. A similar effect occurs for a compressional wave.

The transmission resonance at a frequency within the gap signifies the existence of a state of the elastic field centered on the impurity plane: a mode of vibration of the elastic field that extends to infinity parallel to the surface of the slab (in the manner of a Bloch wave), but decays rapidly normal to the impurity plane on either side of it. We note that the transmission coefficient equals unity at the resonance frequency when the impurity plane is removed from the center of the slab by one plane, the value of the transmission coefficient at resonance diminishes by at least two orders of magnitude (middle diagram in Fig. 53), and the resonance disappears altogether when the impurity plane is removed to the surface of the slab. This is indeed a general characteristic of resonant tunneling [167].

We can always go a step further and think of interacting impurity planes by forming a heterostructure of repeating slices such as the slab above. This will give rise to bands of impurity states inside the absolute frequency gap of the crystal. This suggests that a random distribution of impurity planes (to be taken as size disorder) will lead to vibrational modes localized over smaller regions of the material. The reader may find more on this matter in Refs. [61, 166].

12. Dissipation in phononic lattices

12.1 A brief review on the physics of phononic gaps

It has been established that periodic binary composites consisting of nonoverlapping high-density scatterers in a low-density host material [119] as well as three-component phononic crystals consisting of coated spheres inside an embedding medium [34, 168], exhibit absolute phononic gaps. It is also true that the crystal structure can be very important in the formation of absolute phononic gaps [132]. Nevertheless, the physical origin of the widest of these gaps lies beyond the Bragg gaps at the Brillouin-zone boundaries. In reality, there are also bands originating from resonant elastic modes of the individual scatterers: resonant states on neighbor scatterers that couple weakly with each other, resulting in corresponding relatively narrow bands. These bands originating from the "rigid-body" resonance modes of the individual scatterers hybridize with the continuum bands corresponding to an almost free propagation in an effective homogeneous medium [19, 132, 169, 170]. The opening of the hybridization gap is favored by an increased volume filling fraction, but at the same time it is compromised by the widening of the resonance bands which is also favored by an increased value of the same property of the crystal. As we will show later, this compromising effect will be seised by introducing dissipation on the scatterers of the crystal [169].

For reasons of completeness, we also add the effect of coated scatterers, by which we may shift a hybridization gap toward a desired frequency region [34, 168].

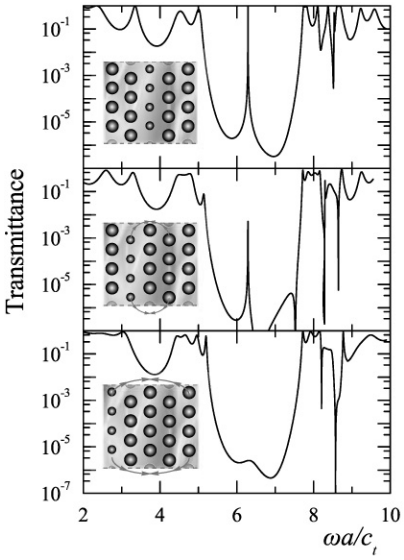

Fig. 53. Transmittance of shear elastic waves incident normally on a slab of an *fcc* crystal of lead spheres in epoxy. The slab consists of five planes of spheres parallel to the (001) surface. The spheres have a radius $S = 0.25a$, except those of the middle plane (top diagram), or of the second plane from the surface (middle diagram), or of the surface of the slab (bottom diagram), which have $S_i = 0.7S$. a is the *fcc* lattice constant, ω is the angular frequency and c_t is the shear speed of sound in epoxy. (After Psarobas *et al.*, Ref. [166]).

12.2 An absorbing sphere in an inviscid fluid

The viscoelastic response of the system, we are going to present here, is accounted for by means of the Kelvin-Voigt model [171], which is well-suited for materials and ultrasonic frequencies of major interest. The problem of acoustic-wave scattering by a single viscoelastic sphere of radius S has been adequately addressed in the past [171] according to the Kelvin-Voigt viscoelastic model. In such

a case the sphere is considered to be elastic with modified shear and compressional complex wavenumbers, the imaginary parts of which represent a measure of the loss. In particular, for an absorbing sphere in an inviscid fluid background, the complex compressional and shear wavenumbers are conveniently defined as

$$q_{sl} = \frac{c_l}{c_{sl}} \frac{q_l}{\sqrt{1 - i[(\alpha + \beta)/\varrho_s c_{sl}^2]}}\,,$$
$$q_{st} = \frac{c_l}{c_{st}} \frac{q_l}{\sqrt{1 - i(\beta/\varrho_s c_{st}^2)}}\,, \tag{59}$$

where $q_l = \omega/c_l$ refers to the fluid environment with ω being the angular frequency and c_l the respective speed of sound. The real parts of the complex Lamé parameters of the sphere, $\lambda_s = \lambda_{se} - i\lambda_{sv}$ and $\mu_s = \mu_{se} - i\mu_{sv}$, combined with the density ϱ_s yield the compressional and shear wave speeds respectively

$$c_{sl} = \sqrt{(\lambda_{se} + 2\mu_{se})/\varrho_s}\,, \qquad c_{st} = \sqrt{\mu_{se}/\varrho_s}\,. \tag{60}$$

The imaginary parts of the Lamé parameters are connected to the viscous losses $\alpha + 2\beta$, and β of the sphere as follows: $\alpha = \omega\lambda_{sv}$, $\beta = \omega\mu_{sv}$.

12.3 A viscoelastic phononic crystal

In order to make our point clear, we have picked a pathological case (but still very real in practice), in certain aspects. The system to be examined is an *fcc* crystal of close-packed rubber spheres in air. In particular, the mass density of air is $\varrho_{\text{air}} = 1.2\,\text{kg/m}^3$ and its respective speed of sound $c_{\text{air}} = 334\,\text{m/s}$. The rubber spheres have a mass density $\varrho_s = 1130\,\text{kg/m}^3$ and $c_{ls} = 1400\,\text{m/s}$, $c_{ts} = 94\,\text{m/s}$ are the compressional and shear speeds of sound, respectively. In addition, according to Ref. [171], three different viscoelastic levels are considered for the rubber spheres, namely: lossless spheres ($\alpha = \beta = 0$), a low viscous level ($\alpha_{\text{low}} = 0.5\,\text{MPa/s}$, $\beta_{\text{low}} = 0.01\,\text{MPa/s}$) and a high viscous level ($\alpha_{\text{high}} = 5\,\text{MPa/s}$, $\beta_{\text{high}} = 0.1\,\text{MPa/s}$). The viscoelastic properties used in this study are typical values for commercial rubbers, the variety of which is quite extensive and frequency dependent at high ultrasonic frequencies.

The on-shell layer MS method [19, 33] can treat very easily dissipative and dispersive materials either as scatterers or hosts. According to this method we view the crystal as a succession of planes of spheres parallel to the (111) *fcc* surface. The results are shown in Fig. 54. One clearly sees a number of flat bands which derive from the strongly interacting sharp resonant modes of the individual rubber spheres as result of the close-packing arrangement. Because these bands are so narrow in the present case, they are hardly observable, except that they introduce small gaps, above and below the main gap, which result from the hybridization of these flat bands with the broad-bands corresponding to nearly free propagating waves. These narrow gaps are seen more clearly in the transmission spectrum. Within the main gap these flat bands manifest themselves as sharp peaks in the transmission spectrum. When losses are present in the system, there are no true propagating waves and the band structure of the infinite lossless crystal is not of any help; therefore, the effect of the low viscous level is shown in the 2nd transmission spectrum [left (c)]. As anticipated from the results of the single sphere, the sharp peaks and dips of the resonant states disappear and we obtain a "clean" sonic gap without any resonant modes within it. The existence of the frequency gap means that sound does not propagate through the crystal when its frequency lies within the gap (the intensity of the wave decays exponentially into the crystal for these frequencies), and if it cannot enter into the crystal, it cannot be absorbed either.

In Fig. 54 we can also observe the close relation between absorption and transmission for normal incidence. A relatively large transmission coefficient implies that a correspondingly large fraction of sound has gone through the slab, with a consequent higher probability of being absorbed. However, since losses are due to the rubber spheres, absorption mainly occurs about the frequency regions where the modes of the acoustic field are mostly localized in the spheres. This explains why, outside the

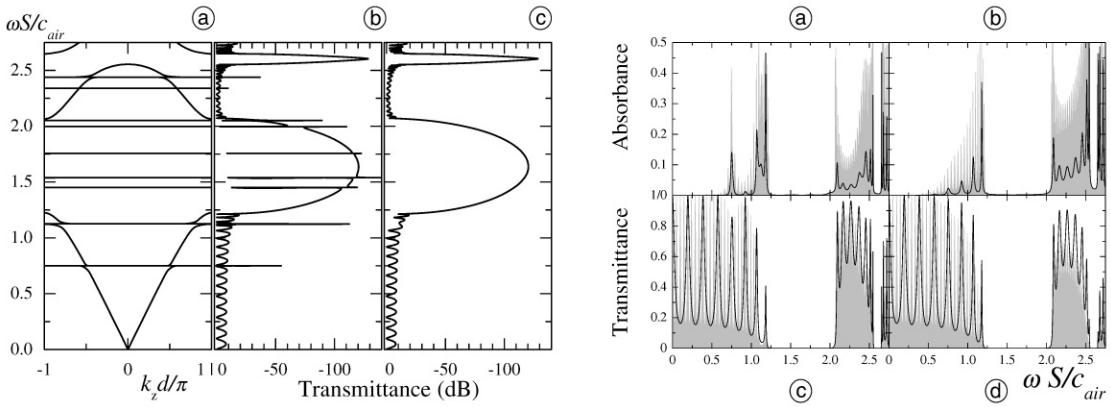

Fig. 54. On the left: The sonic band structure at the center of the SBZ of a (111) surface of an *fcc* crystal (of lattice constant *a*) of close-packed lossless rubber spheres in air (**a**). The corresponding transmittance curve of a slab of 16 layers parallel to the same surface is given in (**b**). In (**c**) the same transmittance curve is presented but with spheres of the low viscous level. *d* is the distance between successive (111) planes of the *fcc* crystal under consideration. On the right: Absorbance and transmittance curves of slabs of the rubber sonic crystal described on the left (a), consisting of 8 [(**a**), (**c**)] and 32 [(**b**),(**d**)] planes of spheres, respectively. The black line (shaded curve) corresponds to the low (high) viscous level. (After Psarobas, Ref. [169]).

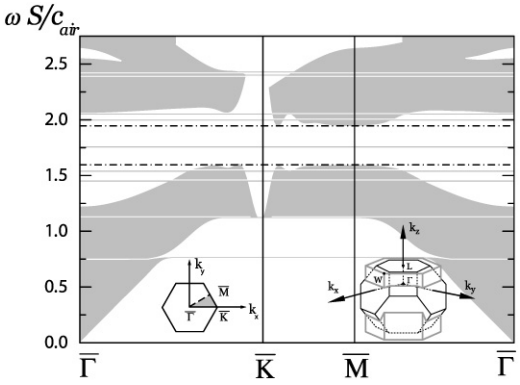

Fig. 55. Projection of the frequency band structure on the SBZ of the (111) surface of the *fcc* sonic crystal described in the caption of Fig. 54. The reduced k zone associated with the *fcc* (111) crystallographic plane with the (bulk) *fcc* Brillouin zone (right inset) and the corresponding surface Brillouin zone (left inset). (After Psarobas, Ref. [169]).

gap regions, absorption takes place essentially about the frequencies of the flat bands.

The induced resonant absorption on the scatterers, and not the host, serves as a cutoff in order to get around problems with disturbing resonant states on the frequency spectrum of the phononic crystal, which spoil the formation of clear omnidirectional frequency gaps and even useful partial gaps. This might be extremely useful in relation to waveguiding. Figure 55 demonstrates from the properties of the lossless "infinite" crystal, along all possible symmetry lines, what we can gain and benefit from dissipation in phononic lattices.

Part III: Experimental observations

13. Introduction

Phononic crystals can be built from plates, cylinders, spheres or any other object with elastic properties differing from those of the embedding medium. However, it is not a straightforward task to tailor a phononic crystal with large absolute (i.e. in all propagation directions and for all polarizations) band gap (band-gap engineering). Since elastic waves in a solid have both longitudinal and transversal components with different propagation velocities their corresponding gaps have to overlap. For example, phononic crystals composed of solid inclusions in a fluid or polymer are good candidates to obtain large spectral gaps.

The elastic wave propagation in an object containing inclusions with elastic properties different from those of the embedding medium is modified by MS (constructive and destructive interferences in the case that the dimensions of the objects and the wave length are of the same order) and refraction (due to different wave velocities of the objects and the surrounding medium). If there are strong density and velocity contrasts in a phononic crystal, Bragg diffraction peaks (related to pseudogaps) are transformed into broad attenuation bands. Coupling between shear modes and longitudinal modes also plays a crucial role and makes calculations very difficult.

A very important and beneficial property of phononic crystals is the scalability of the effects for frequencies from the Hz to the THz range, from seismic waves to phonons. This means that any phenomenon appearing in a phononic crystal for a certain range of frequencies and a given length scale can basically be extrapolated to other systems that are scaled up or down with respect to their frequencies and length scales.

There are numerous potential engineering applications of phononic crystals spanning many orders of magnitude, from thermal barriers, elastic/acoustic filters, vibrationless environments for high-precision mechanical systems, improved transducers, waveguides, acoustic lasers (phasers), acousto-optical devices, non-absorbing mirrors to sound protection devices and earth quake shields. In the following, experimental studies of phononic crystals, as far as they deal with their transmission (attenuation) or resonance spectra and/or their band structure, are reviewed. The work reviewed is grouped around possible applications. Tables 2–4 list phononic crystals studied so far experimentally. Table 5 gives the elastic properties of the materials used.

14. Experimental setup

The experimental setup is determined by the frequency of the elastic or acoustic wave to be used. If sound waves in the audible range are to be studied, the lattice parameters of a sonic crystal are of the order of 10 to 50 centimeters. The sound waves are produced by loudspeakers and detected by microphones. The whole setup should be set up in a sound-deadening chamber.

Since the properties of phononic crystals are scalable, it is space-saving to use ultrasound (Fig. 56). With frequencies of ≈ 1 MHz, the constituents of a phononic crystal and their distances shrink to ≈ 1 mm. This is significantly smaller than the diameters the of the transducers employed as ultrasound emitters and receivers. This allows to probe also more complex structures such as quasicrystals experimentally.

Table 2. 1D phononic crystals studied experimentally so far. In case of hollow (covered) objects the wall (cover) thickness is given in brackets.

Material of the objects	Object cross section [mm]	Periods of objects [mm]	Host material	Potential application reference
Acrylic glass (PMMA)	2	7.24	Water	Frequency filter James *et al.* (1995): Ref. [181]
$LiNbO_3+$	0.0036	0.0072	$LiNbO_3-$	Microwave absorption Lu *et al.* (1999): Ref. [183]
Silica glass	1.23 3.0	2.47 3.51	Water	Frequency filter Shen and Cao (1999): Ref. [182]

Table 3. 2D phononic crystals studied experimentally so far. In case of hollow (covered) cylinders or rods the wall (cover) thickness is given in brackets.

Material of the objects	Object cross section [mm]	Periods of objects [mm]	Host material	Potential application reference
Air	circular 60	honeycomb 210 hexagonal 140	marble	Seismic wave shield Meseguer *et al.* (1999): Ref. [205, 146]
Acrylic glass (PMMA)	circular 20.4	square 110	air	sonic shield Miyashita (2002): Ref. [197]
Aluminum	circular 40 (2)	square 110 hexagonal 63.5	air	acoustic interferometer Sanchis *et al.* (2003): Ref. [200]
Aluminum	circular 10, 20, 30, 40	hexagonal 63.5 Suzuki phase	air	sound control Caballero *et al.* (2001): Ref. [23]; Cervera *et al.* (2002): Ref. [148]
Aluminum steel or wood	circular 10, 20, 30, 40	hexagonal 63.5, 12.7 and square 55, 110	air	acoustic filter Rubio *et al.* (1999): Ref. [195] Sanchez-Perez *et al.* (1998): Ref. [22]
Copper	circular hollow 28 (1)	square 30	air	sonic shield Vasseur *et al.* (2002): Ref. [194]
Duralumin	circular 16	square 20 rectangular 20×40	epoxy	band gap Vasseur *et al.* (1998): Ref. [142]
Electrical conduit	circular hollow 23.4	square 37 hexagonal 37	air	sound control Robertson and Ruby (1998): Ref. [143]
Mercury, air or baby oil	circular 2	square 2.73, 2.80 . . .	aluminum	band gap Garcia-Pablos *et al.* (2000): Ref. [15]; Montero de Espinoza *et al.* (1998): Ref. [144]; Torres *et al.* (1999): Ref. [145]
Mercury	circular 2	twinned square 28	aluminum	wave splitting Torres *et al.* (2001): Ref. [147]
PVC	circular hollow 160	hexagonal 220	air	sonic shield Sanchez-Perez *et al.* (2002): Ref. [193]
Steel	square hollow 30 (3)	square 42.5	air	sonic shield Goffaux *et al.* (2003): Ref. [198]
Steel	circular 2.5	square 3.0	water	sonic shield Khelif *et al.* (2003; 2004): Ref. [210]
Steel	circular 4	hexagonal 6.023	epoxy	waveguide Vasseur *et al.* (2001): Ref. [17]
Steel	circular 5 and rubber coated circular 4 (1)	square 7	epoxy	ultrasound filter Zhang *et al.* (2003): Ref. [204]
Steel	circular 1	Penrose tiling 1.7 triangular 1.5	water	Sutter *et al.* (2004): Ref. [192]
Silica glass	circular full and hollow 0.08 (0.01)	square 0.08	air	acousto-optic devices Russel *et al.* (2003): Ref. [213]
Silica glass	spherical 1.12	square 2.63	polyester	Frequency filters Henderson *et al.* (2000): Ref. [184]
Steel	spherical	square, hexagonal random	polyester	Frequency filters Kinra *et al.* (1998, 1999): Ref. [185, 186]
Silica glass lead steel WC	spherical 0.56 0.6 0.585 0.245	square square square, hexagonal square	polyester	selective filters Maslov *et al.* (1999, 2000): Ref. [188, 189]; Maslov and Kinra (1999): Ref. [187]; Torres *et al.* (1999): Ref. [145]

The parameters controlling existence, position and width of absolute band gaps are the topology of the structure (symmetry and order), packing density (filling factor), contrast in elastic constants, wave velocities and densities of the objects building the phononic crystal as well as their shape and internal structure.

The influence of the limited size of the phononic crystal (the length of rods should be larger than the wavelength to ensure 2D behavior), of container walls and the supporting structure as well as of misalignments and size variations of the building objects has to be controlled. This is also true for the existence of inhomogeneities (air bubbles in a liquid medium, pores and inclusions in solid media etc.).

However, for almost all experiments reported in literature so far, the total number of scattering objects in the studied phononic crystals was rather small. This is also true for the ratio (diameter of the transducer)/(lattice para-

Table 4. 3D phononic crystals studied experimentally so far. In case of hollow (covered) objects the wall (cover) thickness is given in brackets.

Material of the objects	Object cross section [mm]	Periods of objects [mm]	Host material	Potential application reference
Aluminum	spherical 3	randomly dense	air	band gap Turner *et al.* (1998): Ref. [191]
Amorphous silica	spherical $\approx 0.00015-0.0002$	*fcc* $\approx 0.0003-0.0004$	air	nanoacoustics Bogomolov *et al.* (2002): Ref. [208]
Lead	rubber coated spherical 10 (2.5)	cubic 15.5	epoxy	sonic shield Sheng *et al.* (2003): Ref. [201]; Liu, Zhang *et al.* (2000): Ref. [168]
Silica glass steel	spherical 1 spherical 0.55	cubic 2.54 tetragonal $1.32 \times 1.32 \times 2.63$	epoxy acrylic glass	band gaps Kinra and Ker (1983): Ref. [180]
Steel Steel, lead	spherical 11 spherical 16, 19	tetragonal $16 \times 16 \times 20$ tetragonal $30 \times 30 \times 20$	rubber in rigid plastic frame	sonic shield Ho *et al.* (2003): Ref. [203]
Steel	spherical 1.17	tetragonal $2.63 \times 2.63 \times 5.26$	acrylic glass	band gap Henderson *et al.* (2001): Ref. [190]
Steel	spherical 0.8	*hcp* $0.8 \times 0.8 \times 1.306$	water	band gap Liu, Chan *et al.* (2000): Ref. [13]
WC	spherical 0.8	*fcc* 1.6	water	ultrasound tunneling Yang *et al.* (2002): Ref. [149]

meter), which amounts only to ≈ 2 in most cases. This plays a role for the study of more complex structures or defect structures and, in particular, for the comparison with band structure calculations, which are usually based on infinite periodic systems.

Theoretical calculations are often based on systems with strong contrasts in the elastic properties of the components of the phononic crystal, which cannot be fabricated experimentally such as mercury or air cylinders or bubbles in water. For practical purposes and potential applications materials of choice are steel, glass, etc. embedded in polymers or water.

Up to date, mostly very simple structures (hexagonal or square packing of cylinders, hexagonal or cubic dense packing of spheres, etc.) have been studied experimentally. It is well known that, for instance, the reduction of the total symmetry of the phononic crystal can remove bad degeneracies, allowing for the appearance of complete gaps. An example is the comparison between diamond and zinc-blende crystals [7].

15. Experimental studies

The goal of experimental studies is to explore elastic wave propagation in phononic crystals as a function of materials employed as well as of structure and structural ordering. In not so far future theoretical modeling will probably

Table 5. Parameters of materials used for the fabrication of phononic crystals studied experimentally so far. c_l and c_t are the respective compressional and shear sound wave speeds.

Material	Mass density [Mgm^{-3}]	*cl* [ms^{-1}]	*ct* [ms^{-1}]	Reference
Acrylic glass (PMMA)	1.180	2750	–	James *et al.* (1995): Ref. [181]
Air	0.0013	340	–	Caballero *et al.* (2001): Ref. [23]
Alluminum	2.73	6420	3040	Lide (2001): Ref. [214]
Copper	8.950	4330	2900	Vasseur *et al.* (2002): Ref. [194]
Duralumin	2.799	6342	3095	Vasseur *et al.* (1998): Ref. [142]
Epoxy R125	1.142	2569	1139	Vasseur *et al.* (1998): Ref. [142]
Lead	11.3	2210	860	Maslov *et al.* (2000): Ref. [189]
Marble	2.80	6000	3217	Messeguer *et al.* (1999): Ref. [205, 146]
Mercury	13.50	1450	–	Klironomos and Economou (1998): Ref. [215]
Polyester	1.22	2490	1180	Maslov *et al.* (2000): Ref. [189]
Rubber, gum	0.92	1550	–	Lide (2001): Ref. [214]
Silica glass	2.49	5660	3300	Maslov *et al.* (2000): Ref. [189]
Steel	7.8	5940	3200	Maslov *et al.* (2000): Ref. [189]
Tungsten	19.25	5090	2800	Lide (2001): Ref. [214]
WC	15.6	6660	3980	Maslov *et al.* (2000): Ref. [189]
Water	1.0	1490	–	Yang *et al.* (2002): Ref. [149]

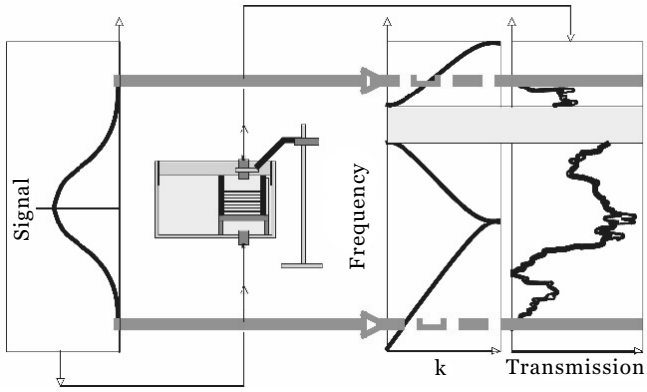

Fig. 56. Experimental setup for a ultrasound transmission experiment. A ultrasound pulse with Gaussian frequency distribution is transmitted through a phononic crystal (steel rods in water). The received signal gives information about the transmission spectrum and the band structure (from Sutter, 2003) [174].

make experiments unnecessary. Nowadays, however, large non-periodic structures still cannot be modeled properly on a reasonable timescale. Experiments are still orders of magnitude faster. Furthermore, real phononic crystals, which may be used for a practical applications, always are finite, show some structural disorder due to inaccuracies in the fabrication process, tolerances in the materials dimensions, inhomogeneities at interfaces. This cannot be modeled properly and its possible influence on the properties of the phononic crystal has to be investigated by comparison of experimental results and theoretical predictions.

15.1 Early studies

Starting in the fifties, the propagation of elastic waves through periodic composite materials was studied on several examples and first suggestions for applications such as frequency filters came up (for a review see, e.g., Ref. [175]). Strong geometric dispersion effects were found in one-dimensional (1D) layered composites consisting of periodically arranged boron fibers and carbon cloth for ultrasound waves propagating parallel to the laminates [176]. Pass and stop bands were found in 1D layered composites consisting of steel and copper foils [177]; in 2D fibrous composites made up of tungsten wires in aluminum [178], boron fibers in epoxy [179] or piezoelectric PZT rods in different polymers [94]; in 3D composites consisting of glass spheres (1 mm diameter, cubic array with period 2.54 mm) in epoxy and steel balls (0.55 mm diameter, tetragonal array with unit cell $1.32 \times 1.32 \times 2.63$ mm^3) acrylic glass [180]. The application of these composites as wave filters was already proposed by Sutherland and Lingle [178]. Kinra and Ker [180] point out that "an important property of the periodic heterogenous materials is the phenomenon of pass bands and stop bands". The wonder why at wavelengths comparable to the sphere diameters no more stop bands are observed and the dispersion curve becomes continuous. This may be explained by the rather strong deviations from a perfect tetragonal structure of their spheres in acrylic glass (see Fig. 2 of Ref. [180]).

Between 1983 and 1992, there was no much activity left studying the properties of periodic composite structures. The increasing interest in photonic crystals, however, induced also a revival of the research in these structures. The term 'phononic crystal' was coined in analogy to 'photonic crystals' by Kushawa *et al*. [7].

15.2 Frequency filters

Frequency filters should ideally posses a very broad omnidirectional band gap and, in its center, a very narrow pass band. There should also be an easy way to tune the frequency of the pass band.

Depending on the application 1D, 2D or 3D structures may be employed. 1D multilayer structures can be rather easily fabricated down to the nanometer scale, for instance. The lattice parameter seen by the elastic waves depends on the angle of incidence, however. A virtual increase of the lattice parameter due to oblique incidence would shift stop and pass band to lower frequencies.

15.2.1 1D arrays of plates

The transmission of ultrasound through a periodic array of 2–10 perspex (PMMA, acrylic glass) plates (2 mm thick, 7.24 mm period) in water was studied by James *et al.* [181]. A vacancy defect, formed by removing one of the plates, resulted in a sharp transmission peak at ≈ 2.25 MHz in the center of stop band between ≈ 2.0 and ≈ 2.5 MHz.

Structures of glass plates (0.51–3 mm thickness) in water consisting of two subsets with different periods have been studied by Shen and Cao [182]. The authors demonstrate that depending on the arrangement either a sharp passband (transmission coefficient ≈ 0.6) or a broad stopband (transmission coefficient < 0.03) can be achieved.

A phononic crystal composed of two sets of periodically aligned (7.2 mm period) ferroelectric $LiNbO_3$ layers with opposite spontaneous polarization was studied by Lu *et al.* [183]. This structure is somehow related to an ionic crystal since the plates carry opposite electric charges constituting dipoles, which can interact with EM radiation. Indeed, a strong microwave absorption peak at 502 MHz indicates a polariton mode, i.e. a coupling mode of photons and optical phonons. The coupling between vibrations of the multilayer structure and EM waves results in various long-wavelength optical properties, such as microwave absorption, dielectric abnormality, and polariton excitation, that originally exist in ionic crystals.

15.2.2 2D arrays of spheres

The diffraction of broadband longitudinal ultrasonic pulses by a 2D square periodic array (2.63 mm period) of glass spheres (1.12 mm diameter) embedded in polyester was studied by Henderson *et al.* [184]. Longitudinal ultrasonic waves are diffracted as both longitudinal and shear waves due to mode conversion. Particular interest was on the shear waves generated. Not surprisingly, reflection peaks were observed according to Bragg's law.

Kinra *et al.* [185, 186] investigated the influence of order (square, hexagonal, random) and filling fraction (0.14 to near close packed 0.92) of glass spheres in polyester. The specimens with random order do not exhibit any structure in their transmission spectra, the square and the

hexagonal arrangements showed different gaps for low (≈ 0.14) and high (≈ 0.57) filling fraction but similar ones in between (≈ 0.28).

Experiments on singular square and hexagonal layers of spheres (glass, steel, tungsten carbide, lead) embedded in polyester were carried out by Maslov *et al.* [187–189]. The resonance (transmission) spectra are similar with one big maximum (minimum) between 0.8 and 1 MHz. The only exception is the tungsten-carbide fibers containing specimen, which has a very low filling ratio of just 1%.

15.2.3 3D arrays of spheres

A tetragonal phononic crystal ($2.63 \times 2.63 \times 5.26\ \text{mm}^3$) of steel balls (1.13 mm diameter) embedded in acrylic glass was investigated by Henderson *et al.* [190]. Despite the very low packing density of just 2.3% a narrow stop band was observed for ultrasound waves propagating along [001]. The authors demonstrate that some properties of higher-density phononic crystals [180, 188] can be predicted based on these data.

Ultrasound tunneling through a phononic crystal consisting of cubic close packed tungsten carbide spheres in water was studied by Yang *et al.* [149]. Along [111] a gap was identified between 0.8 and 1.2 MHz and a complete gap around ≈ 1 MHz. Evidence for tunneling was provided by the measuring the transit time of ultrasound pulses with a midgap frequency. While the transit time of normally propagating waves increases linearly with the thickness of the phononic crystal, the tunneling time is just inversely proportional to the width of the gap.

Band structure and transmission spectra of a phononic crystal made up of hexagonally close packed steel balls (0.8 mm diameter) in water were studied by Liu, Chan *et al.* [13] in order to demonstrate the applicability of the their model based on MS theory.

Several randomly densely packed weakly sintered arrays of aluminum beads (3 mm diameter) were probed by ultrasound [191]. The different stop bands observed are interpreted arising from the coupling of the many internal degrees of freedom of the beads.

15.2.4 2D arrays of cylinders

The properties of band gaps obtained by a hexagonal arrangement (6.023 mm period) of steel cylinders (4 mm diameter) in epoxy were studied by Vasseur *et al.* [17]. Two complete band gaps were found from 124–276 kHz and 441–483 kHz. For a square (20 mm period) and a centered rectangular (20×40 mm unit cell) array of Duralumin cylinders (16 mm diameter) in epoxy a complete gap between 60 and 90 kHz was observed in agreement with theoretical calculations [142].

Square arrays (2.73 and 2.80 mm periods, respectively) of cylinders (2 mm diameter) of fluids (mercury, oil, air) in aluminum were studied by Garcia-Pablos *et al.* [15]. Strongest attenuation (40–80 dB) was found between ≈ 0.75 and ≈ 1 MHz for mercury. The agreement between experimental and calculated (by FDTD) attenuation spectra was rather poor.

The properties of a phononic crystal, consisting of a rectangular array of vacancies on a hexagonal array (63.5 mm period) of Al cylinders (40 mm diameter, 1 m length) in air were studied by Caballero *et al.* [23]. Stop bands for the resulting structure (Suzuki phase) have been found related to both the order of vacancies at lower frequencies and the triangular host lattice at higher frequencies. A complete band gap was found around ≈ 1.4 MHz for a ratio ≈ 0.36 of the cylinder radius and the nearest neighbor distance. This experiment built on previous investigations on the properties of square, hexagonal and honeycomb structures formed by aluminum cylinders in air [128]. The influence of symmetry reduction on the size of the band gap was studied by placing cylinders with smaller diameter at the centers of the unit cells. The largest band gaps were obtained for diameter ratios of the cylinders of 0.1–0.3.

For the first time, fivefold symmetric quasiperiodic arrays (Penrose rhomb tiling) of steel rods (1 mm diameter, 1.7 mm edge length of the rhomb tiles) in water have been investigated in comparison with a hexagonal structure by Sutter, Krauss and Steurer [192]. In the hexagonal structure, (filling fraction 0.4) several large partial band gaps and one small omnidirectional gap (around 1.6 MHz) were observed. In the Penrose phononic crystal, the spectrum was rather spiky with many narrow partial gaps and a few narrow omnidirectional gaps (around 0.45, 0.62 and 0.76 MHz).

15.3 Noise attenuation and sonic shields

An important potential application is the attenuation of traffic noise along highways. It would be very benificial if this could be done in a more efficient and more aesthetical way than nowadays.

15.3.1 2D arrays of cylinders

The sound attenuation of a sculpture by the Spanish artist Eusebio Sempere was demonstrated by Martinez-Sala *et al.* [139]. It consists of square-periodically (100 mm period) arranged hollow steel cylinders (29 mm diameter). A significant sound attenuation was found around 1.67 kHz.

The ability of phononic crystals to attenuate road, aircraft or factory noise was demonstrated in an outdoor experiment using a sculpture of hollow cylindrical PVC rods (160 mm diameter) mounted in a triangular pattern [193]. The average sound attenuation measured is between 10 and 20 dB for frequencies between 1 and 4 kHz.

A significant band gap was found for a square array (30 mm period) of hollow copper cylinders (28 mm diameter, 1 mm wall thickness) in air [194]. For waves propagating along [100] the gap extends from 4 to 6.8 kHz.

In other experiments strong attenuation of sound waves was obtained employing periodic arrays of steel cylinders [22], hollow copper cylinders [194], aluminum cylinders of two different diameters [128], wood cylinders [22, 195], electrical conduits [143] and water-filled soft-polymer tubes [196], respectively, all in air.

Miyashita [197] studied a sonic crystal with acrylic cylinders (20.4 mm diameter) on a square grid (24 mm period) in air. He found a complete gap between 6.8 kHz and 9.5 kHz with a transmission ratio smaller than -25 dB.

Hollow steel rods with square cross section (50 cm length, 3 cm side length, 3 mm wall thickness) were arranged on a square lattice (4.25 cm period), 40° rotated with respect to the lattice [198]. In the spectral range studied (0–15 kHz), sound attenuation up to 30 dB (2–6 kHz) was observed. Bypassing effects due to the rather small size of the sonic crystals lead to a saturation of the attenuation inside the gaps.The authors compared their results with the attenuation, which could be achieved by a homogenous slab of the same mass. The phononic crystal is superior for a thickness of more than 9 periods. Since it is an open structure it is also advantageous if, for instance, a heat exchanger with good acoustical insulation is needed.

15.4 Refractive acoustic devices

Devices based on the difference in refractive indices of phononic crystals and the surrounding medium could be used for lenses for sonic or ultrasound waves.

15.4.1 2D arrays of cylinders

An acoustic biconvex lens made of hexagonally arranged aluminum cylinders (40 mm diameter) in air has been studied experimentally by Cervera *et al.* [148]. The speed of sound inside the lens is with ≈ 270 m/s less than in air and the impedance contrast between the lens and air is small. For frequencies around 1700 Hz there is a clear focusing effect (20 dB) with a focus 70 cm from the lens.

An acoustic interferometer composed of hollow aluminum cylinders (40 mm diameter, 2 mm wall thickness) arranged on either a square or a hexagonal grid (period 110 and 63.5 mm, respectively) in air was studied experimentally and theoretically by Sanchis *et al.* [199, 200]. As a function of the number of lattice layers as well as the filling fraction the reflectance was measured. One result is that the hexagonal structure is isotropic and the square lattice biaxial regarding sound propagation. The authors conclude that sonic crystals of this kind act like Fabry-Perot cavities for light waves.

15.5 Three-component elastic wave band-gap materials

Local resonance of the scattering objects of a phonic crystal can shift the scale by several orders of magnitude. This makes more feasible potential applications such as sound protection or even earthquake protection.

15.5.1 3D arrays of spheres

Experiments with a cubic array (period 15.5 mm) of rubber coated Pb spheres (10 mm diameter, 2.5 mm layer thickness) in an epoxy matrix were performed by Liu *et al.* [13, 34, 168] and Sheng *et al.* [201]. Due to localized resonances (with negative dynamic elastic constants) spectral gaps at frequencies two order of magnitudes lower are found than what is obtained from Bragg scattering of uncoated spheres. Thus, by appropriate coating the size of the objects in a phononic crystal can be uncoupled from the wavelength of the elastic wave. This is very important in some cases such as for seismic waves reaching wavelengths of kilometers.

Sheng *et al.* [201] studied a cubic sonic crystal (15.5 mm period) of rubber coated lead spheres (10 mm diameter, 2.5 mm coating thickness) in epoxy. They investigated the spectra only in the audible frequency range. Two minima with ≈ 0.001 transmission (compared to a maximum transmission of 0.03) were found at ≈ 400 Hz and ≈ 1350 Hz along the [100] direction. For a frequency of 400 Hz the wavelength in epoxy is ≈ 6.4 m.

The low-frequency attenuation of sound by rubber-coated lead spheres in concrete was investigated by Li *et al.* [202]. An enhancement of attenuation by ≈ 20 dB in the frequency range around 150 Hz was found.

Multilayer panels consisting of lead or steel spheres, respectively, embedded in silicone rubber and kept in a rigid plastic square grid were investigated by Ho *et al.* [203]. For ball diameters between 11 and 19 mm significant attenuation of the transmission was observed in a frequency range of 200–500 Hz. The average transmission intensity for a composite multilayer panel (one layer of 16 mm steel balls, one of 16 mm lead spheares, and one layer of 19 mm steel balls) was up to 11 dB lower than that dictated by the mass-density law (for a density of 7 Mg m^{-3}). Since locally resonant materials show stronger attenuation only around the resonance frequency, the combination of several layers of local resonators differing in size and material can act as a broadband sonic shield.

15.5.2 2D arrays of cylinders

An ultrasound experiment with rubber coated steel cylinders (4 mm diameter and 1 mm thick coating) arranged on a square grid (7 mm period) in epoxy showed a drastic increase in the width of the band gap ($\approx$ 200–450 kHz) compared to the uncoated cylinders (5 mm diameter) [204]. Transmission spectra at lower frequencies have not been studied.

15.6 Seismic waves and water waves

Earthquake and coastal protection by phononic crystals are only feasible if the structures needed are significantly smaller than the wavelengths that are of the order of several hundred meters.

15.6.1 2D arrays of cylinder

A feasibility study of the attenuation of surface waves (seismic waves such as Rayleigh waves, i.e. a combination of shear and transverse modes) was successfully performed by Meseguer *et al.* [146, 205] on a large block of marble with an ordered honeycomb and a hexagonal array (140 mm period) of holes (60 mm diameter, 1.6 m deep), respectively. Omnidirectional attenuation bands (>10 dB) were found around 0–2 kHz and 10–15 kHz.

The propagation of surface waves on aluminum-coated glass plates with 1D square-wave surface relief (3 m grating period, 1.15 m relief depth, e.g.) was studied by a laser-based picosecond transient grating method [206]. The surface grating induces surface and bulk resonance mode mixing. Significant gaps were found at the zone boundaries.

The importance of understanding the wave interaction with arrays of offshore structures in the ocean is underlined in a review by McIver [207]. For instance, the thousands of supporting columns for floating airports can act like a large phononic crystal.

15.7 Nanosystems

15.7.1 3D arrays of spheres

Thermal conductivity measurements on synthetic single-crystalline opals (composed of nanospheres of amorphous SiO2) showed an order-dependent lowering of the thermal conductivity (for $T < 20$ K) when the phonon wavelength approaches the diameters of the contact areas ($\approx$40 Å) between the SiO_2 spheres [208]. The first-order amorphous SiO_2 spheres form a *fcc* structure with a period of 3000–4000 Å. The effects are discussed in terms of a 3D array of intersecting nanowaveguides (i.e. along the chains of SiO_2 spheres).

15.8 Waveguides, wavelength demultiplexing

15.8.1 2D arrays of cylinders

Localized defect modes and their interaction have been investigated experimentally in a square phononic crystal (3 mm period) consisting of steel cylinders (2.5 mm diameter, 150 mm length) in water [209]. There is a complete band gap in the range 260–312 kHz. By removing every other cylinder in a row along the propagating direction of the sound wave a defect mode at the center of this gap was formed. The broad transmission (nearly 100%) peak could be used for waveguiding. This was demonstrated in another experiment employing straight as well as bent waveguides [210]. Removing just one row of steel cylinders showed a waveguiding band extending from ≈ 270 to ≈ 310 kHz.

A 90° bending waveguide manufactured of acrylic cylinders in air was investigated by Miyashita and Inoue [211]. Loss to due side leakage was ≈ 30 dB in the full band gap of the phononic crystal.

A device for elastic wave bending and splitting without the requirement of a full gap was proposed by Torres *et al.* [147]. It is based on square array (2.8 mm period) of mercury cylinders (2 mm diameter) in aluminum [145]. Four wedge-like domains of this structure, related by a 45° rotation (twinning), make up the device. It allows 45° and 90° bending of the elastic wave by making use of refraction at the domain boundaries enhanced by the directional gaps. Modular structures (tiling) resulting from arbitrary arrangements of triangular domains are proposed.

The method of topology optimization was employed for the systematic design of phononic crystals to be used for wave damping or waveguiding by Sigmund and Jensen [212].

15.9 Defects in phononic crystals

The sonic resonances were studied experimentally of two coupled solid defects in a square array of channels (59 m diameter, 80 m period) and rods in a silica glass photonic fibre preform [213]. There is a broad band-gap around 25 MHz. The localized resonances at ≈ 23 and ≈ 23.25 MHz were monitored by Laser interferometry. The refractive index of the glass varies as a function of the strength of the vibrations and can induce a phase change of the laser beam. The authors see an application as an efficient optical modulator or acoustic-optically pumped acoustic oscillator.

Acknowledgments. M. S. Kushwaha thanks his collaborators, P. Halevi, G. Martinez, L. Dobrzynski, B. Djafari-Rouhani, J. O. Vasseur, A. Akjouj, X. F. Wang and P. Vasilopoulos without whose diverse set of talents to bear on this exciting problem this work would not have come about and who are co-authors of a number of research papers referenced in this review. In addition, he thanks Professor Sajeev John, Professor W. A. Smith and Professor R. L. Weaver for providing many of their reprints/preprints referenced in this work. This work was partially supported by CONACyT Grant No. SEP-2003-C02-42761.

Dr. I. E. Psarobas expresses his deepest appreciation to N. Stefanou and A. Modinos for many useful discussions on phononic crystals and related problems.

References

[1] Joannopoulos, J. D.; Meade, R. D.; Winn, J. N.: Photonic Crystals. Princeton University Press, Princeton, NJ (1995).
[2] Soukoulis, C. M. (Ed.): Photonic Band Gap Materials. Kluwer Academic, Dordrecht (1996).
[3] For an early extensive review of electronic, photonic, and phononic band-gap crystals see Kushwaha, M. S.: Classical band structure of periodic elastic composites. Int. J. Mod. Phys. B**10** (1996) 977–1094.
[4] Kushwaha, M. S.: Band gap engineering in phononic crystals. Recent Res. Devel. Appl. Phys. **2** (1999) 743.
[5] Modinos, A.; Stefanou, N.; Psarobas, I. E.; Yannopapas, V.: On wave propagation in inhomogeneous systems. Physica B**296** (2001) 167–173.
[6] Sigalas, M.; Economou, E. N.: Elastic and acoustic wave band structure. J. Sound Vib. **158** (1992) 377.
[7] Kushwaha, M. S.; Halevi, P.; Dobrzynski, L.; Djafari-Rouhani, B.: Acoustic Band Structure of Periodic Elastic Composites. Phys. Rev. Lett. **71** (1993) 2022–2025.
[8] Wu, F. G.; Hou, Z. L.; Liu, Z. Y; Liu, Y. Y.: Point defect states in two-dimensional phononic crystals. Phys. Lett. A**292** (2001) 198–202.
[9] Manzanares-Martínez, B.; Ramos-Mendieta, F.: Surface elastic waves in solid composites of two-dimensional periodicity. Phys. Rev. B**68** (2003) 134303.
[10] Korringa, J.: On the Calculation of the Energy of a Bloch Wave in a Metal. Physica **XIII** (1947) 392.
[11] Kohn, W.; Rostoker, N.: Solution of the Schrödinger Equation in Periodic Lattices with an Application to Metallic Lithium. Physical Review **94** (1954) 1111.
[12] Kafesaki, M.; Economou, E. N.: Multiple-scattering theory for three-dimensional periodic acoustic composites. Phys. Rev. B**60** (1999) 11993.
[13] Liu, Z. Y.; Chan, C. T.; Sheng, P.; Goertzen, A. L.; Page, J. H.: Elastic wave scattering by periodic structures of spherical objects: Theory and experiment. Phys. Rev. B**62** (2000) 2446–2457.
[14] Mei, J.; Liu, Z. Y.; Shi, J.; Tian, D.: Theory for elastic wave scattering by a two-dimensional periodical array of cylinders: An ideal approach for band-structure calculations. Phys. Rev. B**67** (2003) 245107.
[15] García-Pablos, D.; Sigalas, M.; Montero de Espinoza, F. R.; Torres, M.; Kafesaki, M.; García, N.: Theory and Experiments on Elastic Band Gaps. Phys. Rev. Lett. **84** (2000) 4349–4352.
[16] Tanaka, Y.; Tomoyasu, Y.; Tamura, S.: Band structure of acoustic waves in phononic lattices: Two-dimensional composites with large acoustic mismatch. Phys. Rev. B**62** (2000) 7378–7392.

[17] Vasseur, J. O.; Deymier, P. A.; Chenni, B.; Djafari-Rouhani, B.; Dobrzynski, L.; Prevost, D.: Experimental and Theoretical Evidence for the Existence of Absolute Acoustic Band Gaps in Two-Dimensional Solid Phononic Crystals. Phys. Rev. Lett. **86** (2001) 3012.
[18] Sigalas, M. M.; García, N.: Theoretical study of three dimensional elastic band gaps with the finite-difference time-domain method. J. Appl. Phys. **87** (2000) 3122–3125.
[19] Psarobas, I. E.; Stefanou, N.; Modinos, A.: Scattering of Elastic Waves by Periodic Arrays of Spherical Bodies. Phys. Rev. B**62** (2000) 278.
[20] Pendry, J. B.: Low Energy Electron Diffraction. Academic Press, London (1974).
[21] Modinos, A.: Field, Thermionic and Secondary Electron Emission Spectroscopy. Plenum Press, New York (1984).
[22] Sánchez-Pérez, J. V.; Caballero, D.; Mártinez-Sala, R.; Rubio, C.; Sánchez-Dehesa, J.; Meseguer, F.; Llinares, J.; Gálvez, F.: Sound Attenuation by a Two-Dimensional Array of Rigid Cylinders. Phys. Rev. Lett. **80** (1998) 5325–5328.
[23] Caballero, D.; Sánchez-Dehesa, J.; Martínez-Sala, R.; Rubio, C.; Sánchez-Pérez, J. V.; Sanchis, L.; Meseguer, F.: Suzuki phase in two-dimensional sonic crystals. Phys. Rev. B**64** (2001) 064303.
[24] Goffaux, C.; Sánchez-Dehesa, J.: Two-dimensional phononic crystals studied using a variational method: Application to lattices of locally resonant materials. Phys. Rev. B**67** (2003) 144301.
[25] Wang, G.; Wen, J. H.; Liu, Y. Z.; Wen, X.: Lumped-mass method for the study of band structure in two-dimensional phononic crystals. Phys. Rev. B**69** (2004) 184302.
[26] Ashcroft, N. W. and Mermin, D. N.: Solid State Physics. Holt, Rinehart and Winston (1976).
[27] Ham, F. S.; Segall, B.: Energy Bands in Periodic Lattices: Green's Function Method. Physical Review **124** (1961) 1786.
[28] Segall, B.; Ham, F. S.: Methods in Computational Physics, Vol 8. Academic Press, London (1968). pp. 251–293.
[29] Wang, Xindong; Zhang, X.-G.; Yu, Qingliang; Harmon, B. N.: Multiple-Scattering Theory for Electromagnetic Waves. Phys. Rev B**47** (1993) 4161.
[30] Moroz, Alexander: Density-of-States Calculations and Multiple-Scattering Theory for Photons. Phys. Rev. B**51** (1995) 2068. Inward and Outward Integral Equations and the KKR Method for Photons. J. Phys.: Condens. Matter **6** (1994) 171.
[31] Stefanou, N.; Karathanos, V.; Modinos, A.: Scattering of Electromagnetic Waves by Periodic Structures. J. Phys.: Condens. Matter **4** (1992) 7389.
[32] Kafesaki, M.; Penciu, R.S.; Economou, E. N.: Air Bubbles in Water: A Strongly Multiple Scattering Medium for Acoustic Waves. Phys. Rev. Lett. **84** (2000) 6050.
[33] Sainidou, R.; Stefanou, N.; Psarobas, I. E.; Modinos, A.: A layer-multiple-scattering method for phononic crystals and heterostructures of such. Comput. Phys. Commun. **166** (2005) 197–240.
[34] Liu, Z. Y.; Chan, C. T.; Sheng, P.: Three-component elastic wave band-gap material. Phys. Rev. B**65** (2002) 165116.
[35] Abramowitz, M.; Stegun, I.: Handbook of Mathematical Functions. Dover Publications. New York (1970).
[36] Edmonds, A. R.: Angular Momentum in Quantum Mechanics. Princeton University Press, Princeton, NJ (1974).
[37] Straton, J. A.: Electromagnetic Theory. McGraw-Hill, New York (1941).
[38] Kafesaki, M.; Economou, E. N.: Interpretation of the Band Structure Results for Elastic and Acoustic Waves by Analogy with the LCAO Approach. Phys. Rev. B**52** (1995) 13317.
[39] Kafesaki, M.: Scattering and Propagation of Elastic Waves in Random Media. PhD thesis, University of Crete (1997).
[40] Ewald, P.: Evaluation of optical and electrostatic lattice potentials. Ann. Phys. **64** (1921) 253.
[41] Landau and Lifshitz: Theory of Elasticity. Pergamon Press, Oxford (1986).
[42] Smith, G. D.: Numerical Solution of Partial Differential Equations: Finite Difference Methods. Claredon Press, Oxford.
[43] Clayton, R.; Engquist, B.: Absorbing Boundary Conditions for Acoustic and Elastic Wave. Bull. Seism. Soc. Am. **67** (1977) 1529.
[44] Zhou, J.; Saffari, N.: Absorbing Boundary Conditions for Elastic Media. Proc. R. Soc. London, Part A **452** (1996) 1609.
[45] Zhou, J.; Saffari, N.: Constructing Absorbing Boundary Conditions from Prescribed Elastic-Wave Incidences. Bull. Seism. Soc. Am. **87** (1997) 1324.
[46] Taflove, A.: Computational Electrodynamics: The Finite Difference Time Domain Method. Artech House, Boston, 1995.
[47] Chan, C. T.; Datta, S.; Yu, Q. L.; Sigalas, M. M.; Ho, K. M.; Soukoulis, C. M.: New Structures and Algorithms for Photonic Band Gaps. Physica A**211** (1994) 411.
[48] Chan, C. T.; Yu, Q. L.; Ho, K. M.: Order-N Spectral Method for Electromagnetic Waves. Phys. Rev. B**51** (1995) 16635.
[49] Fan, S.; Villeneuve, P. R.; Joannopoulos, J. D.: Large Omnidirectional Band Gaps in Metallodielectric Photonic Crystals. Phys. Rev. B**54** (1996) 11245.
[50] Mekis, A.; Chen, J. C.; Kurland, I.; Fan, S.; Villeneuve, P. R.; Joannopoulos, J. D.: High Transmission through Sharp Bends in Photonic Crystal Waveguides. Phys. Rev. Lett. **77** (1996) 3787.
[51] Sigalas, M. M.; Biswas, R.; Ho, K. M.; Soukoulis, C. M.; Crouch, D. D.: Waveguides in Three-dimensional Metallic Photonic Band-Gap Materials. Phys. Rev. B**60** (1999) 4426.
[52] Mur, G.: Absorbing Boundary Conditions for the Finite Difference Approximation of the Time-domain Electromagnetic Field Equations. IEEE Trans. Electromagnetic Compatibility **23** (1981) 377.
[53] Liao, Z. P.; Wong, H. L.; Yang B. P.; Yuan Y. F.: A Transmitting Boundary for Transient Wave Analyses. Scientia Sinica (Series A) **XXVII** (1984) 1063.
[54] Anderson, P. W.: Absence of Diffusion in Certain Random Lattices. Phys. Rev. **109** (1958) 1492. Mott, N. F.: Electrons in disordered structures. Adv. Phys. **16** (1967) 49.
[55] Dean, P.; Bacon, M. D.: Proc. Phys. Soc (London) **81** (1963) 642.
[56] Hodges, C. H.: Confinement of vibration by structural irregularity. J. Sound Vib. **82** (1982) 411.
[57] Ye, Z.; Alvarez, A.: Acoustic Localization in Bubbly Liquid Media. Phys. Rev. Lett. **80** (1998) 3503–3506.
[58] Ye, Z.; Hoskinson, E.: Band gaps and localization in acoustic propagation in water with air cylinders. Appl. Phys. Lett. **77** (2000) 4428–4430.
[59] Chen, Y. Y.; Ye, Z.: Acoustic Attenuation by Two-Dimensional Arrays of Rigid Cylinders. Phys. Rev. Lett. **87** (2001) 184301.
[60] Gupta, B. C.; Ye, Z.: Localization of classical waves in two-dimensional random media: A comparison between the analytic theory and exact numerical simulation. Phys. Rev. E**67** (2003) 036606.
[61] Sainidou, R.; Stefanou, N.; Modinos, A.: Widening of Phononic Transmission Gaps via Anderson Localization. Phys. Rev. Lett. **94** (2005) 205503.
[62] John, S.; Sompolinsky, H.; Stephen, M. J.: Localization in a disordered elastic medium near two dimensions. Phys. Rev. B**27** (1983) 5592.
[63] John, S.: Electromagnetic absorption in a disordered medium near a photon mobility edge. Phys. Rev. Lett. **53** (1984) 2169.
[64] John, S.: Localization and absorption of waves in a weakly dissipative disordered medium. Phys. Rev. B**31** (1985) 304.
[65] Wegner, F.: In: *Anderson Localization* (Eds. Y. Nagaoka, H. Fukuyama) Springer, New York (1982) 8.
[66] Kirkpatrick, T. R.: Localization of acoustic waves. Phys. Rev. B**31** (1985) 5746. Akkermans, E.; Maynard, R.: Weak localization and anharmonicity of phonons. Phys. Rev. B**32** (1985) 7850.
[67] Vollhardt, D.; Wölfle, P.: Anderson Localization in $d \leq 2$ Dimensions: A Self-Consistent Diagrammatic Theory. Phys. Rev. Lett. **45** (1980) 842. Vollhardt, D.; Wölfle, P.: Diagrammatic, self-consistent treatment of the Anderson localization problem in $d \leq 2$ dimensions. Phys. Rev. B**22** (1980) 4666.
[68] Condat, C. A.; Kirkpatrick, T. R.: Third-sound propagation on a periodic substrate. Phys. Rev. B**32** (1985) 4392.
[69] Sheng, P.; Zhang, Z. Q.: Scalar-Wave Localization in a Two-Component Composite. Phys. Rev. Lett. **57** (1986) 1879.
[70] Condat, C. A.; Krikpatrick, T. R.: Observability of acoustical and optical localization. Phys. Rev. Lett. **58** (1987) 226. Condat, C. A.: Acoustic localization and resonant scattering. J. Acoust. Soc. Am. **83** (1988) 441.

[71] Feng, S.; Kane, C.; Lee, P. A.; Stone, A. D.: Correlations and Fluctuations of Coherent Wave Transmission through Disordered Media. Phys. Rev. Lett. **61** (1988) 834.
[72] Dong, H.; Xiong, S.: Acoustic properties of a layered medium with randomly distributed layer thicknesses. J. Phys.: Condens. Matter **5** (1993) 8849.
[73] Makivic, M.; Trivedi, N.; Ullah, S.: Disordered bosons: Critical phenomena and evidence for new low energy excitations. Phys. Rev. Lett. **71** (1993) 2307.
[74] Nisamaneephong, P.; Zhang, L.; Ma, M.: Gaussian theory of superfluid-Bose-glass phase transition. Phys. Rev. Lett. **71** (1993) 3830.
[75] Sheng, P.; Zhou, M.; Zhang, Z. Q.: Phonon transport in strong-scattering media. Phys. Rev. Lett. **72** (1994) 234.
[76] Weaver, R. L.: Anderson localization in the time domain: Numerical studies of waves in two-dimensional disordered media. Phys. Rev. B**49** (1994) 58881. Weaver, R. L.: Anomalous diffusivity and localization of classical waves in disordered media: The effect of dissipation. Phys. Rev. B**47** (1993) 1077. Weaver, R. L.: Anderson localization of ultrasound. Wave Motion (1990) 129.
[77] Hodges, C. H.; Woodhouse, J.: Vibration isolation from irregularity in a nearly periodic structure – Theory and measurements. J. Acoust. Soc. Am. **74** (1983) 894.
[78] He, S.; Maynard, J. D.: Detailed measurements of inelastic scattering in Anderson localization. Phys. Rev. Lett. **57** (1986) 3171.
[79] Belzons, M; Devillard, P.; Dunlop, F.; Guazzelli, E.; Parodi, O.; Souillard, B.: Localization of surface-waves on a rough bottom – Theories and experiments. Europhys. Lett. **4** (1987) 909.
[80] Smith, D. T.; Lorenson, C. P.; Hallock, R. B.; McCall, K. R.; Guyer, R. A.: Third Sound on Substrates Patterned with Periodic and Random Disorder: Evidence for Classical Wave Localization. Phys. Rev. Lett. **61** (1988) 1286.
[81] Ziolkowski, R. W.; Lewis, D. K.; Cook, B. D.: Evidence of Localized Wave Transmission. Phys. Rev. Lett. **62** (1989) 147.
[82] Graham, I. S.; Piché, L.; Grant, M.: Experimental evidence for localization of acoustic waves in three dimensions. Phys. Rev. Lett. **64** (1990) 3135.
[83] Liu, J.; Ye, L.; Weitz, D. A.; Sheng, P.: Novel Acoustic Excitations in Suspensions of Hard-Sphere Colloids. Phys. Rev. Lett. **65** (1990) 2602.
[84] Albada, M. P.; van Tiggelen, B. A.; Lagendijk, A.; Tip, A.: Speed of propagation of classical waves in strongly scattering media. Phys. Rev. Lett. **66** (1991) 3132.
[85] Ye, L.; Cody, G.; Zhou, M.; Sheng, P.; Norris, A. N.: Observation of bending wave localization and quasi mobility edge in two dimensions. Phys. Rev. Lett. **69** (1992) 3080.
[86] Zou, B.; Zhang, Y.; Xiao, L.; Li, T.: Self-trapped state and phonon localization in TiO_2 quantum dot with a dipole layer. J. Appl. Phys. **73** (1993) 4689.
[87] Smith, W. A.; Shaulov, A. A.; Auld, B. A.: Proc. Ultrason. Symp. IEEE, New York (1985) 642.
[88] Smith, W. A.: Proc. Symp. Appl. Ferroelec. IEEE, New York (1986) 249.
[89] Auld, B. A.: In: *Ultrasonic Methods in Evaluation of Inhomogeneous materials* (Eds. A. Alipi, W. G Mayor) Nijhoff, Dordrecht (1987) 227. Baste, S.; Gerard, A.: *ibid*, 381.
[90] Smith, W. A.; Shaulov, A. A. Ferroelect. **87** (1988) 309.
[91] Auld, B. A. Mater. Sci. Eng. A**122** (1989) 65.
[92] Smith, W. A.: Proc. Ultrason. Symp. IEEE, New York (1989) 755.
[93] Takeuchi, H.; Masuzawa, H.; Nakaya, C.: Proc. Ultrason. Symp. IEEE, New York (1990) 697. Smith, W. A.; *ibid* 757.
[94] Smith, W. A.; Auld, B. A.: Modeling 1–3 Composite Piezoelectrics: Thickness-Mode Oscillations. IEEE Trans. Ultrason. Ferroelec. Freq. Contr. **38** (1991) 122 and references therein.
[95] Smith, W. A.: Proc. SPIE Symp. **1733** (1992) 3. See also in Recent Advances in Adeptive & Sensory Materials and their Applications, April 27–29 (1992) 825.
[96] Smith, W. A.: Modeling 1–3 composite piezoelectrics – hydrostatic response. IEEE Trans. Ultrason. Ferroelec. Freq. Contr. **40** (1993) 41 and references therein.
[97] Sigalas, M.; Economou, E. N.: Band structure of elastic waves in two dimensional systems. Solid State Commun. **86** (1993) 141.
[98] Ruffa, A. A.: Acoustic wave propagation through periodic bubbly liquids. J. Acoust. Soc. Am. **91** (1992) 1.
[99] Dowling, J. P.: Sonic band structure in fluids with periodic density variations. J. Acoust. Soc. Am. **91** (1992) 2539.
[100] Esquivel-Sirvent, R.; Cocoletzi, G. H.: Band structure for the propagation of elastic waves in superlattices. J. Acoust. Soc. Am. **95** (1994) 86.
[101] Kushwaha, M. S.; Halevi, P.; Martínez, G.; Dobrzynski, L.; Djafari-Rouhani, B.: Theory of acoustic band structure of periodic elastic composites. Phys. Rev. B**49** (1994) 2313.
[102] Kushwaha, M. S.; Halevi, P.: Band-gap engineering in periodic elastic composites. Appl. Phys. Lett. **64** (1994) 1085.
[103] Vasseur, J. O.; Djafari-Rouhani, B.; Dobrzynski, L.; Kushwaha, M. S.; Halevi, P.: Complete acoustic band gaps in periodic fibre reinforced composite materials: the carbon/epoxy composite and some metallic systems. J. Phys.: Condens. Matter. **6** (1994) 8759.
[104] Kushwaha, M. S.; Halevi, P.; Dobrzynski, L.; Djafari-Rouhani, B.: Kushwaha et al. Reply. Phys. Rev. Lett. **75** (1995) 3581.
[105] Kushwaha, M. S.; Halevi, P.: Giant acoustic stop bands in two-dimensional periodic arrays of liquid cylinders. Appl. Phys. Lett. **69** (1996) 31.
[106] Kushwaha, M. S.; Djafari-Rouhani, B.: Complete acoustic stop bands for cubic arrays of spherical liquid balloons. J. Appl. Phys. **80** (1996) 3191.
[107] Kushwaha, M. S.; Halevi, P.: Stop bands for cubic arrays of spherical balloons. J. Acoust. Soc. Am. **101** (1997) 619.
[108] Kushwaha, M. S.: Stop-bands for periodic metallic rods: Sculptures that can filter the noise. Appl. Phys. Lett. **70** (1997) 3218.
[109] Kushwaha, M. S.; Halevi, P.: Ultrawideband Filter for Noise Control. Jpn. J. Appl. Phys. **36** (1997) L 1043.
[110] Kushwaha, M. S.; Djafari-Rouhani, B.: Sonic stop-bands for periodic arrays of metallic rods: Honeycomb structure. J. Sound Vib. **218** (1998) 697.
[111] Kushwaha, M. S.; Djafari-Rouhani, B.; Dobrzynski, L.; Vasseur, J. O.: Sonic stop-bands for cubic arrays of rigid inclusions in air. Eur. Phys. J. B**3** (1998) 155.
[112] Kushwaha, M. S.; Akjouj, A.; Djafari-Rouhani, B.; Dobrzynski, L.; Vasseur, J. O.: Acoustic spectral gaps and discrete transmission in slender tubes. Solid State Commun. **106** (1998) 659.
[113] Kushwaha, M. S.; Djafari-Rouhani, B.: Giant sonic stop bands in two-dimensional periodic system of fluids. J. Appl. Phys. **84** (1998) 4677.
[114] Kushwaha, M. S.; Djafari-Rouhani, B.; Dobrzynski, L.: Sound isolation from cubic arrays of air bubbles in water. Physics Letters A**248** (1998) 252.
[115] Economou, E. N.; Sigalas, M.: Classical wave propagation in periodic structures: Cermet versus network topology. Phys. Rev. B**48** (1993) 13434.
[116] Sigalas, M.; Economou, E. N.: Elastic waves in plates with periodically placed inclusions. J. Appl. Phys. **75** (1994) 2845.
[117] Economou, E. N.; Sigalas, M.: Stop bands for elastic waves in periodic composite materials. J. Acoust. Soc. Am. **95** (1994) 1734.
[118] Sigalas, M. M.; Economou, E. N.; Kafesaki M.: Spectral Gaps for Electromagnetic and Scalar Waves: Possible Explanation for Certain Differences. Phys. Rev. B**50** (1994) 3393.
[119] Kafesaki, M.; Sigalas, M.; Economou, E. N.: Elastic wave band gaps in 3-D periodic polymer matrix composites. Solid State Commun. **96** (1995) 285.
[120] Sigalas, M.; Economou, E. N.: Attenuation of multiple-scattered sound. Europhys. Lett. **36** (1996) 241.
[121] Sigalas, M.: Elastic wave band gaps and defect states in two-dimensional composites. J. Acoust. Soc. Am. **101** (1997) 1256.
[122] Sigalas, M. M.: Defect states of acoustic waves in a two-dimensional lattice of solid cylinders. J. Appl. Phys. **84** (1998) 3026.
[123] Mon, K. K.: Spectral gaps for elastic waves in continuous periodic composites. J. Appl. Phys. **78** (1995) 5981.
[124] Hernandez-Cocoletzi, H.; Krokhin, A.; Halevi, P.: Reality of the eigenfrequencies of periodic elastic composites. Phys. Rev. B**51** (1995) 17181.

[125] Vasseur, J. O.; Djafari-Rouhani, B.; Dobrzynski, L.; Deymier, P. A.: Acoustic band gaps in fibre composite materials of boron nitride structure. J. Phys.: Condens. Matter **9** (1997) 7327.
[126] Hoskinson, E.; Ye, Z.: Phase Transition in Acoustic Propagation in 2D Random Liquid Media. Phys. Rev. Lett. **83** (1999) 2734.
[127] Vines, R. E.; Wolfe, J. P.; Every, A. V.: Scanning phononic lattices with ultrasound. Phys. Rev. B**60** (1999) 11871.
[128] Caballero, D.; Sánchez-Dehesa, J.; Rubio, C.; Martínez-Sala, R.; Sánchez-Perez, J. V.; Meseguer, F.; Llinares, J.: Large two-dimensional sonic band gaps. Phys. Rev. E**60** (1999) R6313–R6316.
[129] Sigalas, M.; Garcia, N.: Importance of coupling between longitudinal and transverse components for the creation of acoustic band gaps: The aluminum in mercury case. Appl. Phys. Lett. **76** (2000) 2307.
[130] Kafesaki, M.; Sigalas, M.; Garcia, N.: Frequency Modulation in the Transmittivity of Wave Guides in Elastic-Wave Band-Gap Materials. Phys. Rev. Lett. **85** (2000) 4044.
[131] Wang, X. F.; Kushwaha, M. S.; Vasilopoulos, P.: Tunability of acoustic spectral gaps and transmission in periodically stubbed waveguides. Phys. Rev. B**65**, 035107 (2002).
[132] Sainidou, R.; Stefanou, N.; Modinos, A.: Formation of absolute frequency gaps in three-dimensional solid phononic crystals. Phys. Rev. B**66** (2002) 212301.
[133] Gupta, B. C.; Ye, Z.: Theoretical analysis of the focusing of acoustic waves by two-dimensional sonic crystals. Phys. Rev. E**67** (2003) 036603.
[134] Garcia, N.; Nieto-Vesperinas, M.; Ponizovskaya, E. V.; Torres, M.: Theory for tailoring sonic devices: Diffraction dominates over refraction. Phys. Rev. E**67** (2003) 046606.
[135] Lai, Y.; Zhang, Z. Q.: Large band gaps in elastic phononic crystals with air inclusions. Appl. Phys. Lett. **83** (2003) 3900.
[136] Sainidou, R.; Stefanou, N.; Modinos, A.: Green's function formalism for phononic crystals. Phys. Rev. B**69** (2004) 064301.
[137] Zhang, X. D.; Liu, Z. Y.: Negative refraction of acoustic waves in two-dimensional phononic crystals. Appl. Phys. Lett. **85** (2004) 341.
[138] Wang, G.; Wen, X. S.; Wen, J.H.; Shao, L. H.; Liu, Y. Z.: Two-Dimensional Locally Resonant Phononic Crystals with Binary Structures. Phys. Rev. Lett. **93** (2004) 154302.
[139] Martinez-Sala, R.; Sancho, J.; Sanchez, J. V.; Gomez, V.; Llinares, J.; Meseguer, F.: Sound attenuation by sculpture. Nature **378** (1995) 241.
[140] Parmley, S.; Zobrist, T.; Clough, T.; Perez-Miller, A.; Makela, M.; Yu, R.: Phononic band structure in a mass chain. Appl. Phys. Lett. **67** (1995) 777.
[141] J. Vasseur, J. O.; Deymier, P. A.: Propagation of acoustic waves in periodic and random two-dimensional composite media. J. Mater. Res. **12** (1997) 2207.
[142] Vasseur, J. O.; Deymier, P. A.; Frantziskonis, G.; Hong, G.; Djafari-Rouhani, B.; Dobrzynski, L.: Experimental evidence for the existence of absolute acoustic band gaps in two-dimensional periodic composite media. J. Phys.: Condens. Matter **10** (1998) 6051–6064.
[143] Robertson, W. M.; Rudy, J. F.: Measurement of acoustic stop bands in two-dimensional periodic scattering arrays. J. Acoust. Soc. Am. **104** (1998) 694–699.
[144] Montero de Espinoza, F. R.; Jimenez, E.; Torres, M.: Ultrasonic Band Gap in a Periodic Two-Dimensional Composite. Phys. Rev. Lett. **80** (1998) 1208–1211.
[145] Torres, M.; Montero de Espinoza, F. R.; Garcia-Pablos, D.; Garcia, N.: Sonic Band Gaps in Finite Elastic Media: Surface States and Localization Phenomena in Linear and Point Defects. Phys. Rev. Lett. **82** (1999) 3054–3057.
[146] Meseguer, F.; Holgado, M.; Caballero, D.; Benaches, N.; Sanchez-Dehesa, J.; Lopez, C.; Llinares, J.: Rayleigh-wave attenuation by a semi-infinite two-dimensional elastic-band-gap crystal. Phys. Rev. B**59** (1999) 12169–12172.
[147] Torres, M.; Montero de Espinoza, F. R.; Aragon, J. L.: Ultrasonic Wedges for Elastic Wave Bending and Splitting without Requiring a Full Band Gap. Phys. Rev. Lett. **86** (2001) 4282–4285.
[148] Cervera, F.; Sanchis, L.; Sanchez-Perez, J. V.; Martinez-Sala, R.; Rubio, C.; Meseguer, F.; Lopez, C.; Caballero, D.; Sanchez-Dehesa, J.: Refractive Acoustic Devices for Airborne Sound. Phys. Rev. Lett. **88** (2002) 023902.
[149] Yang, S. X.; Page, J. H.; Liu, Z. Y.; Cowan, M. L.; Chan, C. T.; Sheng, P.: Ultrasound Tunneling through 3D Phononic Crystals. Phys. Rev. Lett. **88** (2002) 104301.
[150] Yang, S. X.; Page, J. H.; Liu, Z. Y.; Cowan, M. L.; Chan, C. T.; Sheng, P.: Focusing of Sound in a 3D Phononic Crystal. Phys. Rev. Lett. **93** (2004) 024301.
[151] Yablonovitch, E.: Applied physics – How to be truly photonic. Science **289** (2000) 557.
[152] El-Boudouti, E. H.; Djafari-Rouhani, B.; Khourdifi, E. M.; Dobrzynski, L.: Surface and interface elastic waves in superlattices: Transverse localized and resonant modes. Phys. Rev. B**48** (1993) 10987.
[153] El-Boudouti, E. H.; Djafari-Rouhani, B.: Acoustic waves in finite superlattices. Phys. Rev. B**49** (1994) 4586.
[154] Camley, R. E.; Djafari-Rouhani, B.; Dobzynski, L.; Maradudin, A. A.: Transverse elastic waves in periodically layered infinite and semi-infinite media. Phys. Rev. B**27** (1983) 7318.
[155] Auld, B. A.; Beaupre, G. S.; Herrmann, G.: Horizontal shear surface-waves on a laminated composite. Electron. Lett. **13** (1977) 525.
[156] Nizzoli, F.; Sandercock, J. R.: In: *Dynamical Properties of Solids* (Eds. G. K. Horton and A. A. Maradudin) North Holland, Amsterdam (1990) 281.
[157] Abrahams, E.; Anderson, P. W.; Licciardello, D. C.; Ramakrishnan, T. V.: Scaling Theory of Localization: Absence of Quantum Diffusion in Two Dimensions. Phys. Rev. Lett. **42** (1979) 673.
[158] Gay, D.: Matériaux Composites. Hermes, Paris (1991).
[159] Kushwaha, M. S.; Djafari-Rouhani, B.: Band-gap engineering in two-dimensional periodic photonic crystals. J. Appl. Phys. (2000) 2877.
[160] Kushwaha, M. S.; Martinez, G.: Magnetic-field-dependent band gaps in two-dimensional photonic crystals. Phys. Rev. B**65** (2002) 153202.
[161] Kafesaki, M.; Economou, E. N.; Sigalas, M. M.: Elastic Waves in Periodic Composite Materials. In: *Photonic Band Gap Materials* (Ed. C. M. Soukoulis) Kluwer Academic Publishers, Dordrecht (1996) 143–164.
[162] Einspruch, N.; Witterholt, E. J.; Truell, R.: Scattering of a Plane Transverse Wave by a Spherical Obstacle in an Elastic Medium. J. Appl. Phys. **31** (1960) 806.
[163] Gaunaurd, G.; Uberall, H.: Numerical Evaluation of Modal Resonances in the Echoes of Compressional Waves Scattered from Fluid-filled Spherical Cavities in Solids. J. Appl. Phys. **50** (1979) 4642. Flax, L.; Gaunaurd, G.; Uberall, H.: Theory of Resonance Scattering. In: *Physical Acoustics vol. XV* (Ed. W. P. Mason) Academic, New York (1981) 191.
[164] Brill, D.; Gaunaurd, G.; Uberall, H.: Resonance Theory of Elastic Shear-wave Scattering from Spherical Fluid Obstacles in Solids. J. Acoust. Soc. Am. **67** (1980) 414.
[165] Varadan, V. V.; Varadan, V. K.: *Acoustic Electromagnetic and Elastic Wave Scattering – Focus on the T-Matrix Approach.* Pergamon Press, New York (1979).
[166] Psarobas, I. E.; Stefanou, N.; Modinos, A.: Phononic crystals with planar defects. Phys. Rev. B**62** (2000) 5536–5540.
[167] Moadinos, A.; Nicolaou, N.: A generalized W.K.B method for calculating double barrier transmission coefficients. Surf. Sci. **17** (1969) 359.
[168] Liu, Z. Y.; Zhang, X. X.; Mao, Y. W.; Zhu, Y. Y.; Yang, Z. Y.; Chan, C. T.; Sheng, P.: Locally Resonant Sonic Materials. Science **289** (2000) 1734–1736.
[169] Psarobas, I. E.: Viscoelastic response of sonic band-gap materials. Phys. Rev. B**64** (2001) 012303.
[170] Psarobas, I. E.; Modinos, A.; Sainidou, R.; Stefanou, N.: Acoustic properties of colloidal crystals. Phys. Rev. B**65** (2002) 064307.
[171] Ayres, V. M.; Gaunaurd, G. C.: Acoustic-resonance scattering by viscoelastic objects. J. Acoust. Soc. Am. **81** (1987) 301–311.
[172] Sainidou, R.; Stefanou, N.; Psarobas, I. E.; Modinos, A.: Scattering of elastic waves by a periodic monolayer of spheres. Phys. Rev. B**66** (2002) 024303.

[173] Miyashita, T.: Sonic crystals and sonic wave-guides. Meas. Sci. Technol. **16** (2005) R47–R63.
[174] Sutter, D.: Phononische Kristalle. ETH Diploma thesis 2003.
[175] Bedford, A.; Drumheller, D. S.; Sutherland, H. J.: On modeling the dynamics of composite materials. Mechanics Today 3 (1976) 1–54.
[176] Whittier, J. S. and Peck, J. C.: Experiments on Dispersive Pulse Propagation in Laminated Composites and Comparison with Theory. J. Appl. Mech. **36** (1969) 485–490.
[177] Robinson, C. W. and Leppelmeir, G. W.: Experimental verification of dispersion relations for layered composites. J. Appl. Mech. **41** (1976) 89–91.
[178] Sutherland, H. J. and Lingle, R.: Geometric Dispersion of Acoustic-Waves by a Fibrous Composite. J. Comp. Mater. 6 (1972) 490–502.
[179] Tauchert, T. R. and Guzelsu, A. N.: Experimental Study of Dispersion of Stress Waves in a Fiber- Reinforced Composite. J. Appl. Mech. **39** (1972) 98–102.
[180] Kinra, V. K. and Ker, E. L.: An Experimental Investigation of Pass Bands and Stop Bands in 2 Periodic Particulate Composites. Int. J. Sol. Struc. **19** (1983) 393–410.
[181] James, R.; Woodley, S. M.; Dyer, C. M.; Humphrey, V. F.: Sonic bands, bandgaps, and defect states in layered structures-Theory and experiment. J. Acoust. Soc. Am. **97** (1995) 2041–2047.
[182] Shen, M. R. and Cao, W. W.: Acoustic band-gap engineering using finite-size layered structures of multiple periodicity. Appl. Phys. Letters **75** (1999) 3713–3715.
[183] Lu, Y. Q.; Zhu, Y. Y.; Chen, Y. F.; Zhu, S. N.; Ming, N. B.; Feng, Y. J.: Optical Properties of an Ionic-Type Phononic Crystal. Science **284** (1999) 1822–1824.
[184] Henderson, B. K.; Kinra, V. K.; Gonzales, A. W.: Ultrasonic diffraction by a square periodic array of spheres. J. Acoust. Soc. Am. **107** (2000) 1759.
[185] Kinra, V. K.; Day, N. A.; Maslov, K.; Henderson, B. K.; Diderich, G.: The transmission of a longitudinal wave through a layer of spherical inclusions with a random or periodic arrangement. J. Mech. Phys. Solids **46** (1998) 153–165.
[186] Kinra, V. K.; Henderson, B. K.; Maslov, K.: Elastodynamic response of layers of spherical particles in hexagonal and square periodic arrangements. J. Mech. Phys. Solids **47** (1999) 2147–2170.
[187] Maslov, K.; Kinra, V. K.: Acoustic response of a periodic layer of nearly rigid spherical inclusions in an elastic solid. J. Acoust. Soc. Am. **106** (1999) 3081–3088.
[188] Maslov, K.; Kinra, V. K.; Henderson, B. K.: Lattice resonances of a planar array of spherical inclusions: An experimental study. Mechanics of Materials **31** (1999) 175–186.
[189] Maslov, K.; Kinra, V. K.; Henderson, B. K.: Elastodynamic response of a coplanar periodic layer of elastic spherical inclusions. Mechanics of Materials **32** (2000) 785–795.
[190] Henderson, B. K.; Maslov, K.; Kinra, V. K.: Experimental investigation of acoustic band structures in tetragonal periodic particulate composite structures. J. Mech. Phys. Solids **49** (2001) 2369–2383.
[191] Turner, J. A.; Chambers, M. E.; Weaver, R. L.: Ultrasonic band gaps in aggregates of sintered aluminum beads. Acustica **84** (1998) 628–631.
[192] Sutter, D.; Krauss, G.; Steurer, W.: Phononic Quasicrystals. MRS Proc. **805** (2004) 99–104.
[193] Sanchez-Perez, J. V.; Rubio, C.; Martinez-Sala, R.; Sanchez-Grandia, R.; Gomez, V.: Acoustic barriers based on periodic arrays of scatterers. Appl. Phys. Lett. **81** (2002) 5240–5242.
[194] Vasseur, J. O.; Deymier, P. A.; Khelif, A.; Lambin, Ph.; Djafari-Rouhani, B.; Akjouj, A.; Dobrzynski, L.; Fettouhi, N.; Zemmouri, J.: Phononic crystal with low filling fraction and absolute acoustic band gap in the audible frequency range: A theoretical and experimental study. Phys. Rev. E**65** (2002) 056608.
[195] Rubio, C.; Caballero, D.; Sanchez-Perez, V.; Martinez-Sala, R.; Sanchez-Dehesa, J.; Meseguer, F.; Cervera, F.: The existence of full gaps and deaf bands in two-dimensional sonic crystals. J. Lightwave Technol. **17** (1999) 2202–2207.
[196] Lambin, Ph.; Khelif, A.; Vasseur, J. O.; Dobrzynski, L.; Djafari-Rouhani, B.: Stopping of acoustic waves by sonic polymer-fluid composites. Phys. Rev. E**63** (2001) 066605.
[197] Miyashita, T.: Full band gaps of sonic crystals made of acrylic cylinders in air-Numerical and experimental investigations. Jpn. J. Appl. Phys. **41** (2002) 3170–3175.
[198] Goffaux, C.; Maseri, F.; Vasseur, J. O.; Djafari-Rouhani, B.; Lambin, Ph.: Measurements and calculations of the sound attenuation by a phononic band gap structure suitable for an insulating partition application. Appl. Phys. Lett. **83** (2003) 281–283.
[199] Sanchis, L.; Cervera, F.; Sanchez-Dehesa, J.; Sanchez-Perez, J. V.; Rubio, C.; Martinez-Sala, R.: Reflectance properties of two-dimensional sonic band-gap crystals. J. Acoust. Soc. Am. **109** (2001) 2598–2605.
[200] Sanchis, L.; Hakansson, A.; Cervera, F.; Sanchez-Dehesa, J.: Acoustic interferometers based on two-dimensional arrays of rigid cylinders in air. Phys. Rev. B**67** (2003) 035422.
[201] Sheng, P.; Zhang, X. X.; Liu, Z. Y.; Chan, C.T.: Locally resonant sonic materials. Physica B**338** (2003) 201–205.
[202] Li, Z.; Sheng, P.; Siu, W. L.: Low-frequency soundproof concrete. Mag. Concrete Research **55** (2003) 177–181.
[203] Ho, K. M.; Cheng, C. K.; Yang, Z.; Zhang, X. X.; Sheng, P.: Broadband locally resonant sonic shields. Appl. Phys. Lett. **83** (2003) 5566–5568.
[204] Zhang, S.; Hua, J.; Cheng, J. C.: Experimental and theoretical evidence for the existence of broad forbidden gaps in the three-component composite. Chin. Phys. Lett. **20** (2003) 1303–1305.
[205] Meseguer, F.; Holgado, M.; Caballero, D.; Benaches, N.; Lopez, C.; Sanchez-Dehesa, J.; Llinares, J.: Two-dimensional elastic bandgap crystal to attenuate surface waves. J. Lightwave Tech. **17** (1999) 2196–2201.
[206] Dhar, L.; Rogers, J. A.: High frequency one-dimensional phononic crystal characterized with a picosecond transient grating photoacoustic technique. Appl. Phys. Lett. **77** (2000) 1402.
[207] McIver, P.: Wave interaction with arrays of structures. Appl. Ocean Res. **24** (2002) 121–126.
[208] Bogomolov, V. N.; Parfeneva, L. S.; Smirnov, I. A.; Misiorek, H.; Jzowski, A.: Phonon propagation through photonic crystals-media with spatially modulated acoustic properties. Phys. Solid State **44** (2002) 181–185.
[209] Khelif, A.; Choujaa, A.; Djafari-Rouhani, B.; Wilm, M.; Ballandras, S.; Laude, V.: Trapping and guiding of acoustic waves by defect modes in a full-band-gap ultrasonic crystal. Phys. Rev. B**68** (2003) 214301.
[210] Khelif, A.; Choujaa, A.; Benchabane, S.; Djafari-Rouhani, B.; Laude, V.: Guiding and bending of acoustic waves in highly confined phononic crystal waveguides. Appl. Phys. Lett. **84** (2004) 4400.
[211] Miyashita, T.; Inoue, C.: Numerical investigations of transmission and waveguide properties of sonic crystals by finite-difference time-domain method. Jpn. J. Appl. Phys. **40** (2001) 3488–3492.
[212] Sigmund, O.; Jensen, J. S.: Systematic design of phononic band-gap materials and structures by topology optimization. Philos. Trans. R. Soc. Lond. Ser. A**361** (2003) 1001–1019.
[213] Russell, P. S.; Marin, E.; Diez, A.; Guenneau, S.; Movchan, A. B.: Sonic band gaps in PCF preforms: enhancing the interaction of sound and light. Optics Express **11** (2003) 2555–2560.
[214] Lide, D. R. (Ed.): CRC Handbook of Chemistry and Physics. CRC Press, Boca Raton 2001.
[215] Klironomos, A. D.; Economou, E. N.: Elastic wave band gaps and single scattering. Solid State Commun. **105** (1998) 327–332.